© 2010 Trishan Esram

MODELING AND CONTROL OF AN ALTERNATING-CURRENT PHOTOVOLTAIC MODULE

BY

TRISHAN ESRAM

DISSERTATION

Submitted in partial fulfillment of the requirements
for the degree of Doctor of Philosophy in Electrical and Computer Engineering
in the Graduate College of the
University of Illinois at Urbana-Champaign, 2010

Urbana, Illinois

Doctoral Committee:

Associate Professor Patrick L. Chapman, Chair
Professor Philip T. Krein
Professor Ty A. Newell
Professor Peter W. Sauer
Assistant Professor Robert S. Balog, Texas A&M University

ABSTRACT

Energy independence depends greatly on the adoption of renewable energy sources. Yet, electricity, a commodity of everyday life, is currently being generated primarily from fossil fuels in the U.S. Despite the abundance of solar energy, the total electricity from photovoltaic (PV) sources is negligible, mainly because of the relatively high cost of PV systems. For PV electricity to become mainstream, its price has to reach grid parity, which is unachievable unless the overall cost of PV systems is reduced.

Alternating-current (ac) PV modules are shown to have the potential to significantly decrease the cost of PV systems. An ac PV module consists of an individual conventional PV module embodying a small inverter, often called a microinverter. AC PV modules provide simpler, faster, and less expensive installation. Unlike typical inverters, microinverters are more reliable and robust and do not have to be replaced once or twice over the lifetime of the system. The flexibility provided by ac PV modules with individual maximum power point tracking (MPPT) may also increase the energy yield.

With several microinverters operating simultaneously in a PV system, as opposed to only one or two bigger inverter(s), it is of particular interest to investigate the behavior and dynamics of such a PV system and its compliance with regulatory codes and standards when interconnected with the utility grid. For this purpose, complete detailed ac PV module models, along with different possible control techniques, are developed, analyzed, and tested through simulations. Average-value models (AVMs) for the ac PV modules are shown to drastically reduce simulation times while preserving their performances. The ac PV module AVMs therefore allow for rapid simulations and analyses of several ac PV modules running concurrently under numerous conditions.

I dedicate this dissertation to
my mother, father, and brother.

ACKNOWLEDGMENTS

First of all, I would like thank my adviser, Professor Patrick L. Chapman. I remember clearly the first phone call I received from him, asking me whether I was still interested in joining the University of Illinois for my graduate studies under his supervision. It was a privilege for me to accept his offer and I spent the following several exceptional years learning from him and doing research with him. His advice, guidance, and help have always been invaluable. This dissertation is the outcome of the great collaboration between him and me. All this work would have been impossible without him.

I also remember my first meeting with Professor Chapman, at a time when he had just founded SmartSpark Energy Systems, Inc. He casually mentioned that maybe I could work for SmartSpark after graduation. Little did I know that this would indeed happen, although earlier than expected. I have been working for SmartSpark, now SolarBridge Technologies, Inc., for more than two years and much of the experience that I gained there is reflected in this dissertation. I would like to thank all my colleagues at SolarBridge for their support while I was finishing this dissertation.

I would also like to thank Professors Philip T. Krein and Robert S. Balog, whose research on the cycloconverter-type inverter instigated this dissertation on microinverter and ac PV module design. I have learned a considerable amount from Professor Krein's classes, as both a student and a teaching assistant. Professor Balog's time and patience in teaching me the cycloconverter operation will always be appreciated. I would like to thank Professors Peter W. Sauer and Ty A. Newell for being critics of this research from a different perspective than power electronics. I will never forget the amazing time I spent working with Professor Newell on the Solar Decathlon.

Most importantly, I would like to thank my parents, who have always been there for me. Their unconditional love and support have helped me surpass my own expectations. My brother has always known how to motivate me and push me beyond my limits; I thank him for that. Nora Wang, someone very special, has provided me with constant support, advice, ideas, and help throughout this dissertation work; I can never thank her enough for being there for me. I will forever be grateful to Rodney and Linda for their friendship. My thanks also go to the entire Power and Energy Systems group for hosting me for so many years and Jamie Hutchinson for editing this dissertation.

TABLE OF CONTENTS

Page

LIST OF FIGURES vii

LIST OF TABLES xi

1 INTRODUCTION 1
1.1 Overview 1
1.2 Grid Parity 2
1.3 AC PV Modules 9
1.4 Initially Proposed Microinverter 14
1.5 Alternative Microinverter 18

2 INPUT STAGE 20
2.1 Overview 20
2.2 PV Module Model 22
2.3 MPPT Algorithm 30
2.4 Boost Converter Setup for MPPT Analysis 35
2.5 Isolated Boost Converter 43
2.6 Average-Value Model 45

3 OUTPUT STAGE 47
3.1 Overview 47
3.2 Abnormal Voltages 49
3.3 Abnormal Frequencies 50
3.4 Power Quality 50
3.5 Islanding 51
3.6 Output Stage Simulations 62
3.7 Average-Value Model 69

4 ENERGY STORAGE 73
4.1 Overview 73
4.2 Passive Filter 75
4.3 Active Filter 84

5 MULTI-INVERTER SYSTEM 96
5.1 Overview 96
5.2 Abnormal Grid Conditions 99
5.3 Islanding Detection in a PV System with Identical IDMs 100
5.4 Islanding Detection in a PV System with Mixed IDMs 102
5.5 Power Quality 105

6 CONCLUSION 109
6.1 Future Work 112

APPENDIX A CODES 113
A.1 MATLAB Code for PV Data Extraction 113
A.2 Complete PV Module Model Modelica Code 114
A.3 *dP*-P&O MPPT Algorithm Modelica Code 115
A.4 Modelica Code to Compute Root-Mean-Square (rms) 117
A.5 Modelica Code to Compute Frequency 118
A.6 MATLAB Code to Perform FFT and Compute THD 118
A.7 Modelica Code for AFD IDM Current Command Generation 119
A.8 Modelica Code for SMS IDM Current Command Generation 120
A.9 Modelica Code for SFS IDM Current Command Generation 121
A.10 Modelica Code for Fault Detection 122

APPENDIX B DERIVATIONS 124
B.1 Transfer Functions for Microinverter Input Stage 124
B.2 Transfer Functions for Microinverter with Passive Filter 126
B.3 Transfer Functions for Microinverter with Active Filter 128

APPENDIX C MULTIPLE-CARRIER PWM 131

REFERENCES 134

LIST OF FIGURES

Page

Fig. 1.1 2008 U.S. electric power industry net generation [4] 2
Fig. 1.2 Solar resources in Germany and the U.S., from [3] 3
Fig. 1.3 Electricity price peaking and irradiance on a typical summer day in Illinois 4
Fig. 1.4 2007 state electricity profile in ¢/kWh, from [8] 5
Fig. 1.5 Variation in average installed cost among states, from [9] 5
Fig. 1.6 Variation in average installed cost based on PV system size, from [9] 6
Fig. 1.7 2008 components of U.S. average electricity prices [10] 6
Fig. 1.8 PV module prices (left) [11] and inverter prices (right) [12] 7
Fig. 1.9 Cost fractions from Table 1.2 [13] 8
Fig. 1.10 Setups for two different PV systems: PV system with string inverter (left) and PV system with ac PV modules (right) 10
Fig. 1.11 Additional power yielded by using ac PV modules instead of a string inverter 11
Fig. 1.12 Possible microinverter topologies as shown in [24]: (a) with line-frequency transformer and (b) with high-frequency transformer 12
Fig. 1.13 Classification of microinverters with high-frequency transformers [24]: microinverter with (a) dc link, (b) pseudo dc link, and (c) no dc link 13
Fig. 1.14 Cycloconverter-type high-frequency link inverter proposed in [26] 14
Fig. 1.15 State machine for cycloconverter control [27] 15
Fig. 1.16 Experimental waveforms and logic signals for initially proposed microinverter [27] 15
Fig. 1.17 Dymola simulation setup for initially proposed microinverter 16
Fig. 1.18 Simulation waveforms and logic signals from Dymola setup 16
Fig. 1.19 Grid-tied cycloconverter-type inverter with PV source 17
Fig. 1.20 Waveforms with PV source and input filter 18
Fig. 1.21 Alternative microinverter with PV source and grid-tied 19

Fig. 2.1 Microinverter input stage 20
Fig. 2.2 Example of characteristic *i*-*v* curve of a PV module 20
Fig. 2.3 Effects of insolation (left) and temperature (right) on a PV characteristic curve [30] 21
Fig. 2.4 PV module model 22
Fig. 2.5 Dymola PV module model block 29
Fig. 2.6 Voltage sweep simulation setup 29
Fig. 2.7 Good correlation between datasheet (left) [29] and simulated (right) *i*-*v* curves under varying *T* 29
Fig. 2.8 *i*-*v* (left) and *p*-*v* (right) curves under varying insolation 30
Fig. 2.9 Slopes of PV module characteristic curve 31
Fig. 2.10 Flowchart for basic P&O MPPT algorithm 32
Fig. 2.11 Divergence of P&O under rapid insolation change 33
Fig. 2.12 *dP*-P&O additional power measurement between two updates 33
Fig. 2.13 Flowchart for *dP*-P&O MPPT algorithm 34

Fig. 2.14 Dymola *dP*-P&O MPPT block 35
Fig. 2.15 Boost converter connected to PV module 35
Fig. 2.16 Switching signal generation from MPPT duty ratio command 36
Fig. 2.17 Dymola setup to simulate MPPT with duty ratio command 36
Fig. 2.18 Steady-state waveforms for MPPT with duty-ratio command 37
Fig. 2.19 120-Hz load disturbance transmitted to the input 37
Fig. 2.20 Switching signal generation from MPPT current command 38
Fig. 2.21 Bandwidth of the input current control loop 38
Fig. 2.22 Bode plot of input current control loop 39
Fig. 2.23 Input transconductance 39
Fig. 2.24 Dymola setup to simulate MPPT with current command 40
Fig. 2.25 Steady-state waveforms for MPPT with current command 41
Fig. 2.26 Power collapse with MPPT current command under rapid decrease in insolation 41
Fig. 2.27 Switching signal generation from MPPT voltage command 42
Fig. 2.28 Alternative switching signal generation from MPPT voltage command 42
Fig. 2.29 Dymola setup to simulate MPPT with voltage command 42
Fig. 2.30 Robustness of control scheme using MPPT with voltage command under varying insolation 43
Fig. 2.31 Switching signals for input full-bridge inverter 44
Fig. 2.32 Dymola microinverter input stage setup 45
Fig. 2.33 Dymola average-value model for input converter 45
Fig. 2.34 Dymola setup with boost converter average-value model 46
Fig. 2.35 Waveforms from boost converter average-value model setup 46

Fig. 3.1 Microinverter output stage 47
Fig. 3.2 Common grid-tied PV system interconnection as shown in [41] 47
Fig. 3.3 Dymola root-mean-square (rms) computation block 49
Fig. 3.4 Dymola frequency computation block 50
Fig. 3.5 Magnitude and phase of an example parallel RLC load 53
Fig. 3.6 Nondetection zone for UFP/OFP 54
Fig. 3.7 AFD current waveform and its fundamental with respect to voltage waveform 55
Fig. 3.8 Nondetection zone for AFD 57
Fig. 3.9 Intersections of load lines and disturbance functions 58
Fig. 3.10 Nondetection zone for SMS 59
Fig. 3.11 Nondetection zone for SFS 61
Fig. 3.12 Dymola block for IDM current command generation 62
Fig. 3.13 Dymola setup to simulate output stage 62
Fig. 3.14 i_{out} and i^* when δf = 1.5 Hz with AFD IDM 64
Fig. 3.15 Harmonic content of i_{out} when δf = 1.5 Hz with AFD IDM 64
Fig. 3.16 AFD islanding detection when δf = 1.5 Hz, Q_f = 1.0, and f_0 = 60 Hz 65
Fig. 3.17 AFD islanding nondetection when δf = 1.5 Hz, Q_f = 3.0, and f_0 = 60 Hz 66
Fig. 3.18 i_{out} and i^* when θ_m = 10° with SMS IDM 66
Fig. 3.19 Harmonic content of i_{out} when θ_m = 10° with SMS IDM 67
Fig. 3.20 SMS islanding detection when θ_m = 10°, Q_f = 1.0, and f_0 = 60 Hz 67

Fig. 3.21 SMS islanding nondetection when $\theta_m = 10°$, $Q_f = 3.0$, and $f_0 = 60$ Hz 68
Fig. 3.22 SFS islanding detection when $k = 0.05$, $\delta f_0 = 1.5$ Hz, $Q_f = 1.0$, and $f_0 = 60$ Hz 68
Fig. 3.23 SFS islanding nondetection when $k = 0.05$, $\delta f_0 = 1.5$ Hz, $Q_f = 3.0$, and $f_0 = 59.6$ Hz 69
Fig. 3.24 Dymola average-value model for output full-bridge inverter 70
Fig. 3.25 Dymola output stage setup using output full-bridge AVM 70
Fig. 3.26 AFD islanding detection with AVM when $\delta f = 1.5$ Hz, $Q_f = 1.0$, and $f_0 = 60$ Hz 71
Fig. 3.27 SMS islanding detection with AVM when $\theta_m = 10°$, $Q_f = 1.0$, and $f_0 = 60$ Hz 71
Fig. 3.28 SFS islanding detection with AVM when $k = 0.05$, $\delta f_0 = 1.5$ Hz, $Q_f = 1.0$, and $f_0 = 60$ Hz 72

Fig. 4.1 AC PV module connected to the utility grid 73
Fig. 4.2 Microinverter instantaneous output power 74
Fig. 4.3 Double-frequency power 74
Fig. 4.4 Double-frequency energy 75
Fig. 4.5 Control topology for passive filter 77
Fig. 4.6 Bandwidth of bus voltage control loop 78
Fig. 4.7 Bode plot of bus voltage control loop gain 78
Fig. 4.8 Effective bus impedance 79
Fig. 4.9 Dymola setup for grid-tied ac PV module with passive filter 80
Fig. 4.10 Simulation waveforms of grid-tied ac PV module with passive filter 81
Fig. 4.11 Simulation waveforms of average-value model of ac PV module with passive filter 82
Fig. 4.12 Average-value model of ac PV module with passive filter 83
Fig. 4.13 Waveforms under rapid insolation changes for ac PV module with passive filter 84
Fig. 4.14 Energy variation in passive filter 85
Fig. 4.15 Active filter converter 86
Fig. 4.16 Ideal active filter waveforms 86
Fig. 4.17 Waveforms resulting from energy offset 87
Fig. 4.18 Control topology for active filter, based on [56] 88
Fig. 4.19 Bandwidth of bus voltage control loop 89
Fig. 4.20 Bode plot of bus voltage control loop gain 89
Fig. 4.21 Bandwidth of active filter voltage control loop 90
Fig. 4.22 Bode plot of active filter voltage control loop gain 90
Fig. 4.23 Effective bus impedance in the presence of active filter 90
Fig. 4.24 Simulation waveforms of grid-tied ac PV module with active filter 91
Fig. 4.25 Dymola setup for grid-tied ac PV module with active filter 92
Fig. 4.26 Simulation waveforms of average-value model of ac PV module with active filter 93
Fig. 4.27 Average-value model of ac PV module with active filter 94
Fig. 4.28 Waveforms under rapid insolation changes for ac PV module with active filter 95

Fig. 5.1 PV system with multiple ac PV modules 97
Fig. 5.2 Dymola ac PV module blocks 98
Fig. 5.3 Dymola setup to simulate PV system with multiple ac PV modules 98
Fig. 5.4 Shutdown of a PV system with 10 ac PV modules due to abnormal grid voltage 99
Fig. 5.5 Shutdown of a PV system with 10 ac PV modules due to abnormal grid frequency 100
Fig. 5.6 Islanding detection in a PV system of 10 ac PV modules with AFD 100
Fig. 5.7 Islanding detection time for different combinations of ac PV modules with AFD and SMS 103
Fig. 5.8 Islanding detection time for different combinations of ac PV modules with AFD and SFS 104
Fig. 5.9 Islanding detection time for different combinations of ac PV modules with SFS and SMS 105
Fig. 5.10 PWM switching signals generation for the output full-bridge converter 106
Fig. 5.11 Current i_{PV} with synchronized carrier signals 107
Fig. 5.12 Harmonics around switching frequency with synchronized carrier signals 107
Fig. 5.13 Carrier signals 90° out of phase from each other 108
Fig. 5.14 Current i_{PV} with unsynchronized carrier signals 108
Fig. 5.15 Harmonics around switching frequency with unsynchronized carrier signals 108

Fig. C.1 Example of multiple-carrier PWM generation 132
Fig. C.2 Two methods of generating the same gate control sequence 133

LIST OF TABLES

Page

Table 1.1 Electricity generation costs [5] 3
Table 1.2 Cost breakdown for installed residential PV system in 2008 [13] 8

Table 2.1 Simulated MPP datapoints vs. insolation levels 30

Table 3.1 Interconnection system response to abnormal voltages [42] 49
Table 3.2 Interconnection system response to abnormal frequencies [42] 50
Table 3.3 Maximum harmonic current distortion in percent of current [42] 51

Table 4.1 Microinverter and control parameter settings 79

Table 5.1 Islanding detection time versus number of ac PV modules, at 1000 W/m^2 and 25 °C 101
Table 5.2 Islanding detection time versus insolation, with 10 ac PV modules at 25 °C 102
Table 5.3 Islanding detection time for different combinations of ac PV modules with AFD and SMS 102
Table 5.4 Islanding detection time for different combinations of ac PV modules with AFD and SFS 104
Table 5.5 Islanding detection time for different combinations of ac PV modules with SFS and SMS 105

1 INTRODUCTION

1.1 Overview

With the soaring prices and scarcity of fossil fuels, the pursuit of energy independence, and the growing concern about carbon emissions, solar energy is showing great potential. Consequently, producing electricity from photovoltaic (PV) systems is becoming more feasible. Yet, for PV electricity to become mainstream, grid parity—the point at which PV resources become competitive with more conventional electrical resources [1]—has to be reached. In Section 1.2, different views of grid parity will be discussed. Regardless of the type of parity, cheaper and more efficient solar cell technologies, cheaper and more reliable inverters, cheaper and easier installation, better governmental policies and incentives, and better green public education are required to bring down PV system costs, which, in turn, can lower the cost of PV electricity.

Alternating-current (ac) PV modules, though not currently on the market, can help achieve several of these requirements. An ac PV module consists of an individual conventional PV module embodying a relatively small inverter, often called a microinverter. The different aspects of ac PV modules will be covered in Section 1.3, along with a review of possible microinverter topologies. While microinverters serve the same purpose as bigger string or central inverters that are connected to strings or arrays of PV modules—conversion of direct-current (dc) power from PV modules into ac power—they represent a couple of challenges. Attached to the back of PV modules, microinverters have to be not only compact and light, but also reliable enough to match or outlast the common 20–25-year lifetime of the PV modules.

A cycloconverter-type inverter topology showed the potential to meet these challenges and was thus initially proposed for this research work. However, as discussed in Section 1.4, upon further investigation of this inverter topology in the context of ac PV modules, several limitations arose in terms of controls and component sizes, making it less suitable to be incorporated into ac PV modules.

A topology consisting of an isolated boost converter input stage and a full-bridge inverter output stage is therefore proposed in Section 1.5 for the microinverter. In the subsequent chapters, this microinverter, along with necessary controls for its two stages, will be developed, modeled, and tested through simulations. Combined with a model of a

PV module, the microinverter and its controls will form a complete ac PV module model. The performance of the ac PV module model will also be evaluated via simulations. Several ac PV modules in parallel on the same circuit—representative of a typical PV system—connected to the ac utility grid will be simulated to investigate the interaction of microinverters with the grid and verify compliance with regulatory codes and standards. The ac PV module model will be a useful tool for future development of PV systems.

1.2 Grid Parity

1.2.1 Photovoltaic in the Electricity Market

The abundance of solar energy is indisputable. According to [2], the sun provides four orders of magnitude more power than the 13 terawatts (TW) consumed by the world, and only about 4 gigawatts (GW)—or about four orders of magnitude less than the world's power consumption—of photovoltaic is installed across the world. In other words, solar energy is being underutilized and there is plenty of room for PV systems to penetrate the electricity market.

According to a 2007 PV market survey, "the U.S. solar energy industry saw a glimpse of a gigawatt future"—the point at which contribution to the overall electricity production becomes significant and noticeable [3]. However, in 2008, less than 1% of the electricity generated in the U.S. was from solar power, based on data from the U.S. Energy Information Administration (EIA). The remainder was dominated by fossil fuel and nuclear sources, as can be seen in Fig. 1.1, which shows the breakdown of the U.S. electric power industry net generation in 2008 [4].

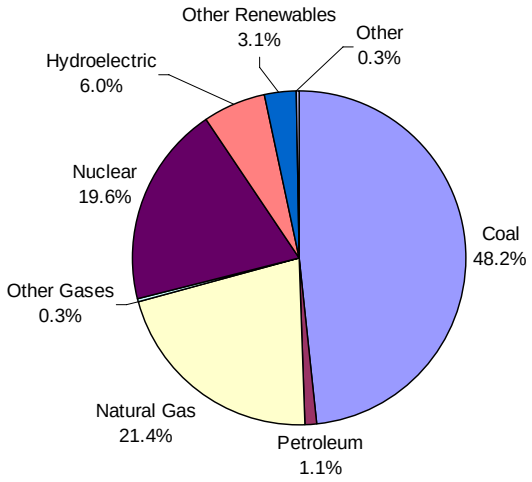


Fig. 1.1 2008 U.S. electric power industry net generation [4]

Although its PV installations and production have been increasing at a steady rate, the U.S. is only the fourth largest PV market in the world, behind Germany, Japan, and Spain [3]. Ironically, when compared to Germany, solar resources are considerably higher in the U.S., as shown in Fig. 1.2. The U.S. clearly has all the required resources for solar energy to be a major contributor to the electricity market, but the cost of generating electricity from PV systems has remained high, making grid parity difficult to achieve.

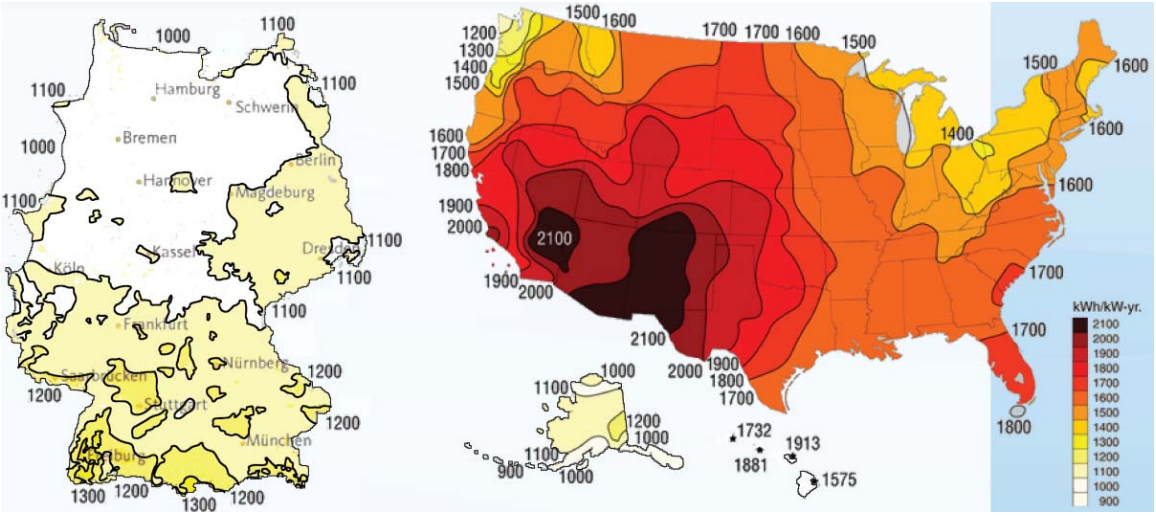


Fig. 1.2 Solar resources in Germany and the U.S., from [3]

Table 1.1 [5] gives a general idea of the present costs of generating electricity from several sources and confirms that PV electricity costs are an order of magnitude higher than those of base load generation sources such as coal. It is worth noting that electricity costs from distributed PV systems (like residential rooftop systems) tend to be higher than centralized PV systems (like utility-scale systems). As can also be noted, wind energy is on par with the base load sources, hence its successful integration in the electricity market.

Table 1.1 Electricity generation costs [5]

Source	**¢/kWh**
Coal integrated gas combined cycle (IGCC)	3–5
Wind	4–7
Biomass gasification	7–9
Remote diesel generation	20–40
PV central station	20–30
PV distributed	20–50

Which one or combination of the sources is used to generate electricity depends on the market demand, which varies continuously throughout the day and year. As a result, there are several different kinds of grid parity: spot market, peak, retail, and cost parity [1]. While spot market parity is the easiest to achieve by the cost of PV energy matching or falling below the locational marginal price (LMP) of a given area, the very rare occurrence of high LMPs makes it the least useful [1].

1.2.2 Peak Parity

Peak parity, on the other hand, is considered as being the point at which PV electricity cost matches or falls below generation costs from conventional peaking sources such as diesel generators. Peak parity is more viable not only because the costs of producing electricity on a large scale from PV and diesel are already in the same range (see Table 1.1), but also because solar energy tends to be most readily available at the times of peak demand. This is evident from Fig. 1.3, which shows the solar irradiance recorded on a typical summer day in Illinois [6] along with the electricity real time price (RTP) for that same day [7].

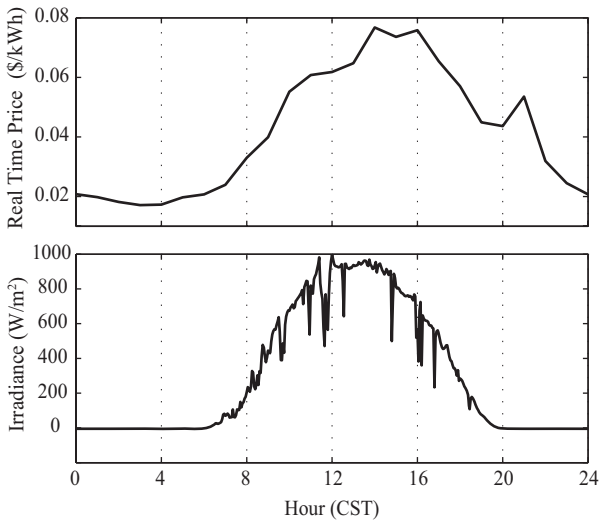


Fig. 1.3 Electricity price peaking and irradiance on a typical summer day in Illinois

1.2.3 Retail Parity

When PV electricity cost at the point of end use equals or drops below the average retail cost at a given location, retail parity is reached—this is the usual definition of grid parity [1]. However, since average electricity prices vary from state to state as reported by the EIA [8] and shown in Fig. 1.4, for a given PV system cost, retail parity cannot be

achieved simultaneously nationwide. This is further accentuated by the fact that, based on 37,000 PV system installations throughout the country, [9] reported that the average installed cost of PV systems varies not only across states, as shown in Fig. 1.5, but also with size as in Fig. 1.6. These result from bigger systems benefitting from economy of scale and states having different policies, incentives, and cost of labor, among several factors affecting the cost of PV systems.

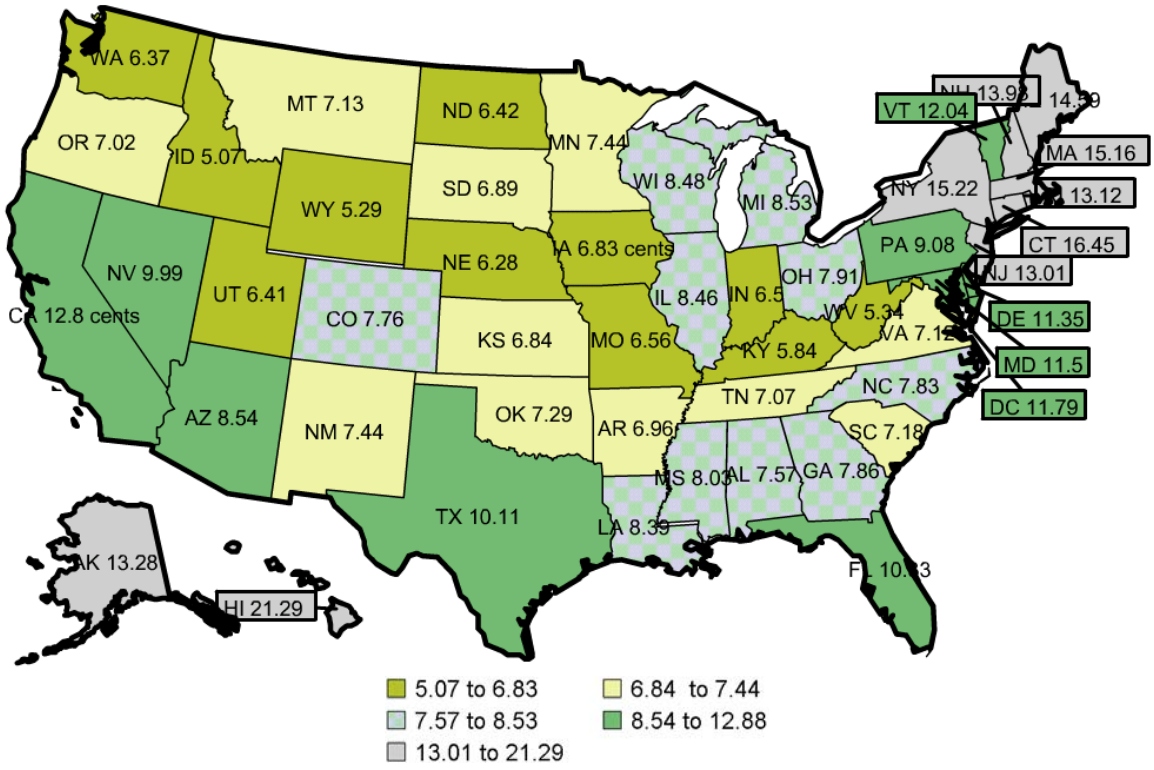


Fig. 1.4 2007 state electricity profile in ¢/kWh, from [8]

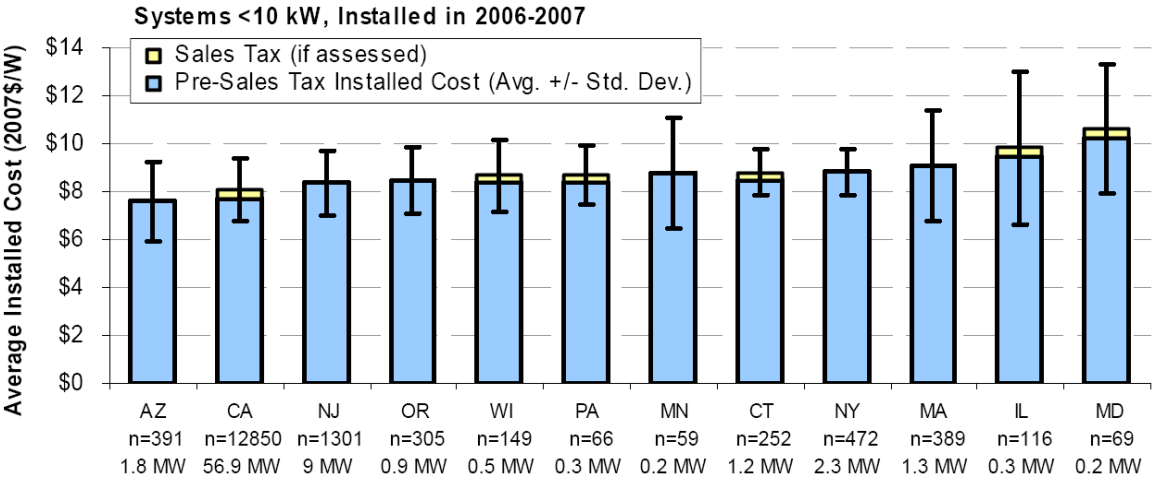


Fig. 1.5 Variation in average installed cost among states, from [9]

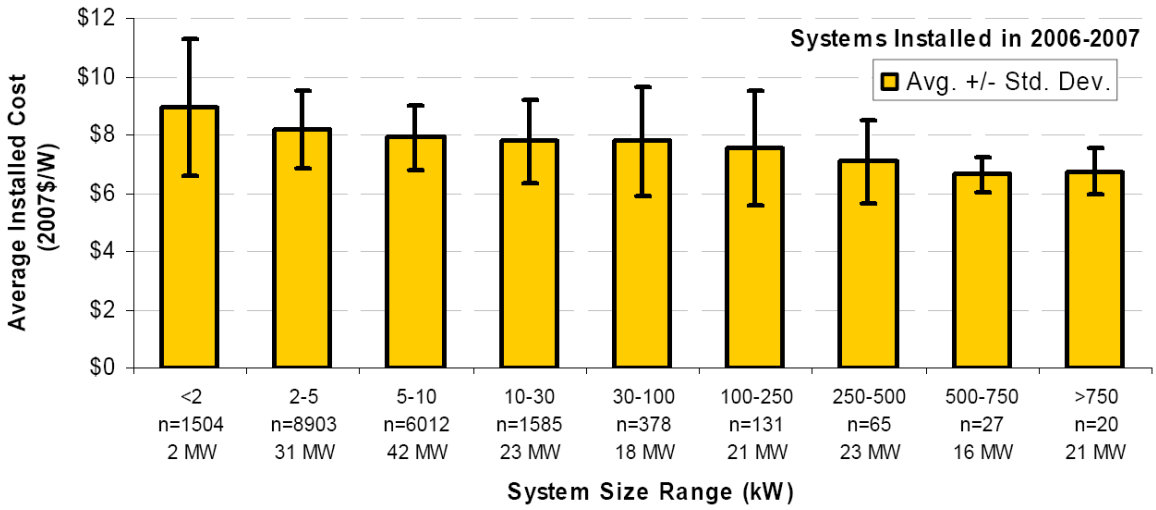


Fig. 1.6 Variation in average installed cost based on PV system size, from [9]

In Figs. 1.5 and 1.6, "n" represents the number of installations in each category. It is interesting to see in Fig. 1.5 that California and New Jersey have the most PV system installations—the positive consequence of their better policies and attractive incentives. Even more interesting in Fig. 1.6 is that most of the installations are in the 2–5-kW range, which usually corresponds to residential-scale systems. For residential rooftop installations, PV electricity has to compete with the retail electricity prices, which include distribution and transmission fees. According to the EIA [10], these usually accounted for about 31% of the price in 2008, as shown by the distribution in Fig. 1.7. Therefore, even though Table 1.1 indicates higher electricity prices for distributed PV systems, they should not be compared to the other sources without including the distribution and transmission fees. This also indicates that, although more costly to install, smaller PV systems might reach grid parity concurrently with or even sooner than larger ones.

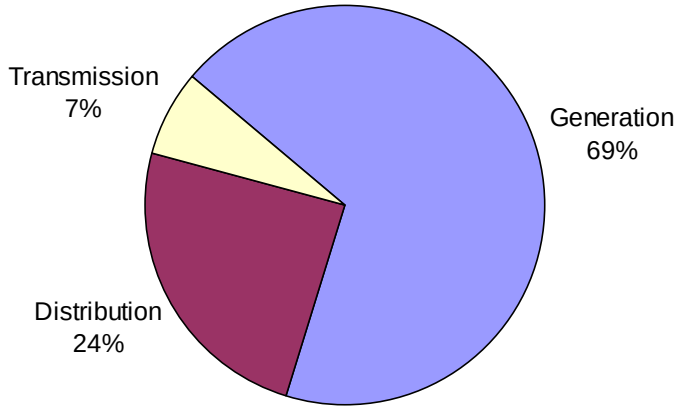


Fig. 1.7 2008 components of U.S. average electricity prices [10]

1.2.4 Cost Parity

Probably the most difficult to reach, cost parity is when the cost of PV electricity is less than or equal to wholesale electricity rates or even dominant base load rates for a given region [1]. Achieving cost parity implies that PV sources are able to successfully compete with other energy sources, thus increasing the initiatives to proliferate the use of solar energy. As mentioned above, electricity from wind energy is very close to cost parity, as witnessed by its strong presence in the U.S. and many other countries.

1.2.5 Implications

Based on peak, retail, and wholesale rates in typical U.S. locations and the amount of energy that a conventional PV cell can produce over its lifetime at a typical location in North America, [1] estimated that peak, retail, and cost parity can be reached if the initial installed cost of a complete unsubsidized PV system is about $4.38, $2.63, and $1.10 per peak watt, respectively. According to Solarbuzz, as of March 2010, the average retail prices are about $4.24 per watt for PV modules [11] and $0.72 per watt for inverters [12], resulting in a total of $4.96 per watt. This is already above the peak parity cost and does not even include installation costs. In Fig. 1.8, it is interesting to note that PV module prices showed some decline in the past year, unlike inverter prices.

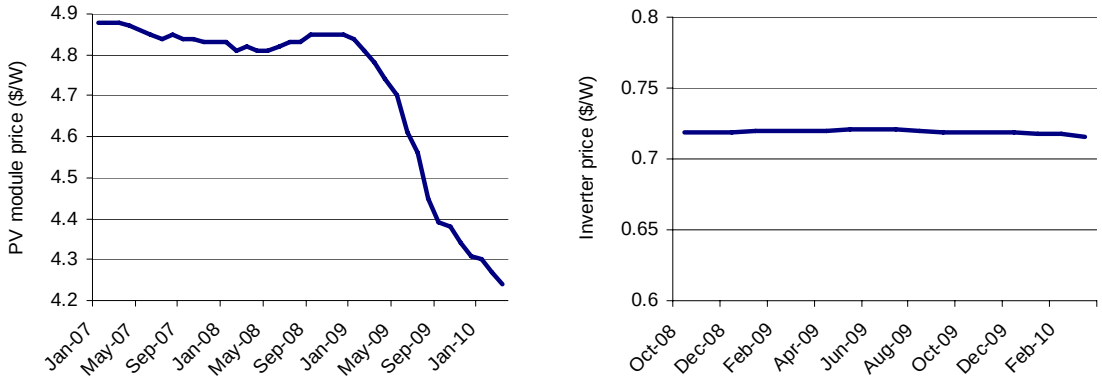


Fig. 1.8 PV module prices (left) [11] and inverter prices (right) [12]

A more comprehensive breakdown of the initial cost of installing a PV system in 2008 is given in Table 1.2, using data from [13]. The total amounts to $8.25 per watt. While the costs are somewhat optimistic when compared to those in Fig. 1.8, the relative values are instructive. The percentages of the breakdown are shown in Fig. 1.9 and are

representative of systems in the range of 2 to 5 kW—larger systems have a different relative mix. As can be seen, manufacturing the PV cells and assembling them into modules represent about 45% of the total cost. The remainder is divided among the installation of the system, inverters, and other hardware components. It is interesting to see that installation accounts for 40% of the price. It also has to be pointed out that, even though the inverters represent only about 6% of the up-front total price, they usually have to be replaced once or twice over the lifetime of the PV system since the mean time between failures (MTBF) of an inverter is from 5 to 10 years, while the MTBF of most PV modules is about 25 years. This further increases the contribution from inverters [1].

Table 1.2 Cost breakdown for installed residential PV system in 2008 [13]

Sector	**Cost ($/W)**
Polysilicon	1.50
Wafers from polysilicon	0.75
PV cells from wafers	0.75
Completion of PV modules	0.75
Inverters	0.50
Other components	0.75
Installer's labor	1.25
Installer's overhead	2.00
Total	8.25

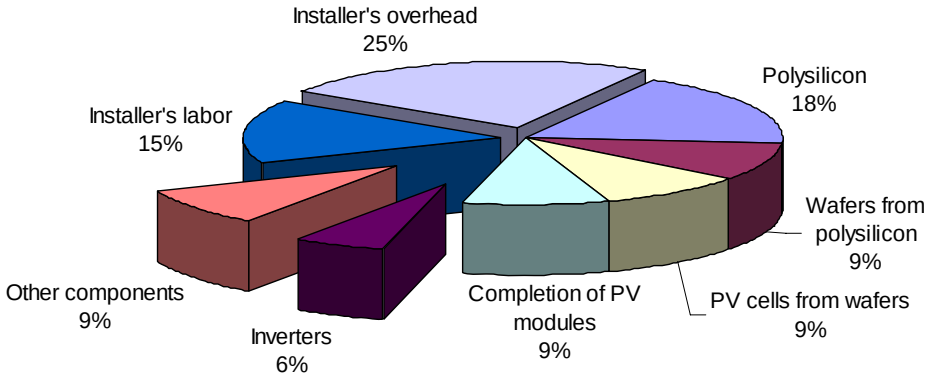


Fig. 1.9 Cost fractions from Table 1.2 [13]

There seems to be a misconception that lowering the cost of PV modules alone can lead to grid parity [14]. Clearly, to achieve any one type of grid parity, the overall cost of PV systems has to be brought down by decreasing the cost of every sector in Fig. 1.9. As will be discussed hereinafter, the use of ac PV modules has the potential to cut the costs of all the sectors except those related to the manufacturing of PV modules.

1.3 AC PV Modules

1.3.1 Simpler and Less Expensive Installation

Clause 690.2 of the 2008 National Electrical Code (NEC) [15] defines an ac PV module as "a complete, environmentally protected unit consisting of solar cells, optics, inverter, and other components, exclusive of tracker, designed to generate ac power when exposed to sunlight." In other words, unlike regular PV modules, ac PV modules do not have any accessible dc circuits, and none of the dc code requirements in Section 690 of the NEC apply [16]. This definition also implies that ac PV modules are listed as unified devices consisting of small inverters attached permanently to the back of conventional PV modules [16]. As mentioned in [16], the interconnections of separately listed small inverters and PV modules do not qualify as an ac PV module, and requirements are imposed on dc wire size, dc overcurrent protection, and ground fault interruption, as per the NEC. Equipment grounding of the PV module frame can also be done through the integrated inverter, thus eliminating the need to run a separate equipment-grounding conductor, as is commonly the case in a typical PV system.

With the modular aspect of ac PV modules, power mismatch among PV modules is not problematic because they work independently of each other, with individual maximum power point tracking (MPPT) [17, 18]. Since there is no need to match the voltage and current ratings of the PV modules, PV systems can easily incorporate different PV modules—either of the same model with widely varying tolerances, different models from the same manufacturer, or from different manufacturers. Unlike systems with string or central inverters, systems with ac PV modules do not have to enforce precision and consistency in mounting the PV modules to ensure maximum energy yield. As a result, simpler mounting hardware/components can be used, making the installation process easier, faster, and less expensive.

1.3.2 Extended Inverter Lifetime

As pointed out above, the inverter attached permanently to the back of the PV module is an inherent feature of an ac PV module. As such, unlike string and central inverters that only last 5 to 10 years, inverters for ac PV modules must be reliable enough to match or outlast the common 20–25-year lifetime of the PV modules. Conventional inverters

usually suffer from poor reliability because of their use of low-cost aluminum electrolytic capacitors for internal energy storage. These capacitors have limited life that is difficult to extend even with derating strategies [1]. Film capacitors or ceramic capacitors are known to be more reliable, but are far more expensive for the same capacitance. Nevertheless, [19] employs an active filter technique that uses less capacitance to store the same amount of energy, thus making the use of film or ceramic capacitors feasible and providing inverters with the reliability levels needed to support 25-year life. This active filter technique is analyzed in Chapter 4. Therefore, without the need to replace inverters once or twice, the lifetime cost of a PV system will be reduced.

1.3.3 Better Energy Yield and System Reliability

Complete or partial shadowing of one or more of the ac PV modules in a PV system only affects the energy yield of the respective module(s) and not the entire PV system. To better illustrate the improvement in power output by using ac PV modules, two systems were simulated, each representative of a typical 2-kW system, having ten 185-W PV modules. One of the systems uses a standard string inverter with the PV modules connected in series and MPPT performed on the entire string. The other system uses ac PV modules, with individual MPPT, connected in parallel. The setups for these two systems are shown in Fig. 1.10. For each system, the number of modules affected by shadowing is incremented and, for each case, the irradiance level is varied from 1 kW/m^2 (full sun) to 0 kW/m^2 (no sun) and the power delivered to the load is recorded. The additional power that can be obtained by using ac PV modules is then computed. The outcome in Fig. 1.11 shows that, in the best case, a system with ac PV modules can yield more than an additional 350 W.

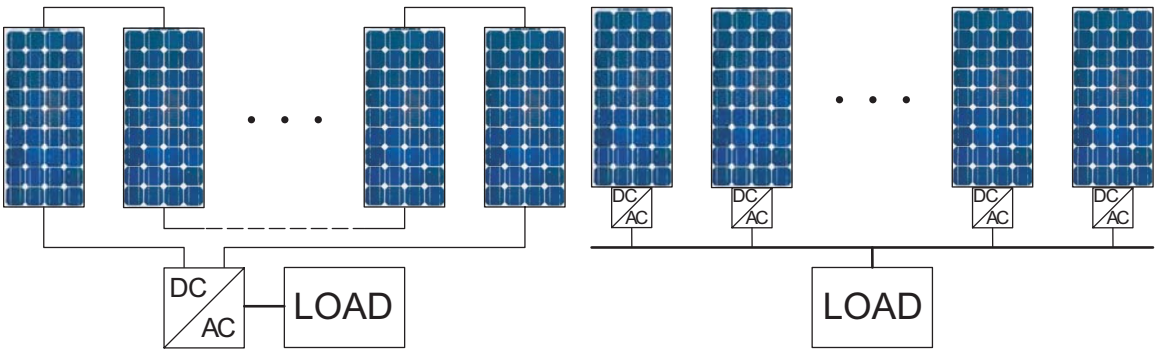


Fig. 1.10 Setups for two different PV systems: PV system with string inverter (left) and PV system with ac PV modules (right)

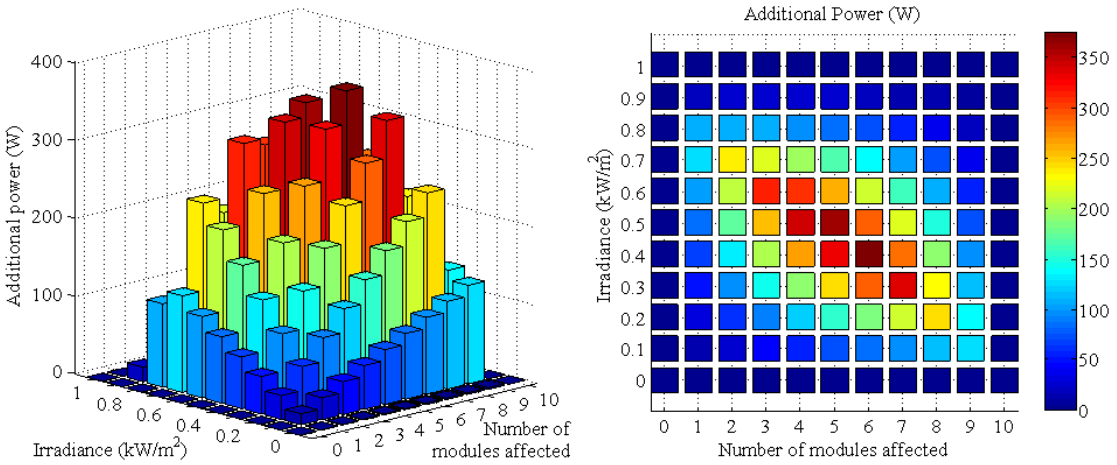


Fig. 1.11 Additional power yielded by using ac PV modules instead of a string inverter

Another limitation of centralized or string inverters is that all the PV modules have to be at the same tilt angle in order to prevent power mismatch. As mentioned previously, this is not a problem for ac PV modules, and they can thus be more easily adapted to odd roof-lines with different tilt angles and orientations, without considerably compromising the overall power output of the PV system. More importantly, better system reliability is achieved with the modularity of ac PV modules. If one of the modules is lost due to some failure in each system, the string inverter system is completely brought down while the modular system remains functional as the ac PV modules continue to supply power to the load. Moreover, the use of ac PV modules eliminates the need for special, properly sized dc cables that carry high currents at lower voltages, thus simplifying system design and improving system efficiency by eliminating dc losses.

1.3.4 Microinverter Topologies for AC PV Modules

Although ac PV modules are not currently available on the market, they have been the subject of much research, development, and attempted market penetration over the past couple of decades [20-22]. Ascension Technology, Inc., started development of ac PV modules in 1991 [21] and started shipping them in 1997 [23]. In 1995, OKE-Services developed microinverters [20], which were integrated on PV modules and shipped by NKF Kabel B.V. in 1996 [23]. However, supply of these ac PV modules on the market was short-lived—Applied Power Corporation bought Ascension Technology and discontinued its ac PV module line in 2001 and NKF Kabel stopped production of the microinverters in 2003 when a Dutch subsidy program ended [23].

In 2006, researchers in [22] claimed to be very close to having a fully operational ac PV module, but only presented a prototype, which required further development to reach the performance of string and central inverters; there has not been any update since then. On the other hand, there are companies such as Enphase Energy and Petra Solar that are currently marketing microinverters, which are only warranted for up to 15 years. As a result, they are not directly attached to PV modules, have exposed dc wiring, and do not qualify as ac PV modules. It is apparent that ac PV modules are not realizable unless reliability of the microinverters can match that of PV modules—this is highly dependent on the circuit topology of the microinverters.

References [24] and [25] have reviewed most of the ac PV module microinverter topologies that have been used in commercial ac PV modules and introduced in the literature. Since the majority of PV modules on the market output low dc voltage, the basic requirement for microinverters is to provide voltage amplification and dc–ac inversion in their power conversion stage [24]. Generally, voltage amplification can be realized by using either a line-frequency transformer or a high-frequency transformer as shown in Fig. 1.12.

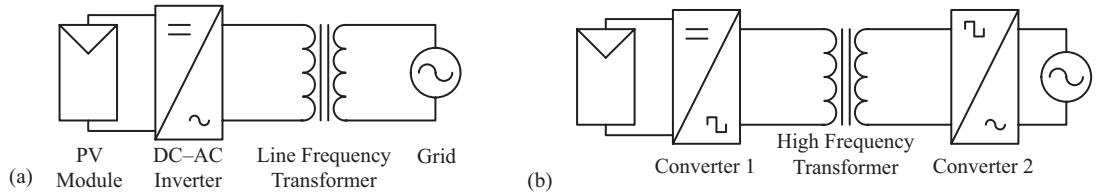


Fig. 1.12 Possible microinverter topologies as shown in [24]: (a) with line-frequency transformer and (b) with high-frequency transformer

In Fig. 1.12 (a), voltage amplification by the line-frequency transformer is preceded by a dc–ac inversion stage. Since a microinverter is an integral part of the assembly in an ac PV module, compactness is desired, meaning that a high power density is important [24]. However, line-frequency transformers tend to be bulky and may not be very efficient. Interestingly, this was the topology employed by Ascension Technology for its ac PV module [21]. For the reasons above, microinverters with high-frequency transformers are preferred. Depending on the configuration of Converter 2 in Fig. 1.12 (b), microinverters with high-frequency transformers can be classified as having either a dc link, a pseudo dc link, or no dc link, as shown in Fig. 1.13 (a), (b), and (c), respectively [24].

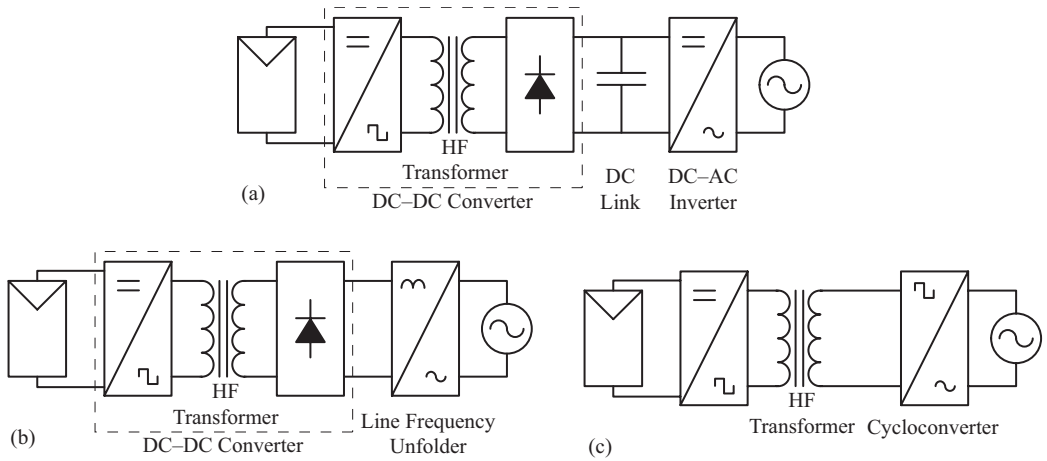


Fig. 1.13 Classification of microinverters with high-frequency transformers [24]: microinverter with (a) dc link, (b) pseudo dc link, and (c) no dc link

In Fig. 1.13 (a), the input converter, the high-frequency transformer, and the rectifier form a dc–dc converter, which is basically an isolated boost converter that amplifies the low dc voltage from the PV module to a higher dc voltage for the dc link, before the dc–ac inversion takes place. The dc–dc converter in the pseudo dc link microinverter in Fig. 1.13 (b) is slightly different, in that it is modulated to provide a rectified sinusoidal voltage to the output stage, where it is unfolded to match the grid voltage. The third configuration does not include any dc link. The input stage converts the dc voltage from the PV module to a high-frequency square wave. After the square wave is amplified by the high-frequency transformer, an ac–ac converter (cycloconverter) is used to reconstruct a sinusoidal voltage or current waveform at the line frequency.

While there are very many different commercial and experimental circuits, as shown in [24] and [25], that can be categorized as one of the above topologies, for the sake of brevity of this document, they will not be individually addressed and analyzed here. Nevertheless, the authors in [24] strongly believe that the microinverter topology without a dc link "may become the trend for the development of the next generation" of microinverters. One major advantage of this topology over the other high-frequency transformer topologies is that there are only two power conversion stages. This implies that there is the possibility for fewer components, higher reliability, better efficiency, and lower overall cost. However, the authors in [24] find constructing bidirectional switches needed for the output converter to be a challenge and claim that more sophisticated controls are needed due to the loss of an intermediate energy storage stage.

1.4 Initially Proposed Microinverter

The cycloconverter-type high-frequency link inverter, proposed in [26] and shown in Fig. 1.14, was initially introduced and intended for fuel cell applications. Yet, this topology is very much like that shown in Fig. 1.13 (c), with a typical full-bridge inverter at the input to generate a high-frequency square wave, a high-frequency transformer to amplify the square wave, and a cycloconverter at the output to generate a line-frequency sinusoidal wave. At first glance, this particular topology seems to lend itself well to an ac PV module microinverter. Moreover, it resolves the challenges of constructing bidirectional switches and eliminates the need for more complex controls, as mentioned at the end of Section 1.3.4. The bidirectional switches for the cycloconverter are implemented with anti-parallel thyristors, which are controlled by a state machine.

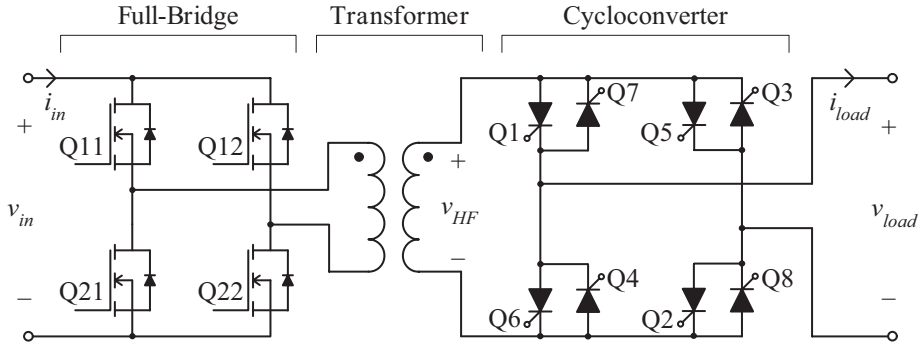


Fig. 1.14 Cycloconverter-type high-frequency link inverter proposed in [26]

The state machine in Fig. 1.15 was introduced and analyzed in [27], where it was shown to solve the cycloconverter-related issue of current commutation by generating switching signals to turn on the appropriate pairs of thyristors at the appropriate time. According to [27], while the load current changes sign, "improper switching can cause commutation failure where either the source is short-circuited or the load current is interrupted"—situations capable of causing high current or voltage that can damage the circuit. There are only four allowable states in the state machine. Depending on HFPOL, the polarity of the high-frequency voltage square wave v_{HF}, and IP and IN, the load current i_{load} polarity signals based on some fixed thresholds, the state machine moves from one state to another and outputs the switching signals to turn on the appropriate pair of thyristors. These switching signals are governed by the *delay* (DE) and *advance* (AD) pulse width modulation (PWM) signals, obtained from a multiple-carrier PWM technique covered in [26].

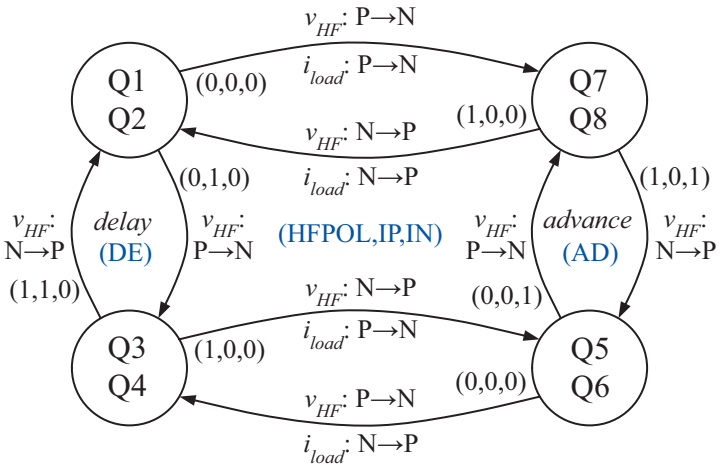


Fig. 1.15 State machine for cycloconverter control [27]

1.4.1 Hardware Implementation

The authors in [27] implemented the inverter, along with the state machine, in hardware. A 30-V dc voltage supply was used as the input source and a 6.2-Ω resistor R in series with a 35-mH inductor L as the load, with a switching frequency of 1 kHz. Figure 1.16 shows the waveforms and logic signals recorded from their experiment. The current i_{load} is sinusoidal at the line frequency, although there is some low-frequency distortion. The conversion from a high-frequency square wave to a low-frequency sinusoid can be clearly noted. It is also interesting to see how the DE and AD pulses are steered based on HFPOL, IP, and IN to generate the switching signals for the thyristors.

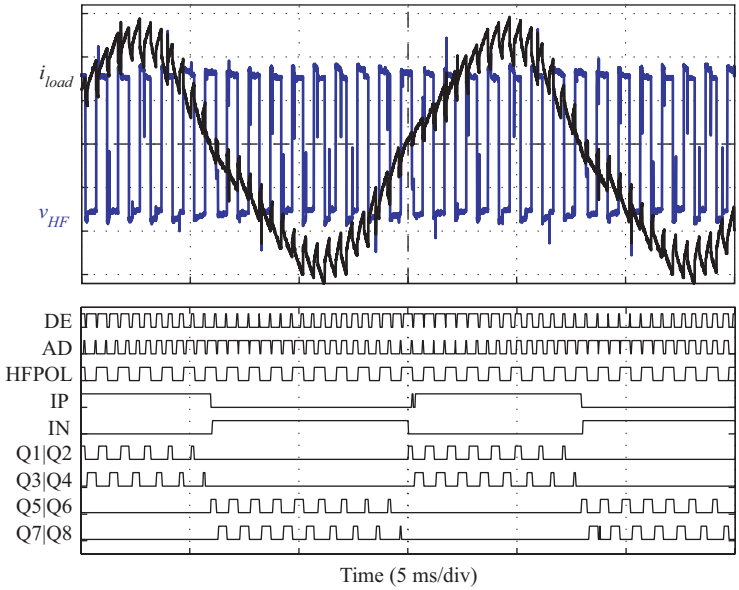


Fig. 1.16 Experimental waveforms and logic signals for initially proposed microinverter [27]

1.4.2 Simulation

The hardware results being promising, for further tests and observations, the cycloconverter-type inverter was modeled in Dymola [28], as illustrated in Fig. 1.17. The control block implements the state machine and generates all the switching signals. The model was simulated using the same settings as the hardware implementation, but with ideal components. The simulated waveforms and logic signals are shown in Fig. 1.18. The logic signals are practically similar to those shown in Fig. 1.16. In the absence of non-ideal components, i_{load} is much cleaner, with no apparent low-frequency distortion and no commutation failure. The load voltage v_{load} is shown here, instead of v_{HF}, to show how v_{HF} is modulated by the cycloconverter to produce a PWM voltage across the load. The low line-frequency content of this PWM voltage is easily separated and recovered from its high-frequency switching content by the low-pass characteristic of the *R*-*L* load.

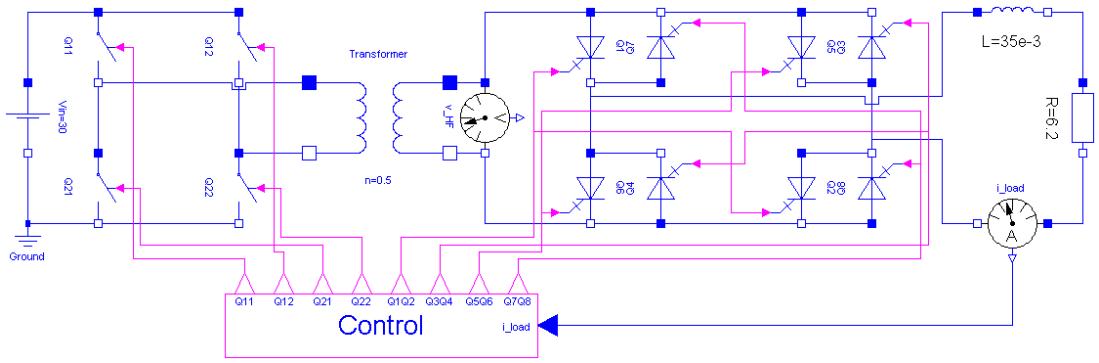


Fig. 1.17 Dymola simulation setup for initially proposed microinverter

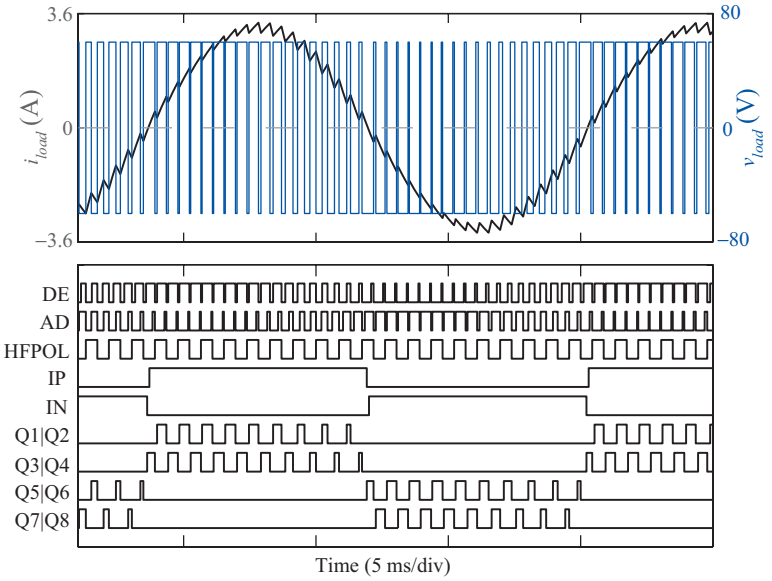


Fig. 1.18 Simulation waveforms and logic signals from Dymola setup

1.4.3 Limitations

To test the feasibility of using the cycloconverter-type inverter as the microinverter of a grid-connected ac PV module, it needs to be simulated with a PV module as its source and the ac grid as its load. One example of doing this is shown in Fig. 1.19, where L_{in} and C_{in} form an input filter and L_{out} an output filter. There are other possible configurations, but this one is probably the simplest. Capacitor C_{in} also serves as the energy storage of the energy flowing to and from the ac load at double its frequency.

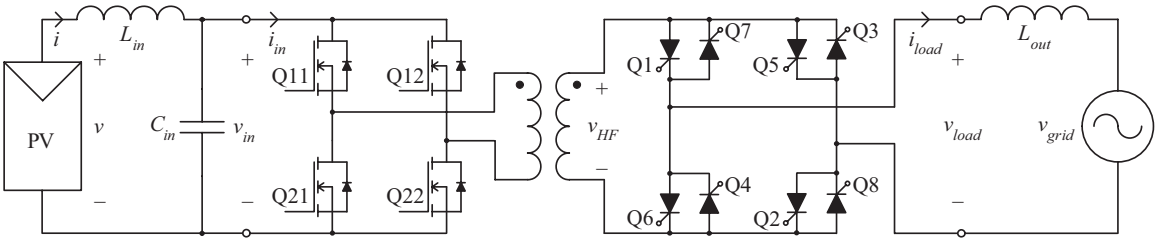


Fig. 1.19 Grid-tied cycloconverter-type inverter with PV source

The goal of a microinverter is to deliver the maximum available power from the PV module to the ac grid while meeting all the regulatory codes and standards, which are discussed in detail in Chapter 3. The current i_{load} injected in the ac grid has to meet well-defined harmonic limits and is usually desired to be in phase with grid voltage v_{grid} for unity power factor. However, simulations showed that the setup in Fig. 1.19 can get close to meeting these requirements only at the expense of excessively big, maybe unrealistic, passive components.

For example, with a BP 7185 [29] 185-W PV module model, 240-V grid voltage, and the switching frequency increased to 4 kHz, L_{in}, C_{in}, and L_{out} had to be set at 1 mH, 1600 μF, and 342 mH, respectively, to generate the waveforms shown in Fig. 1.20. At a relatively low input voltage, a high capacitance is needed for C_{in} to manage the double-frequency energy, while minimizing the variation in the voltage v_{in}. Along with C_{in}, L_{in} is sized to form a low-pass filter, adequate to filter out the switching ripple from i_{in}. On the other hand, it was found that the load has to be inductive enough for the state machine to provide the right switching signals to the cycloconverter for proper current commutation. A 342-mH inductance for L_{out} provides the needed impedance.

Such a big C_{in} was still not adequate to prevent the voltage oscillation across it from being about 8 V peak-to-peak—higher than desired. This not only imposes excessive ripple on the PV module, shown by the ripple in its power p, but also introduces

distortion in i_{load}, mostly third harmonic in this case. Not only is the energy yield from the PV module affected, but so is the quality of the power delivered to the grid. These can be improved by further increasing C_{in}, but this does not seem to be the best solution.

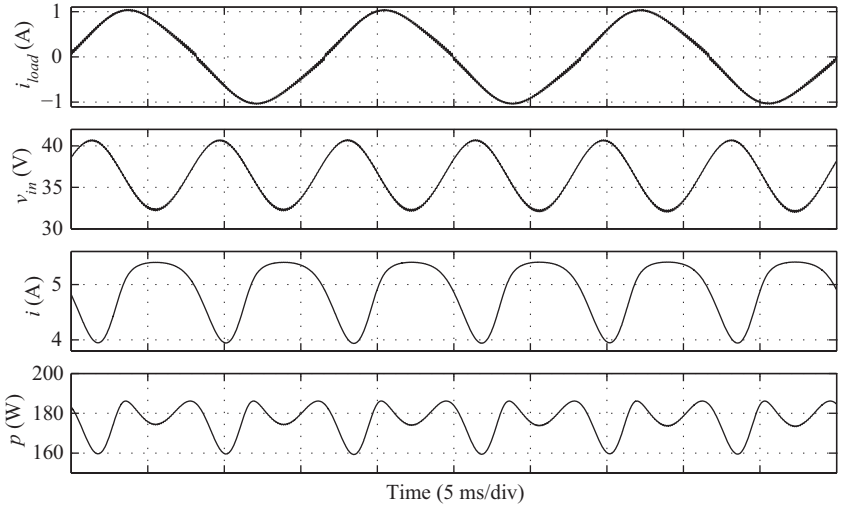


Fig. 1.20 Waveforms with PV source and input filter

Adding a third port as discussed in [19] to manage the double-frequency energy might alleviate the poor energy yield and power quality, but will not significantly change the requirement of the input and output filters. Unless the switching frequency—which is currently limited by the thyristors—can be drastically increased and the state machine changed such that an inductive load is not necessary, decreasing the size of these passive components is not trivial. It is clear that considerable research and development have to be done, mainly in the design of thyristors that can allow much higher switching frequency, but this is beyond the scope of this dissertation.

The bottom line is that, as of now, the cycloconverter-type inverter does not lend itself well to an ac PV module application and is not suitable for this research work, which aims at developing a complete ac PV module model along with all the required controls for maximum energy yield and successful compliance with regulatory codes and standards. Such an ac PV module model should provide a good platform to test different control algorithms and analyze the behavior of PV systems with multiple ac PV modules.

1.5 Alternative Microinverter

Due to the limitations of the cycloconverter-type inverter, an alternative microinverter based on Fig. 1.13 (a) has been identified for the purpose of modeling, developing, and

analyzing an ac PV module, including its controls. The detailed structure of this microinverter is presented in Fig. 1.21. As mentioned in Section 1.3.4, the input stage is an isolated boost converter connected to a typical full-bridge converter output stage through a dc link/bus. Both stages can use MOSFETs as switches, which can be controlled by conventional PWM techniques, thus allowing for much higher switching frequencies and smaller filter components.

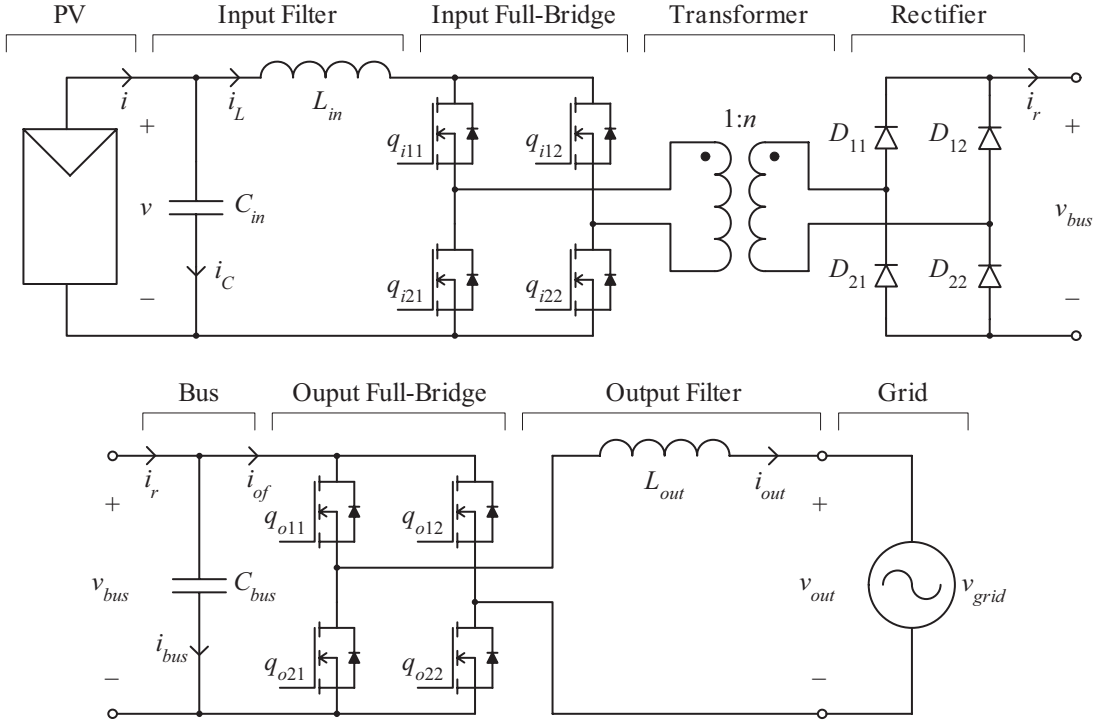


Fig. 1.21 Alternative microinverter with PV source and grid-tied

The input and output stages will first be investigated separately in Chapters 2 and 3, respectively, and then together in Chapter 4. Chapter 2 starts with modeling the PV module, followed by the development of the input control needed for the robust and fast maximum power point tracking (MPPT) of the PV module. The controls required for the safe interconnection of the output stage with the utility grid are developed and analyzed in Chapter 3. In Chapter 4, both stages are put together and two ways of managing the double-frequency energy storage are examined. Since typical PV systems will more likely consist of multiple ac PV modules, it is crucial to understand their dynamics and interactions with the utility grid. Therefore, Chapter 5 analyzes PV systems with up to 10 ac PV modules under different operating and atmospheric conditions.

2 INPUT STAGE

2.1 Overview

The input stage of the proposed microinverter, introduced in Section 1.5, is shown in Fig. 2.1. The input stage is basically an isolated boost converter connected to a photovoltaic (PV) module through a low-pass input filter made up of L_{in} and C_{in}. The isolated boost converter consists of a full-bridge inverter, a transformer, and a rectifier as in Fig. 2.1. The purpose of the input stage is to maximize the energy yield from the PV module at all times and boost the PV module voltage to a high enough bus voltage v_{bus} to ensure the proper operation of the output stage, which will be covered in Chapter 3.

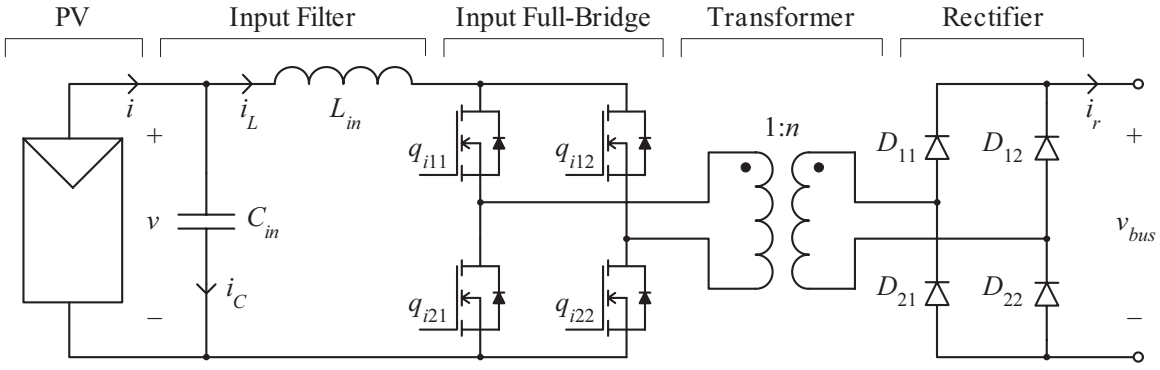


Fig. 2.1 Microinverter input stage

PV modules exhibit a nonlinear relationship between the voltage v across their terminals and the current i coming out of the terminals. An example of such a characteristic curve, along with the resulting power curve, is shown in Fig. 2.2.

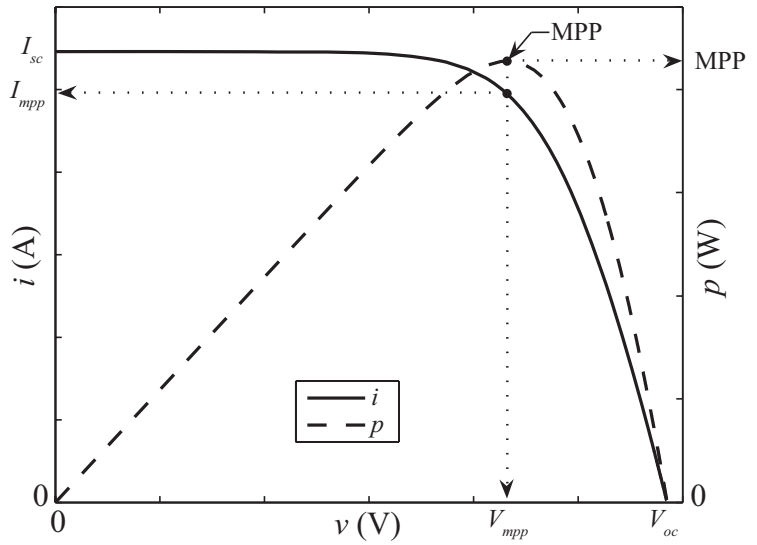


Fig. 2.2 Example of characteristic *i*-*v* curve of a PV module

In Fig. 2.2,

- i = PV module current,
- v = PV module voltage,
- I_{sc} = short-circuit current ($v = 0$),
- V_{oc} = open-circuit voltage ($i = 0$),
- p = PV module power ($p = iv$),
- MPP = maximum power point,
- I_{mpp} = current at the maximum power point, and
- V_{mpp} = voltage at the maximum power point.

The current i is highly dependent on the amount of **in**cident **sol**ar radi**ation**, often called insolation G, on the PV module while the voltage v is more dependent on temperature T. Exaggerated examples of these phenomena are illustrated in Fig. 2.3.

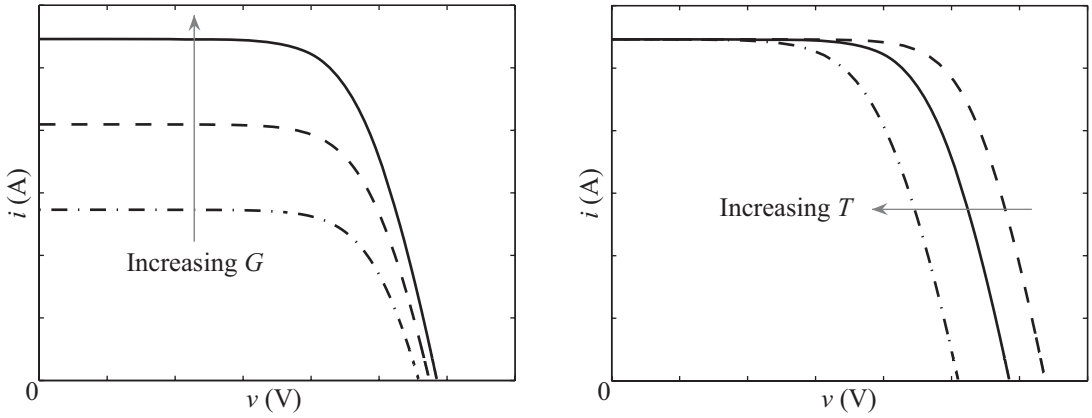


Fig. 2.3 Effects of insolation (left) and temperature (right) on a PV characteristic curve [30]

Throughout the day, varying G and T due to changing atmospheric conditions lead to continuously varying i and v. Consequently, the MPP is expected to be constantly changing. Therefore, the control of the microinverter input stage needs to include a maximum power point tracking (MPPT) algorithm [18] to continuously track the MPP of the PV module such that its energy harvest is maximized.

In Section 2.2, a set of equations will be derived to model any given PV module available on the market, based on parameters from its datasheet. It will be shown that the model perfectly matches characteristic curves from a datasheet and adequately captures the effects of insolation and temperature. After that, an improved version of a perturb-and-observe (P&O) MPPT algorithm will be reviewed in Section 2.3 and its performance

will be analyzed by using the PV module model connected to a conventional boost converter in Section 2.4. The conventional boost converter can be substituted by the isolated boost converter by simply manipulating the switching signal of the former as covered in Section 2.5. Section 2.6 will demonstrate that a simple average-value model (AVM) can be used for either the boost or isolated boost converter without the loss of the essential behaviors and dynamics of the system.

2.2 PV Module Model

In order to review the performance of the MPPT algorithm in simulation, it is necessary to have a PV module model that can accurately represent the current-voltage (*i*-*v*) characteristic curve of any given PV module, under any atmospheric condition. In the literature [31-36], one common model used for a PV module is that shown in Fig. 2.4.

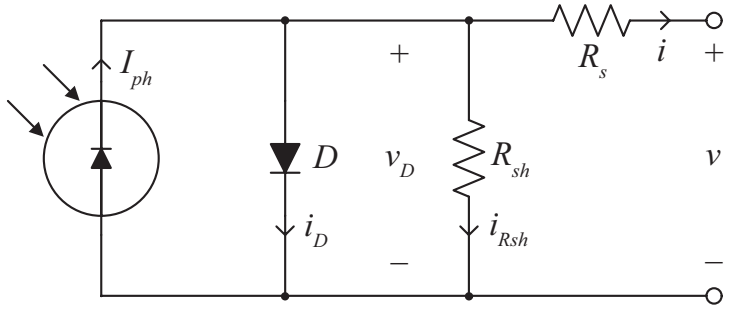


Fig. 2.4 PV module model

In Fig. 2.4,

- I_{ph} = current generated by the photosensitive diode,
- R_s = PV module series resistance, and
- R_{sh} = PV module shunt resistance.

Using KCL,

$$i = I_{ph} - i_D - i_{Rsh}\,. \tag{2.1}$$

The well-known diode current i_D [37] is given by

$$i_D = I_s\left(e^{v_D/(nV_T)} - 1\right), \tag{2.2}$$

where

- I_s = reverse bias saturation current of the diode,
- n = emission coefficient, also known as the diode ideality factor, and
- V_T = diode junction thermal voltage given by

$$V_T = \frac{kT}{q}. \tag{2.3}$$

In (2.3),

- k = Boltzmann's constant = 1.38065×10^{-23} J/K
- T = the absolute temperature in kelvins = 273 + temperature in °C, and
- q = the magnitude of electronic charge, 1.602×10^{-19} C.

If a PV module consists of N cells in series, where each cell is effectively a p-n junction, it suffices to multiply (2.3) by N. Using KVL, the voltage v_D across the diode can be expressed in terms of i and v as

$$v_D = v + iR_s. \tag{2.4}$$

Combining (2.1), (2.2), and (2.4) results in

$$i = I_{ph} - I_s\left(e^{\frac{v+iR_s}{nNV_T}} - 1\right) - \frac{v+iR_s}{R_{sh}}. \tag{2.5}$$

Equation (2.5) is usually termed the single exponential model. During forward-bias conditions, the exponential term in the diode equation dominates; as a result, it is common to approximate (2.5) by

$$i = I_{ph} - I_s e^{\frac{v+iR_s}{nNV_T}} - \frac{v+iR_s}{R_{sh}}. \tag{2.6}$$

One might quickly realize that using either (2.5) or (2.6) to model and match the i-v characteristic curve of a given PV module is not an easy task, unless I_{ph}, I_s, R_s, R_{sh}, and n are known. These parameters, which are generally not provided in the datasheets of PV modules from manufacturers, are, however, solved for in [36] by using parameters that are given in the datasheets. In addition to providing I_{sc}, V_{oc}, I_{mpp}, and V_{mpp} under standard test conditions (STC, i.e. G = 1000 W/m^2 and T = 25 °C) and m, PV module datasheets also provide

- k_i = temperature coefficient (in %/K) of the short-circuit current I_{sc}, and
- k_v = temperature coefficient (in V/K) of the open-circuit voltage V_{oc},

which will be important in capturing the effect of temperature in the PV module model.

Since there are five unknowns, at least five equations are needed to solve for them. The first three equations are obtained by substituting the three known points on the i-v

curve—short-circuit (0, I_{sc}), open-circuit (V_{oc}, 0), and maximum power (V_{mpp}, I_{mpp})—into (2.6):

$$I_{sc} = I_{ph} - I_s e^{\frac{I_{sc}R_s}{nNV_T}} - \frac{I_{sc}R_s}{R_{sh}} \tag{2.7}$$

$$0 = I_{ph} - I_s e^{\frac{V_{oc}}{nNV_T}} - \frac{V_{oc}}{R_{sh}} \tag{2.8}$$

$$I_{mpp} = I_{ph} - I_s e^{\frac{V_{mpp}+I_{mpp}R_s}{nNV_T}} - \frac{V_{mpp}+I_{mpp}R_s}{R_{sh}} \tag{2.9}$$

The fact that the derivative of p with respect to v is zero at the MPP leads to the fourth equation:

$$\left.\frac{dp}{dv}\right|_{\substack{v=V_{mpp}\\ i=I_{mpp}}} = 0\,. \tag{2.10}$$

The fifth equation results from the negative slope of the i-v curve under the short-circuit condition. As pointed out in [36], the slope is mainly determined by the shunt resistance R_{sh}, such that

$$\left.\frac{di}{dv}\right|_{\substack{v=0\\ i=I_{sc}}} = -\frac{1}{R_{sh}}\,. \tag{2.11}$$

2.2.1 Parameter Extraction

From (2.8),

$$I_{ph} = I_s e^{\frac{V_{oc}}{nNV_T}} + \frac{V_{oc}}{R_{sh}}\,. \tag{2.12}$$

Substituting (2.12) into (2.7) leads to

$$I_{sc} = I_s\left(e^{\frac{V_{oc}}{nNV_T}} - e^{\frac{I_{sc}R_s}{nNV_T}}\right) + \frac{V_{oc}-I_{sc}R_s}{R_{sh}}\,. \tag{2.13}$$

According to [36], since $e^{\frac{V_{oc}}{nNV_T}} >> e^{\frac{I_{sc}R_s}{nNV_T}}$,

$$I_{sc} = I_s e^{\frac{V_{oc}}{nNV_T}} + \frac{V_{oc}-I_{sc}R_s}{R_{sh}}\,. \tag{2.14}$$

I_s can thus be solved from (2.14):

$$I_s = \left(I_{sc} - \frac{V_{oc} - I_{sc}R_s}{R_{sh}} \right) e^{-\frac{V_{oc}}{nNV_T}}. \tag{2.15}$$

Substituting I_{ph} and I_s found in (2.12) and (2.15), respectively, results in

$$\begin{aligned} I_{mpp} = & \left[\left(I_{sc} - \frac{V_{oc} - I_{sc}R_s}{R_{sh}} \right) e^{-\frac{V_{oc}}{nNV_T}} \right] e^{\frac{V_{oc}}{nNV_T}} + \frac{V_{oc}}{R_{sh}} + \ldots \\ & - \left[\left(I_{sc} - \frac{V_{oc} - I_{sc}R_s}{R_{sh}} \right) e^{-\frac{V_{oc}}{nNV_T}} \right] e^{\frac{V_{mpp} + I_{mpp}R_s}{nNV_T}} - \frac{V_{mpp} + I_{mpp}R_s}{R_{sh}}, \end{aligned} \tag{2.16}$$

which simplifies to

$$I_{mpp} = I_{sc} - \frac{V_{mpp} + I_{mpp}R_s - I_{sc}R_s}{R_{sh}} - \left(I_{sc} - \frac{V_{oc} - I_{sc}R_s}{R_{sh}} \right) e^{\frac{V_{mpp} + I_{mpp}R_s - V_{oc}}{nNV_T}}. \tag{2.17}$$

Equation (2.17) is not only valid at the MPP, but also at any other point on the *i*-*v* curve. Therefore, the following expression can be written:

$$i = f(i,v) = I_{sc} - \frac{v + iR_s - I_{sc}R_s}{R_{sh}} - \left(I_{sc} - \frac{V_{oc} - I_{sc}R_s}{R_{sh}} \right) e^{\frac{v + iR_s - V_{oc}}{nNV_T}}. \tag{2.18}$$

To obtain an explicit expression for (2.11), the derivative of (2.18) with respect to voltage is needed. This can be done by differentiating (2.18) [36] as

$$di = di \frac{\partial}{\partial i} f(i,v) + dv \frac{\partial}{\partial v} f(i,v) \tag{2.19}$$

and rearranging terms

$$\frac{di}{dv} = \frac{\frac{\partial}{\partial v} f(i,v)}{1 - \frac{\partial}{\partial i} f(i,v)}. \tag{2.20}$$

The partial derivatives in (2.20) can be expressed as

$$\frac{\partial}{\partial v} f(i,v) = -\left(\frac{I_{sc}R_{sh} - V_{oc} + I_{sc}R_s}{nNV_T R_{sh}} \right) e^{\frac{v + iR_s - V_{oc}}{nNV_T}} - \frac{1}{R_{sh}} \tag{2.21}$$

and

$$\frac{\partial}{\partial i} f(i,v) = -R_s \left(\frac{I_{sc}R_{sh} - V_{oc} + I_{sc}R_s}{nNV_T R_{sh}} \right) e^{\frac{v + iR_s - V_{oc}}{nNV_T}} - \frac{R_s}{R_{sh}}. \tag{2.22}$$

Substituting (2.21) and (2.22) into (2.20):

$$\frac{di}{dv}=\frac{-\left(\frac{I_{sc}R_{sh}-V_{oc}+I_{sc}R_s}{nNV_TR_{sh}}\right)e^{\frac{v+iR_s-V_{oc}}{nNV_T}}-\frac{1}{R_{sh}}}{1+R_s\left(\frac{I_{sc}R_{sh}-V_{oc}+I_{sc}R_s}{nNV_TR_{sh}}\right)e^{\frac{v+iR_s-V_{oc}}{nNV_T}}+\frac{R_s}{R_{sh}}}. \tag{2.23}$$

Evaluating (2.23) at the short-circuit point, as stated in (2.11), results in

$$\frac{-\left(\frac{I_{sc}R_{sh}-V_{oc}+I_{sc}R_s}{nNV_TR_{sh}}\right)e^{\frac{I_{sc}R_s-V_{oc}}{nNV_T}}-\frac{1}{R_{sh}}}{1+R_s\left(\frac{I_{sc}R_{sh}-V_{oc}+I_{sc}R_s}{nNV_TR_{sh}}\right)e^{\frac{I_{sc}R_s-V_{oc}}{nNV_T}}+\frac{R_s}{R_{sh}}}=-\frac{1}{R_{sh}}, \tag{2.24}$$

which is erroneously reported in [36]. Furthermore, the derivative of power with respect to voltage can be written as

$$\frac{dp}{dv}=\frac{d\left(iv\right)}{dv}=i+\frac{di}{dv}v. \tag{2.25}$$

Therefore, with (2.23) inserted into (2.25) and evaluated at the maximum power point as in (2.10),

$$I_{mpp}+V_{mpp}\frac{-\left(\frac{I_{sc}R_{sh}-V_{oc}+I_{sc}R_s}{nNV_TR_{sh}}\right)e^{\frac{V_{mpp}+I_{mpp}R_s-V_{oc}}{nNV_T}}-\frac{1}{R_{sh}}}{1+R_s\left(\frac{I_{sc}R_{sh}-V_{oc}+I_{sc}R_s}{nNV_TR_{sh}}\right)e^{\frac{V_{mpp}+I_{mpp}R_s-V_{oc}}{nNV_T}}+\frac{R_s}{R_{sh}}}=0, \tag{2.26}$$

which is also incorrectly reported in [36]. Finally, Equations (2.17), (2.24), and (2.26) can be solved iteratively for R_s, R_{sh}, and n. An example of a MATLAB code used for the iteration is given in Appendix A. As an example, the datasheet values for the BP Solar BP 7185 module [29] are V_{oc} = 44.8 V, I_{sc} = 5.5 A, V_{mpp} = 36.5 V, I_{mpp} = 5.1 A, and N = 72 and the extracted parameters are R_s = 0.2614 Ω, R_{sh} = 1474 Ω, and n = 1.4061.

2.2.2 Model Formulation

Now that R_s, R_{sh}, and n are known, it is possible to formulate the characteristic *i-v* curve of a PV module as per Equation (2.5). However, it is important to capture the effects of insolation G and temperature T on the curve. While R_s, R_{sh}, and n can be assumed to be independent of G and T, this is not the case for I_{ph} and I_s. By applying the principle of superposition [36], the dependence of I_{ph} and I_s on temperature and insolation is derived below.

2.2.2.1 *Temperature effects*

The open-circuit voltage V_{oc} varies with T based on the temperature coefficient k_v such that

$$V_{oc}(T) = V_{oc} + k_v (T - T_{STC}), \tag{2.27}$$

where T_{STC} is the temperature at STC, i.e. 25 °C or 298 K. On the other hand, the temperature coefficient k_i dictates the variation in the short-circuit current I_{sc} as

$$I_{sc}(T) = I_{sc}\left[1 + \frac{k_i}{100}(T - T_{STC})\right]. \tag{2.28}$$

The fact that V_{oc} and I_{sc} vary with T implies that, from (2.12) and (2.15), the photo-generated current I_{ph} and the saturation current I_s also vary with T as follows:

$$I_s(T) = \left(I_{sc}(T) - \frac{V_{oc}(T) - I_{sc}(T)R_s}{R_{sh}}\right) e^{-\frac{V_{oc}(T)}{nNV_T}} \tag{2.29}$$

$$I_{ph}(T) = I_s(T) e^{\frac{V_{oc}(T)}{nNV_T}} + \frac{V_{oc}(T)}{R_{sh}} \tag{2.30}$$

2.2.2.2 *Insolation effects*

As widely reported in the literature, I_{sc} is directly proportional to G:

$$I_{sc}(G,T) = I_{sc}(T)\frac{G}{G_{STC}}, \tag{2.31}$$

where G_{STC} is the insolation at STC, i.e. 1000 W/m^2. To find the insolation dependence of V_{oc}, it can be assumed that I_{ph} is also directly proportional to G:

$$I_{ph}^* = I_{ph}(T)\frac{G}{G_{STC}}. \tag{2.32}$$

Then, using Equation (2.8),

$$V_{oc}(G,T) = \ln\left(\frac{I_{ph}^* R_{sh} - V_{oc}(G,T)}{I_s(T) R_{sh}}\right) nNV_T, \tag{2.33}$$

which is a transcendental equation in $V_{oc}(G,T)$ and needs to be solved iteratively for $V_{oc}(G,T)$. Therefore, with $I_{sc}(G,T)$ and $V_{oc}(G,T)$ found from (2.31) and (2.33), the temperature/insolation-dependent I_s and I_{ph} can be expressed as follows:

$$I_s(G,T) = \left(I_{sc}(G,T) - \frac{V_{oc}(G,T) - I_{sc}(G,T)R_s}{R_{sh}}\right) e^{-\frac{V_{oc}(G,T)}{nNV_T}} \tag{2.34}$$

$$I_{ph}(G,T) = I_s(G,T)e^{\frac{V_{oc}(G,T)}{nNV_T}} + \frac{V_{oc}(G,T)}{R_{sh}} \tag{2.35}$$

Finally, the formulation of the PV module characteristic curve is given by

$$i = I_{ph}(G,T) - I_s(G,T)\left(e^{\frac{v+iR_s}{nNV_T}} - 1\right) - \frac{v+iR_s}{R_{sh}}. \tag{2.36}$$

2.2.2.3 Breakdown region

Based on reference [31], (2.36) can be further extended to include the PV module reverse characteristics, which is important in modeling the effects of partial shading [36]. This is done by adding a factor to the last term in (2.36), such that

$$i = I_{ph}(G,T) - I_s(G,T)\left(e^{\frac{v+iR_s}{nNV_T}} - 1\right) - \frac{v+iR_s}{R_{sh}}\left[1 + a\left(1 - \frac{v+iR_s}{NV_{br}}\right)^{-m}\right], \tag{2.37}$$

where

- a = fraction of ohmic current involved in the avalanche breakdown,
- m = avalanche breakdown exponent,
- and V_{br} = cell junction breakdown voltage.

2.2.3 Simulated Characteristic Curves

Given the required datasheet parameters, with the equations derived above, the characteristic curve of any PV module can be simulated under any given temperature and insolation. However, for this PV module model to be used as a source in the simulation of a power electronic converter, the simulation tool must be able to solve for i and v, not only under fixed or varying temperature and/or insolation, but also based on the continuous operation of the converter—current ripple imposed by the switching action of the converter on the PV module, for example. Dymola [28], a hybrid simulator, lends itself well to simulating this PV module model under all these conditions by seamlessly solving the set of algebraic and transcendental equations for i and v.

In Dymola, the above equations can be bundled into a block to represent the PV module source. The icon created for this block is shown in Fig. 2.5, while the code within the block, written in Modelica modeling language, is provided in Appendix A. Input interfaces to the blocks allow the insolation G and temperature T to be set by external signals. To obtain the i-v curve of the PV module model block at a given T and G, v can

be swept from 0 to V_{oc}. Alternatively, i can be swept from 0 to I_{sc}. The Dymola setup to sweep v, using additional built-in blocks from the Modelica library, is shown in Fig. 2.6.

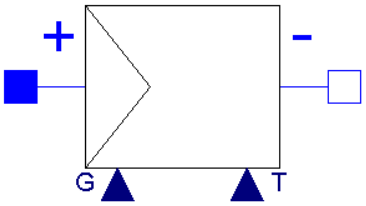


Fig. 2.5 Dymola PV module model block

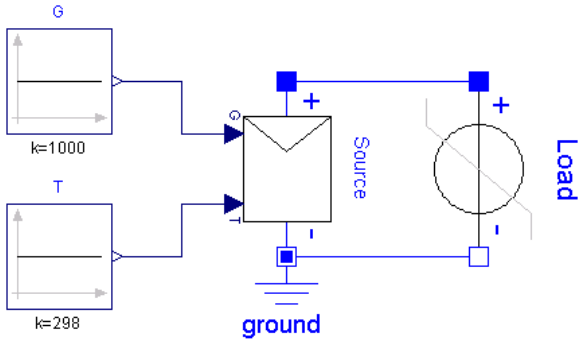


Fig. 2.6 Voltage sweep simulation setup

The datasheet parameters from the BP Solar BP 7185 PV module [29], along with its extracted parameters (given above), were input into the PV module model block. Figure 2.7 shows how, at different values of T with G fixed at 1000 W/m^2, the simulated current-voltage curves match those of the datasheet, which are usually empirically obtained.

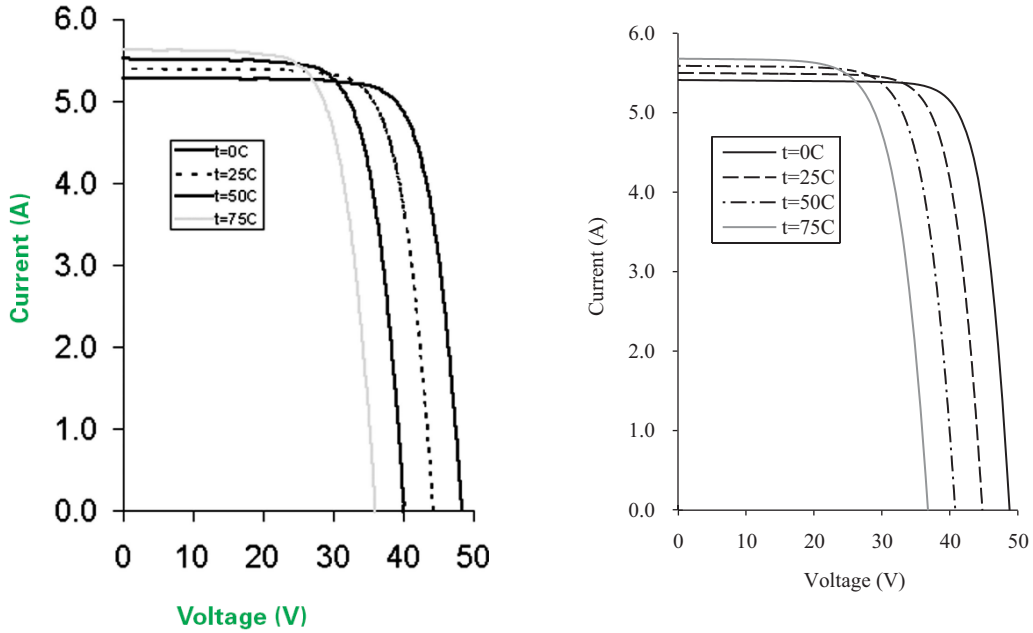


Fig. 2.7 Good correlation between datasheet (left) [29] and simulated (right) i-v curves under varying T

With the temperature kept constant at 298 K (25 °C), varying the insolation from 100 to 1000 W/m^2, in increments of 100 W/m^2, leads to the *i*-*v* curves shown in Fig. 2.8, which also shows the resulting *p*-*v* curves.

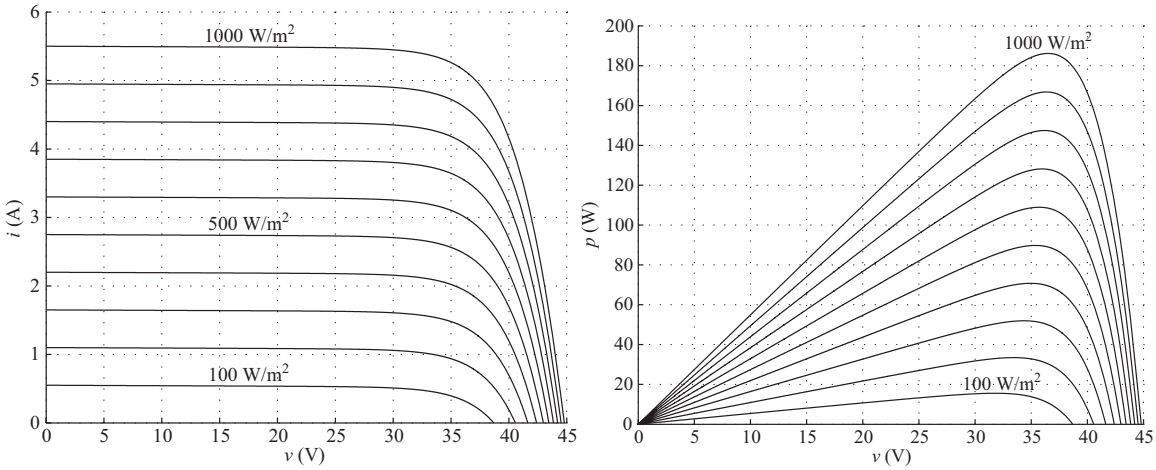


Fig. 2.8 *i*-*v* (left) and *p*-*v* (right) curves under varying insolation

The simulated MPP, V_{mpp}, and I_{mpp} at the different insolation levels are given in Table 2.1. It is important to note that, at 1000 W/m^2, V_{mpp} and I_{mpp} perfectly match the values given in the datasheet, confirming correct parameter extraction and modeling. At the other insolation levels, due to the lack of information from the datasheet, one can only assume that the model is a good representation of the actual physical module.

Table 2.1 Simulated MPP datapoints vs. insolation levels

Insolation (W/m^2)	**MPP (W)**	**V_{MPP} (V)**	**I_{MPP} (A)**
1000	186.1	36.5	5.1
900	166.8	36.4	4.6
800	147.5	36.2	4.1
700	128.2	36.0	3.6
600	108.9	35.7	3.1
500	89.8	35.4	2.5
400	70.8	34.9	2.0
300	51.9	34.4	1.5
200	33.5	33.4	1.0
100	15.6	31.8	0.5

2.3 MPPT Algorithm

For the PV module model to be used efficiently as the energy source of some power electronic circuit, it is necessary for the control of the circuit to incorporate a maximum power point tracking (MPPT) algorithm. Here and in the remainder of this dissertation,

an improved and optimized Perturb and Observe (P&O) MPPT algorithm, introduced in [38, 39] and named *dP*-P&O, will be used in the control of the microinverter input stage.

To better understand the *dP*-P&O algorithm, it useful to start by reviewing the operation of the basic P&O method. P&O is one of the most common MPPT algorithms that have been reported in the literature, although numerous distinct MPPT algorithms have been reviewed and compared in [18]. P&O is widely used because of its simple implementation and relatively low computational load in a microcontroller (μC), microprocessor, or digital signal processor (DSP).

P&O makes use of the fact that the slope of PV module power p with respect to its voltage v is zero at the MPP, positive when v is less than V_{mpp}, and negative when v is greater than V_{mpp}, as shown in Fig. 2.9. Since $dp/dv \cong \Delta P/\Delta V$,

$$\begin{cases} \Delta P/\Delta V = 0, \; v = V_{mpp} \\ \Delta P/\Delta V > 0, \; v < V_{mpp} \\ \Delta P/\Delta V < 0, \; v > V_{mpp} \end{cases}. \tag{2.38}$$

Therefore, the sign of $\Delta P/\Delta V$ can indicate the location of operation on the PV module characteristic curve and in which direction v has to be perturbed to reach the MPP. This can be done based on the flowchart shown in Fig. 2.10, where k represents the k-th instance at which the MPPT command *cmd* is updated to perturb v.

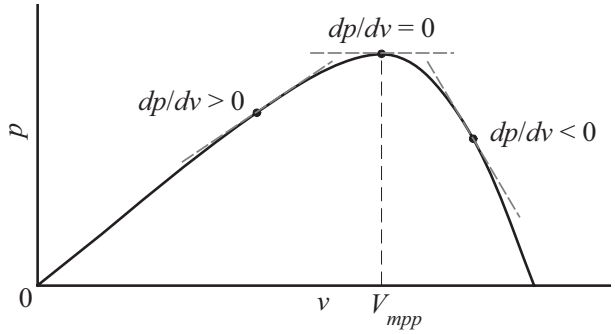


Fig. 2.9 Slopes of PV module characteristic curve

The *cmd* signal can be either a direct voltage command, in which case the perturbation step δ is positive, or a current command with δ being negative since i is negatively correlated to v. For a PV module connected to a power electronic converter, depending on the effect of the duty ratio of the switching device(s) on the PV module

voltage and current, a duty ratio command can also be outputted with the appropriate polarity for δ. For example, in a boost converter, increasing the duty ratio increases the input current. Therefore, a duty ratio command will require the same polarity for δ as a current command.

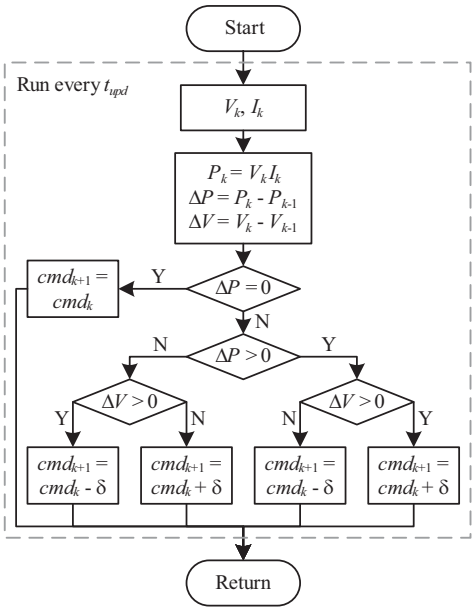


Fig. 2.10 Flowchart for basic P&O MPPT algorithm

Due to noise, ripple, and disturbances in the system, instead of using single samples between updates, it is customary to use a set of samples to compute current and voltage averages, based on which computations and decisions in the flowchart in Fig. 2.10 are made. The magnitude of δ and the update period t_{upd} have to be chosen in such a way as to prevent excessive oscillation about the MPP and to ensure rapid tracking of the MPP.

One drawback of P&O is that tracking tends to diverge from the MPP under rapid changes in insolation. Referring to Fig. 2.11, if the atmospheric conditions remain practically constant from the k-th to (k+1)-th instance, then the PV module characteristic curve does not change and the operating point will move from P_k to P'_{k+1}. This corresponds to a decrease in power (a negative ΔP) and a positive ΔV. Based on Fig. 2.10, the command will be subsequently decremented by δ to bring the operation closer to the MPP. However, if the insolation increases between the k-th and (k+1)-th instances, operation will move from P_k to P_{k+1}, representing a positive ΔP. Consequently, the command will be incremented in the (k+2)-th instance and the operating point will diverge from the MPP and will keep diverging if there is a steady increase in insolation.

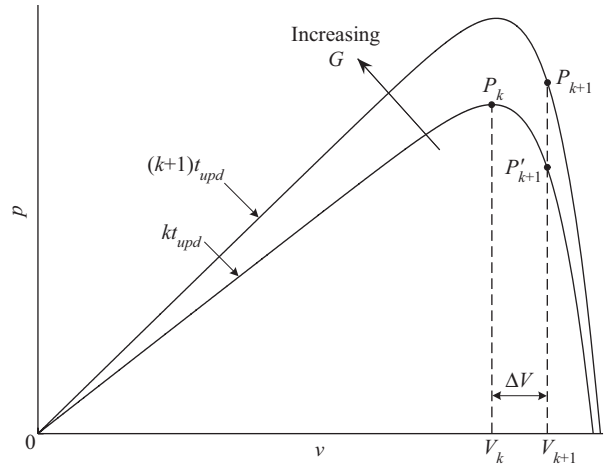


Fig. 2.11 Divergence of P&O under rapid insolation change

The *dP*-P&O MPPT algorithm resolves the shortcoming of the basic P&O by decoupling the change in power due to the MPPT perturbation from the change in power due to the change in insolation [38, 39]. This is done by performing an additional power measurement half-way between two command updates, as shown by P_x in Fig. 2.12. In [38, 39], the difference between P_x and P_k is defined as dP_1, while the difference between P_{k+1} and P_x is dP_2. Assuming that the insolation increases steadily from the k-th to (k+1)-th update, dP_2 represents the change in power due to insolation change since there is no change in MPPT command. On the other hand, the power change dP_1 is due to both MPPT perturbation and insolation change. Therefore, the change in power dP solely due to MPPT perturbation is obtained by

$$dP = dP_1 - dP_2 = \left(P_x - P_k\right) - \left(P_{k+1} - P_x\right) = 2P_x - P_{k+1} - P_k \,. \tag{2.39}$$

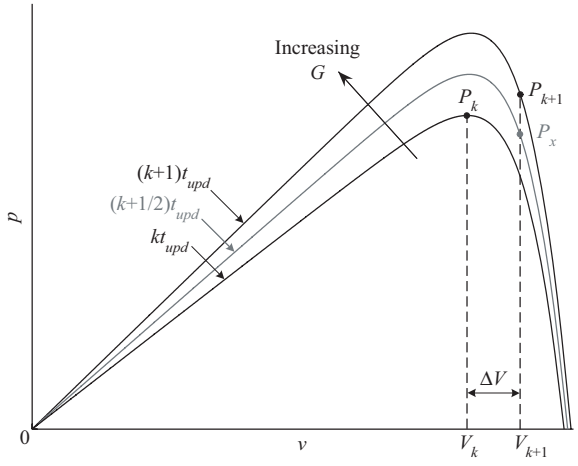


Fig. 2.12 *dP*-P&O additional power measurement between two updates

As long as the magnitude of dP_1 is less than that of dP_2, which is usually the case for steadily changing insolation, dP will capture the true effect of the MPPT perturbation. The dP-P&O can thus be implemented by substituting ΔP in Fig. 2.10 by dP as computed in (2.39), resulting in Fig. 2.13. Note that, even if part of the flowchart runs at half the update time t_{upd} to compute dP, when compared to the basic P&O, no hardware change is required and the computational load hardly increases as no additional sampling is required since the sampling frequency is usually much higher than the update frequency.

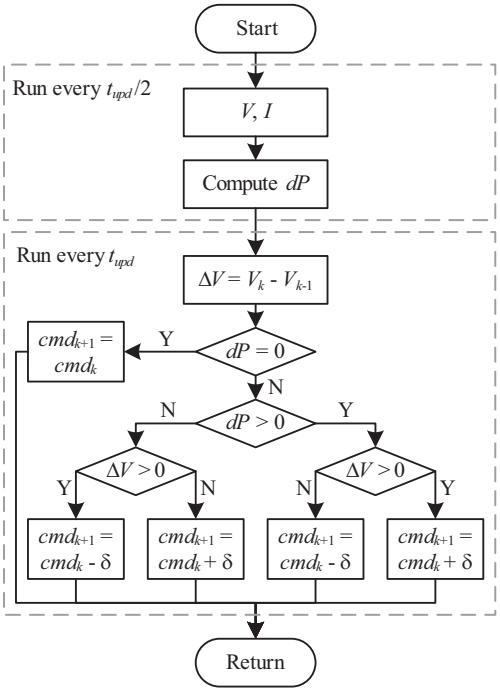


Fig. 2.13 Flowchart for dP-P&O MPPT algorithm

In Dymola, a block was created to implement the dP-P&O MPPT algorithm. The block is shown in Fig. 2.14. The Modelica code within the block can be found in Appendix A. Note that the code also includes the optimization discussed in [39] that, based on the magnitudes of dP_1 and dP_2, allows for bigger perturbation step and faster tracking during rapid changes in insolation. This code can be easily adapted for the firmware of an actual power electronic converter. The block is designed to take the PV module current i and voltage v as inputs. The structure of the code allows the output of the block to either be a voltage, current, or duty ratio command, as discussed above. For the block to output a duty ratio command, the sign of δ has to be chosen according to the power electronic converter to which the PV module is connected.

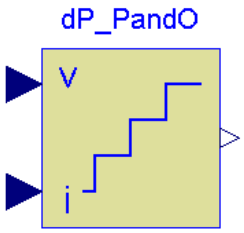


Fig. 2.14 Dymola *dP*-P&O MPPT block

2.4 Boost Converter Setup for MPPT Analysis

With the PV module model and MPPT blocks complete, the performance of the *dP*-P&O MPPT algorithm can be analyzed using the boost converter setup shown in Fig. 2.15. A boost converter is chosen here because it is arguably the simplest power electronic converter topology that draws continuous current from its energy source—a desirable feature for a PV module. Furthermore, it can be easily modeled, quickly simulated, and substituted by the isolated boost converter of the microinverter input stage. The use of a boost converter instead of a more intricate converter, such as a current-sourced push-pull converter or a single-ended primary inductor converter (SEPIC), among others, does not affect the MPPT algorithm performance analysis herein.

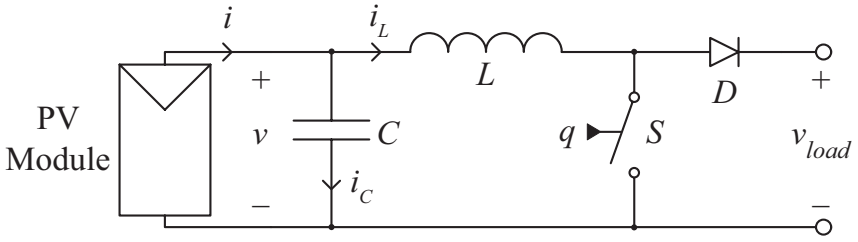


Fig. 2.15 Boost converter connected to PV module

With this boost converter setup, the MPP can be tracked by adjusting the average of the current i_L through the duty ratio d of the switching signal q of the switch S. As per Kirchoff's current law, since the current i_C through the capacitor C is zero on average, controlling the average of i_L effectively controls the average of i.

Hereinafter, 100 kHz will be used for the switching frequency of S, 3.3 µF for C, 100 µH for L, and a nominal voltage of 60 V for the load. The MPPT block will sample the PV module voltage v and current i at a frequency of 15 kHz and will update its output after every 250 samples, corresponding to a 60-Hz update rate (i.e. t_{upd} = 1/60 s). While these parameters affect the convergence speed of the MPPT algorithm, they do not affect the ability of the MPPT algorithm to track the MPP.

2.4.1 *MPPT with Duty Ratio Command*

One of the simplest ways to generate the pulse-width modulation (PWM) switching signal q of the switch S in Fig. 2.15 is to have the MPPT block output a duty ratio command d, as shown in Fig. 2.16. The PWM block can be implemented either in hardware by comparing d to a ramp or triangle carrier signal, or in software by using d as the modulation index for one of the PWM channels that are usually available in digital signal processors.

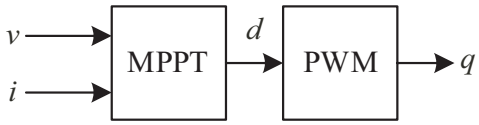


Fig. 2.16 Switching signal generation from MPPT duty ratio command

Figure 2.17 shows the Dymola setup that combines the PV module model, the *dP*-P&O MPPT block, and the boost converter. Ideal current and voltage sensor blocks, available from the Modelica library in Dymola, are used to sense the PV module current i and voltage v. The PWM block simply compares d to a *ramp* signal, which ramps up from 0 to 1 at the switching frequency, such that

$$q = d > ramp\,. \tag{2.40}$$

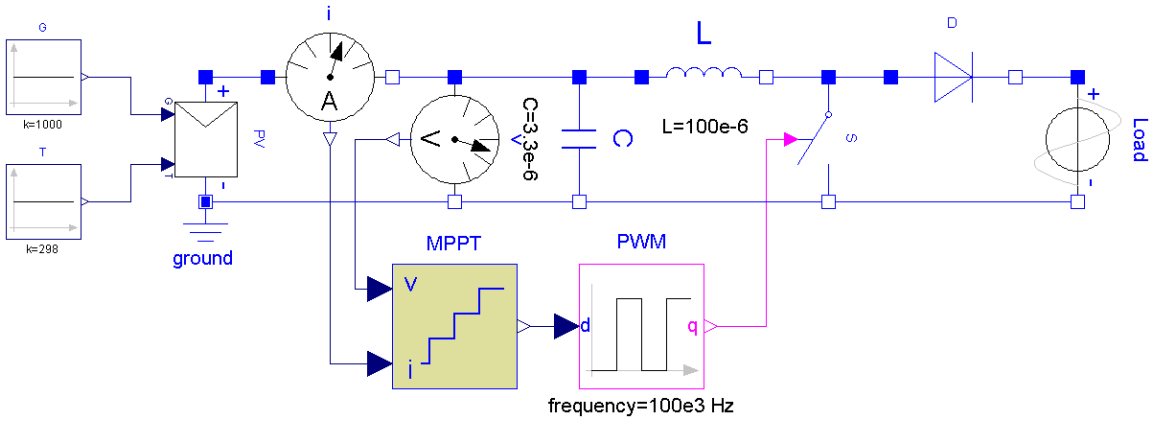


Fig. 2.17 Dymola setup to simulate MPPT with duty ratio command

With the insolation G set to 1000 W/m^2 (full sun), the temperature T to 298 K (25 °C), and the load to 60 V dc, the simulation is run until steady state is reached. Figure 2.18 shows the resulting duty ratio command d, the PV module current i, and power p. Clearly, i has an average of 5.1 A, which matches I_{mpp} (see Table 2.1). It is worth noting that the average of d, denoted by D_0, is also as expected based on the ideal boost converter equation that relates average duty ratio to input and load voltage as follows:

$$D_0 = 1 - \left(V_{mpp} / V_{load} \right) = 1 - \left(36.5/60 \right) = 0.392 . \tag{2.41}$$

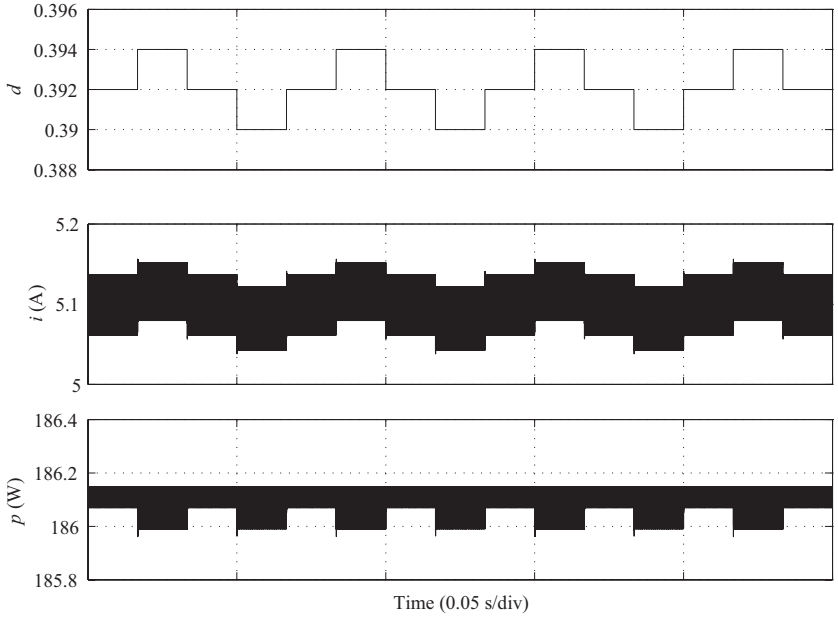


Fig. 2.18 Steady-state waveforms for MPPT with duty-ratio command

However, the above control scheme cannot mitigate every load disturbance because, at a 60-Hz update rate, the MPPT algorithm lacks bandwidth. For example, a 2-V peak-to-peak 120-Hz sinusoidal disturbance added to the 60-V load results in the Fig. 2.19 waveforms, which clearly show 120-Hz ripple on the PV module current and power. This is undesirable because it affects the energy yield of the PV module. Nevertheless, it is interesting to see that the MPPT algorithm is still tracking the MPP.

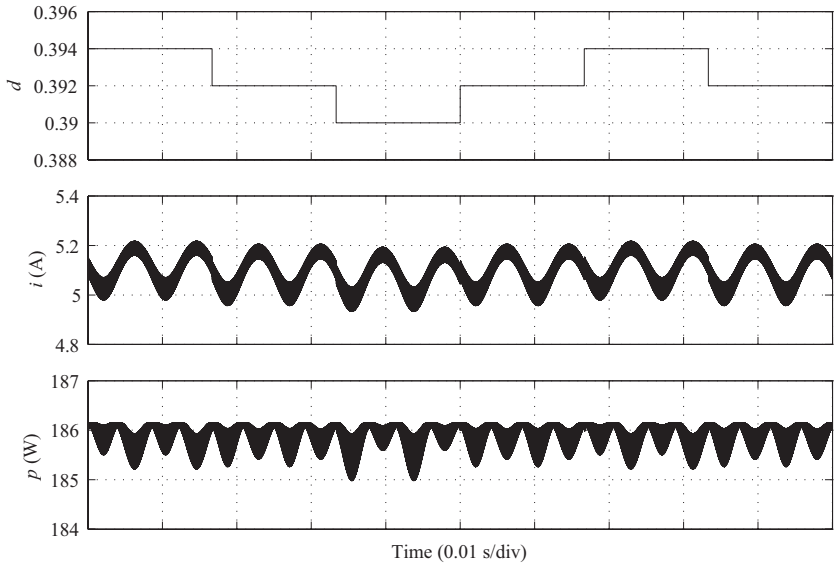


Fig. 2.19 120-Hz load disturbance transmitted to the input

2.4.2 MPPT with Current Command

With an additional control loop, more bandwidth can be obtained to isolate the PV module source from load disturbances. As mentioned previously, the MPPT blocks are also able to output a current command i^*. It is then desired to control q such that i tracks i^*. One way is to use average current mode (ACM) control [40] with i and i^* as inputs to generate the duty ratio d, from which q can be obtained as in Section 2.4.1. In principle, the ACM control is a proportional-integral (PI) controller that aims at driving the error between average of i and i^* to zero. Figure 2.20 shows the implementation of this control scheme.

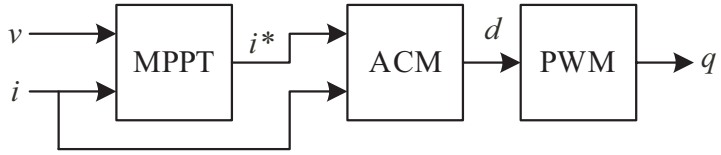


Fig. 2.20 Switching signal generation from MPPT current command

The proportional gain k_{p_acm} and integral gain k_{i_acm} of the ACM control have to be chosen accordingly to ensure adequate bandwidth for i to track i^* and stability of the closed loop. The i^* to i transfer function, derived in Appendix B, is given by

$$\frac{i(s)}{i^*(s)} = \frac{V_{load0}k_{p_acm}s + V_{load0}k_{i_acm}}{Ls^2 + V_{load0}k_{p_acm}s + V_{load0}k_{i_acm}}, \tag{2.42}$$

where V_{load0} represents the nominal load voltage. Figure 2.21 shows a plot of the magnitude of (2.42) as a function of frequency, with V_{load0} = 60 V, k_{p_acm} = 0.3 V/A, and k_{i_acm} = 10 kV/As. The close-loop system has a bandwidth of 34 kHz, which is slightly aggressive with a 100-kHz switching frequency, but is needed to attenuate any load disturbance at the input of the boost converter, as will be shown shortly.

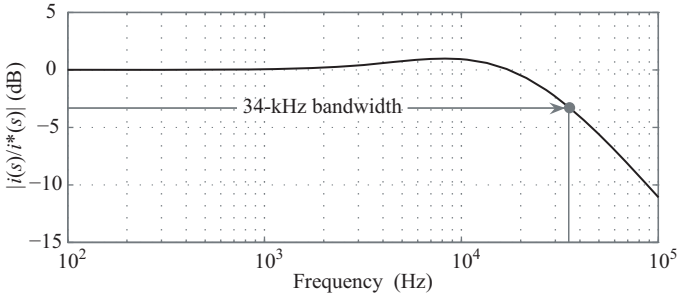


Fig. 2.21 Bandwidth of the input current control loop

Also derived in Appendix B, the loop gain of the $i(s)/i^*(s)$ can be expressed as

$$\ell_i(s) = \frac{V_{load0} k_{p_acm} s + V_{load0} k_{i_acm}}{Ls^2}. \tag{2.43}$$

The Bode plot of $\ell_i(s)$, shown in Fig. 2.22, confirms the stability of the closed loop with a phase margin of 80°.

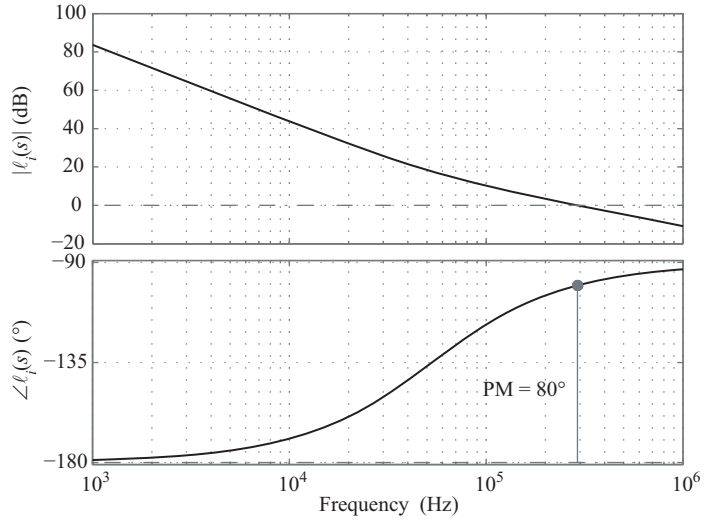


Fig. 2.22 Bode plot of input current control loop

Moreover, the attenuation of load disturbances at the input of the boost converter can be analyzed by plotting the magnitude of the $i(s)/v_{load}(s)$ transfer function, which is given by (see Appendix B for derivation)

$$\frac{i(s)}{v_{load}(s)} = \frac{(D_0 - 1)s}{Ls^2 + V_{load0} k_{p_acm} s + V_{load0} k_{i_acm}}. \tag{2.44}$$

With D_0 as given in (2.41), Fig. 2.23 shows the magnitude plot of (2.44).

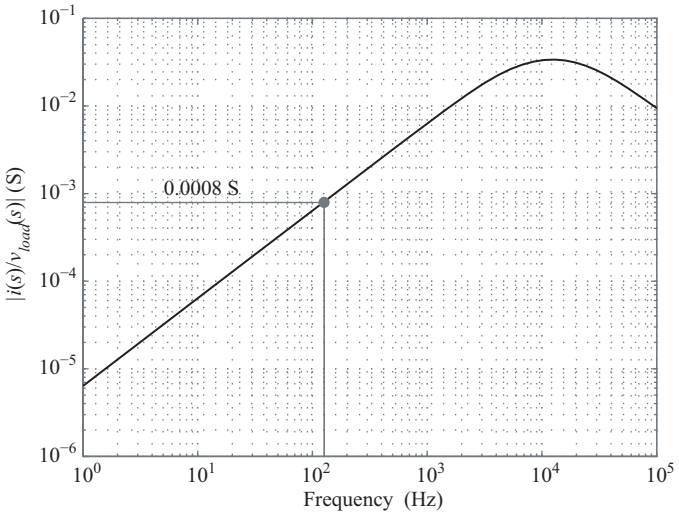


Fig. 2.23 Input transconductance

As pointed out in Fig. 2.23, the input transconductance at 120 Hz is about 0.8 mS. Therefore, a 2-V peak-to-peak 120-Hz load disturbance will be well attenuated and the 120-Hz ripple in i will be minimal. More attenuation can be achieved by increasing the gains of the ACM control. However, increasing the gains also increases the bandwidth, which was already aggressive with k_{p_acm} = 0.3 V/A, and k_{i_acm} = 10 kV/As. On the other hand, decreasing these gains leads to a less aggressive bandwidth, but at the expense of less attenuation of load disturbances at the input.

Therefore, with k_{p_acm} = 0.3 V/A and k_{i_acm} = 10 kV/As proven to provide ample bandwidth, stability, and enough attenuation, the control scheme in Fig. 2.20 is incorporated with the boost converter in Dymola as in Fig. 2.24.

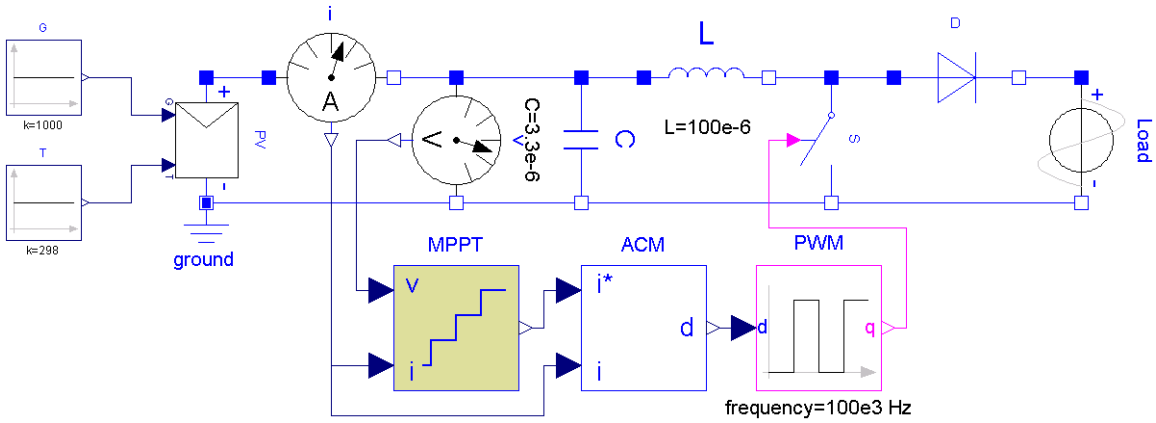


Fig. 2.24 Dymola setup to simulate MPPT with current command

The simulation is run with the same settings as in Section 2.4.1, along with the 2-V peak-to-peak 120-Hz sinusoidal load disturbance. From the steady-state waveforms shown in Fig. 2.25, it can be seen that most of the 120-Hz ripple has been attenuated at the input, as expected by the above derivations. Although this control scheme using MPPT current command can mitigate load disturbances, the PV power p collapses under rapid decrease in insolation as shown in Fig. 2.26. This is because, under rapid decrease in insolation, it is very likely that i* from the k-th update does not lie on the PV module characteristic curve at the (k+1)-th update. In such a case, in practice, the boost converter will shut down completely and go through its startup routine all over again. Of course, this can lead to considerable waste of available PV power.

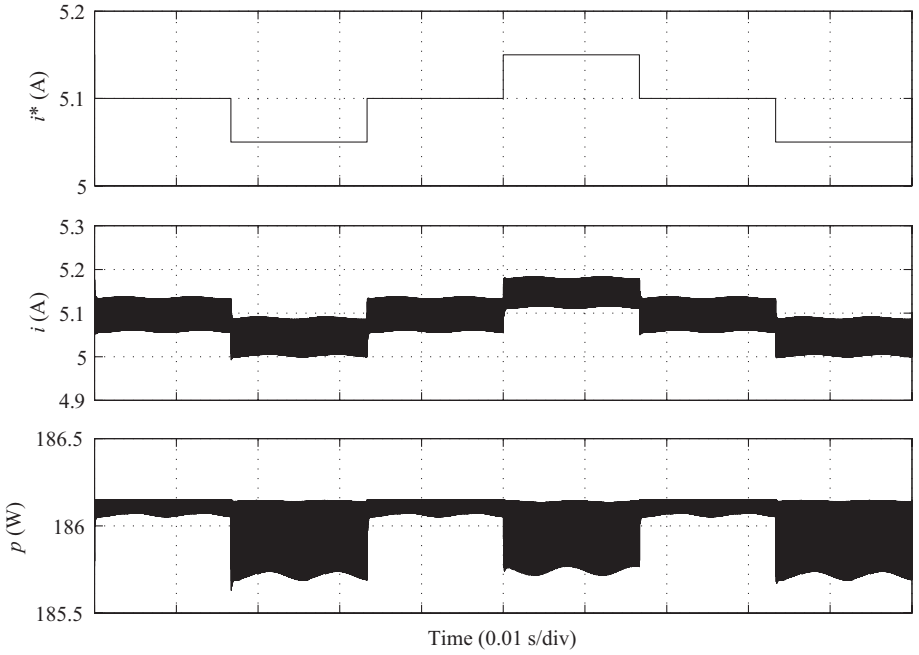


Fig. 2.25 Steady-state waveforms for MPPT with current command

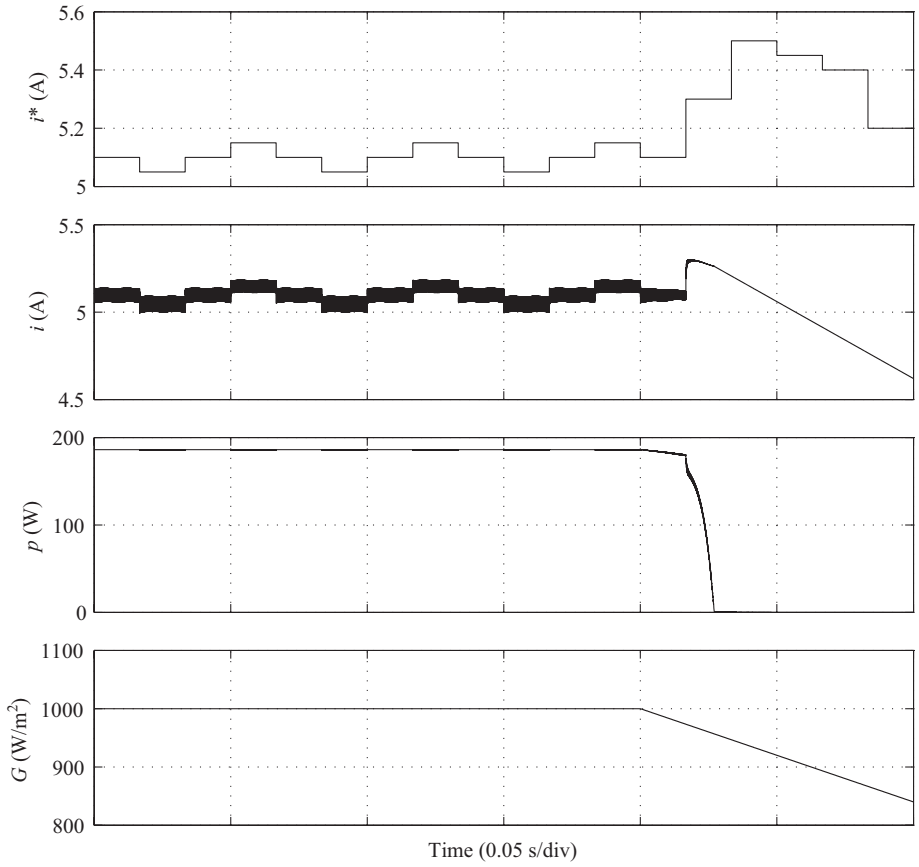


Fig. 2.26 Power collapse with MPPT current command under rapid decrease in insolation

2.4.3 MPPT with Voltage Command

Under rapidly decreasing insolation, thanks to the slow variation of the PV module voltage v with insolation, having the MPPT block output a voltage command v^* alleviates the lack of robustness of the control method in Section 2.4.2. The switching signal q being the only control handle, it has to be obtained from v^*. One way is to use a proportional-integral (PI) control on v^* and v to obtain the duty ratio d. Then q is generated from d just like in Section 2.4.1. Figure 2.27 shows this implementation, which only performs well in the absence of load disturbances.

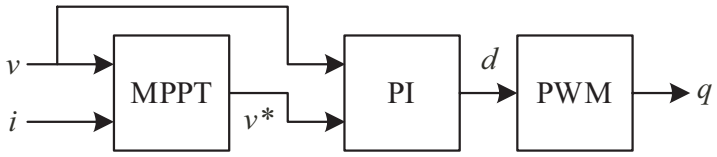


Fig. 2.27 Switching signal generation from MPPT voltage command

To be more robust to load disturbances, the PI control can generate a current command. Similar to the implementation in Section 2.4.2, ACM is then used to generate the duty ratio command d, from which q can be obtained, as illustrated in Fig. 2.28 and implemented in Dymola in Fig. 2.29.

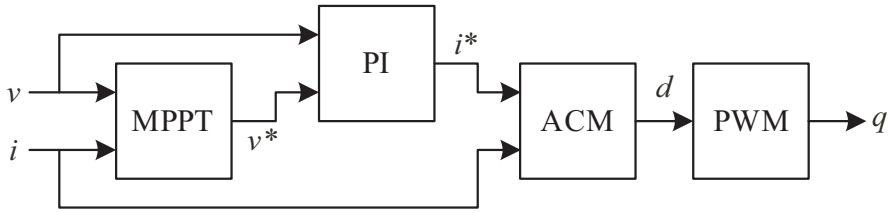


Fig. 2.28 Alternative switching signal generation from MPPT voltage command

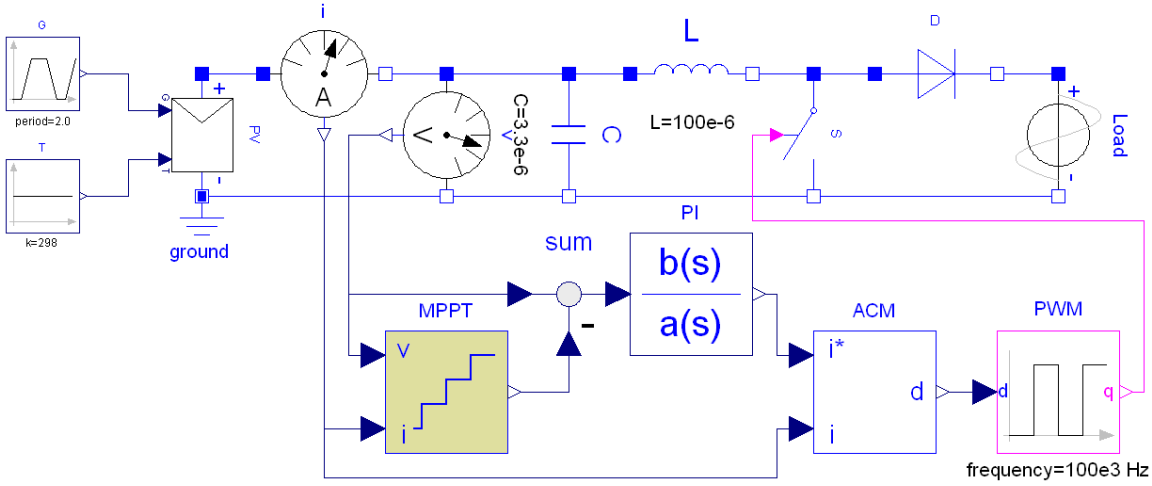


Fig. 2.29 Dymola setup to simulate MPPT with voltage command

To show the robustness of the control scheme in Fig. 2.28, the insolation G is made to remain at 1000 W/m^2 for 0.5 s before decreasing steadily over 0.5 s to 200 W/m^2. G is maintained at this insolation level for another 0.5 s before getting back to 1000 W/m^2 after 0.5 s. The 2-V, 120-Hz sinusoidal load disturbance is also included. The MPPT voltage command v*, the PV module current i, power p, and G are shown in Fig. 2.30.

It is worth noting that the MPPT performs perfectly with v* tracking V_{mpp} during the steady states at 1000 and 200 W/m^2 (see Table 2.1). Furthermore, 120-Hz ripple is not discernible on the input and the input power does not collapse under rapidly changing insolation. A close look at the v* waveform also reveals the increase in perturbation step size during the insolation transients, thanks to the optimization of the *dP*-P&O MPPT algorithm.

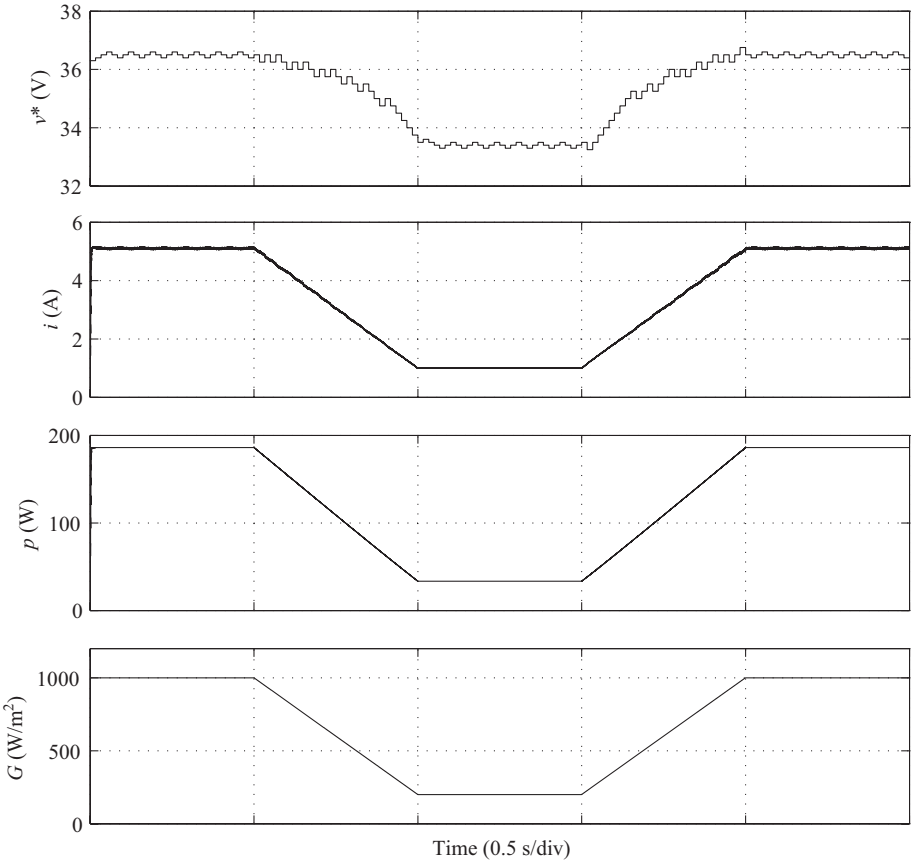


Fig. 2.30 Robustness of control scheme using MPPT with voltage command under varying insolation

2.5 Isolated Boost Converter

As mentioned above, the conventional boost converter used in the previous sections can be substituted by the isolated boost converter shown in Fig. 2.1. The switching

signals of the MOSFETs of the full-bridge inverter can be obtained from the switching signal q of the boost converter as

$$\begin{aligned} q_{i11} &= q_{i22} = q + Q \\ q_{i12} &= q_{i21} = q + \overline{Q}, \end{aligned} \tag{2.45}$$

where Q is a square pulse waveform synchronized with the *ramp* signal, but at half the frequency, as illustrated in Fig. 2.31. As can be seen from the same figure, while q is at 100 kHz, the resulting switching signals for the input full-bridge inverter are only at 50 kHz. However, the frequency of the switching ripples on the inductor current i_L and the PV module current i remain at 100 kHz.

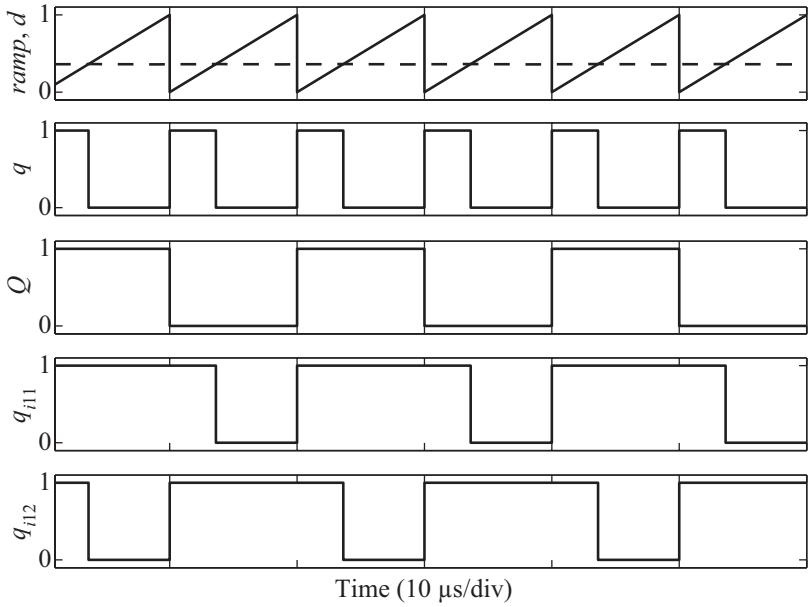


Fig. 2.31 Switching signals for input full-bridge inverter

The input stage, as shown in Fig. 2.1, was thus put together in Dymola with its switching signals generated as per (2.45) and the duty ratio d generated using the Fig. 2.28 implementation. Figure 2.32 shows the Dymola setup. In this case, the voltage source used for the load represents the bus voltage v_{bus} and is nominally set to 400 V. The turns ratio of the transformer is set to 1:7 such that the resulting duty ratio is about the same as the conventional boost converter in steady state. Disable ports are included in the input switching and the PI blocks to be able to stop the input stage from processing power and to prevent the integral loop from winding up, respectively, when a fault is detected from the output stage. Simulating this setup results in the same waveforms as in Fig. 2.30.

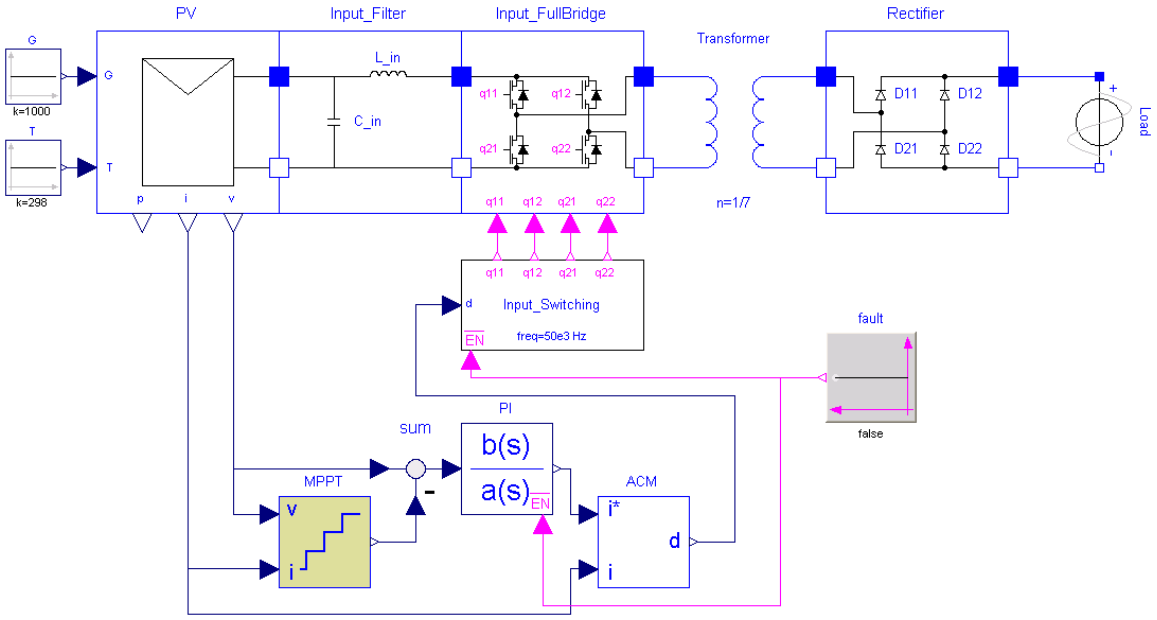


Fig. 2.32 Dymola microinverter input stage setup

2.6 Average-Value Model

From all the above simulation results, it can be noticed that, due to the ACM control, the average of PV current i is practically equal to i^*. Based on this observation, the fast switching of the system can be neglected, without the loss of essential dynamics, and an average-value model (AVM) can be created for the isolated boost converter in Dymola, as shown in Fig. 2.33. This AVM is also valid for the conventional boost converter. The average input current of either converter can be modeled as a controlled current source equal to the current command i^*. With the assumption that the converter is ideal (that is, no power loss), the controlled current source for the output current is dictated by

$$i_{out} = \frac{v_{in} i_{in}}{v_{out}} = \frac{v_{in} i^*}{v_{out}}. \tag{2.46}$$

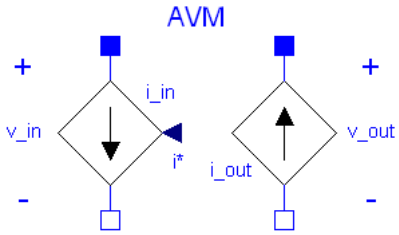


Fig. 2.33 Dymola average-value model for input converter

In Dymola, the switch-level isolated boost converter, with the input filter, in Fig. 2.32 is replaced by the AVM block. The ACM and switching blocks are removed to directly

use the current command i^*. The resulting setup in Fig. 2.34 is simulated using the same insolation setting as in Section 2.4.3 to generate the waveforms in Fig. 2.35. Perfect match can be noted between these waveforms and those shown in Fig. 2.30, except from the ripple in the power p and the fact that $i = i^*$. More importantly, the simulation time for the setup in Fig. 2.34 is a lot faster than that for the setup in Fig. 2.29—the CPU integration times reported by Dymola are 18.5 s and 710 s, respectively.

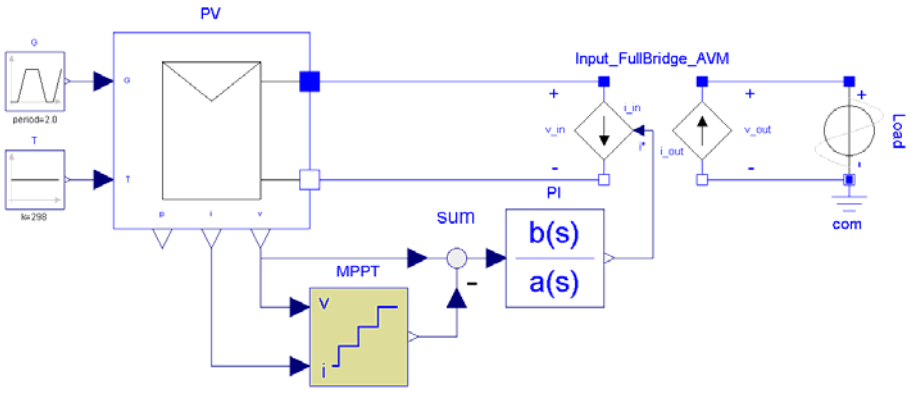


Fig. 2.34 Dymola setup with boost converter average-value model

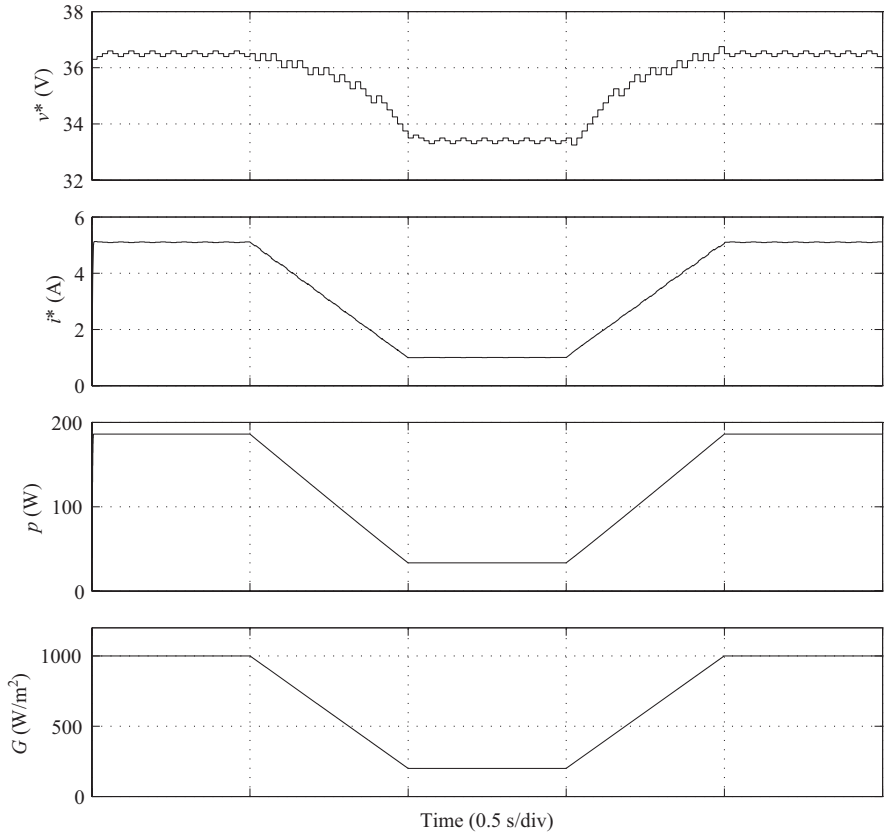


Fig. 2.35 Waveforms from boost converter average-value model setup

3 OUTPUT STAGE

3.1 Overview

The output stage of the microinverter, introduced in Section 1.5 and shown below in Fig. 3.1, comprises a full-bridge inverter along with an output filter made up of, but not limited to, an inductor L_{out}. The input side of the output stage is connected to a bus capacitor while the output side generally connects to a feeder line coming from the utility grid. The point at which the output stage is connected to the feeder line is called the point of common coupling (PCC).

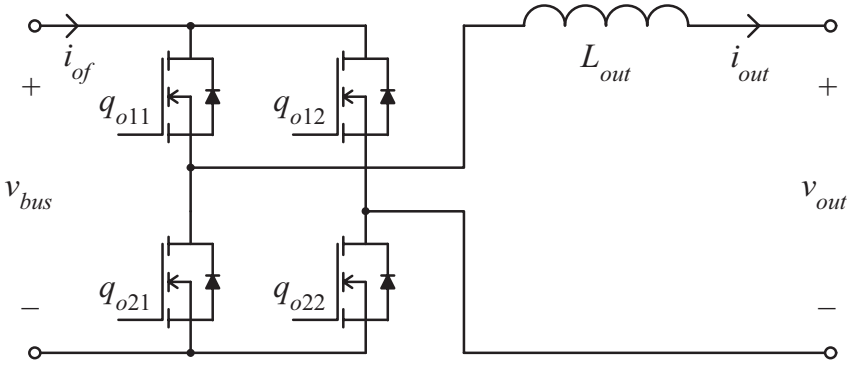


Fig. 3.1 Microinverter output stage

A one-line diagram of a common interconnection layout for a grid-tied photovoltaic (PV) system (combination of the PV module/array and microinverter/inverter) is illustrated in Fig. 3.2 [41]. The feeder line is connected to the utility grid through a transformer and a switch (breaker, recloser, etc.). A parallel resistor-inductor-capacitor (RLC) load, which can represent a wide range of electrical loads, may also be connected locally at the same PCC.

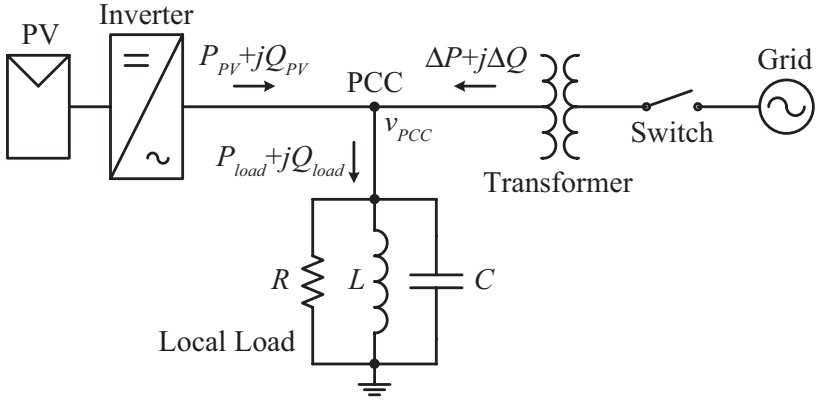


Fig. 3.2 Common grid-tied PV system interconnection as shown in [41]

In Fig. 3.2,

- P_{PV} = real power from the PV system,
- Q_{PV} = reactive power from the PV system,
- P_{load} = real power into the local RLC load,
- Q_{load} = reactive power into the local RLC load,
- ΔP = real power from the utility grid,
- ΔQ = reactive power from the utility grid, and
- v_{PCC} = voltage at PCC.

As stated in the IEEE 1547 standard [42], "utility electric power systems were not designed to accommodate active generation and storage at the distribution level." Consequently, IEEE 1547 sets forth several requirements that have to be met when distributed resources—which include PV systems—are connected to the utility grid. These requirements ensure that distributed resources respond appropriately to abnormal grid conditions and islanding and maintain the grid power quality.

While it is fairly straightforward to have the control system of the microinverter output stage detect and respond to abnormal grid voltages and frequencies, as will be shown in Sections 3.2 and 3.3, respectively, and to have the output current i_{out} meet the harmonic limits discussed in Section 3.4, Section 3.5 will show that detecting islanding conditions may sometimes be challenging in the presence of local resonant RLC loads. For this reason, over the past decades, a number of islanding detection methods (IDMs) have been developed, tested, and refined.

Three IDMs [41, 43-47]—active frequency drift (AFD), slip mode frequency shift (SMS), and Sandia frequency shift (SFS, also known as the active frequency drift with positive feedback AFDPF)—will be reviewed and analyzed hereinafter. It will be shown that these IDMs have nondetection zones (NDZs)—sets of local resonant RLC loads for which the IDMs are unable to detect the formation of an island. The theoretical NDZs will be derived for each method and confirmed through the simulation results of a switch-level full-bridge inverter model. The latter part of this chapter will show that the detailed inverter model can be replaced by an average-value model (AVM) and still capture the behaviors and performances of the IDMs. It is worth noting that the detection techniques covered here apply worldwide, even though different countries have different standards.

3.2 Abnormal Voltages

As per IEEE 1547 Clause 4.2.3, if the voltage v_{PCC} at the PCC has a root-mean-square (rms) value V_{PCC} that is within one of the ranges given in Table 3.1, the PV system(s) connected to the PCC shall cease to provide energy to the utility grid within the corresponding clearing time (note that 240 V is used as the base voltage to represent the line-to-line voltage of a typical household split-phase system). Therefore, V_{PCC} needs to be continuously computed within each PV system. This can be realized by sensing and sampling v_{PCC}, which is equivalent to v_{out} in Fig. 3.1, at a frequency f_{sample} and then computing the rms on the last $n_{samples}$ samples (a moving window), where

$$n_{samples} = \frac{f_{sample}}{f_{nom}}. \tag{3.1}$$

Table 3.1 Interconnection system response to abnormal voltages [42]

Voltage Range (% of base voltage)	Clearing Time (s)	Voltage Range (240 V base voltage)
$V_{PCC} < 50\%$	0.16	$V_{PCC} < 120$ V
$50\% \leq V_{PCC} < 88\%$	2.00	120 V $\leq V_{PCC} < 211.2$ V
$110\% < V_{PCC} < 120\%$	1.00	264 V $< V_{PCC} < 288$ V
$V_{PCC} \geq 120\%$	0.16	$V_{PCC} \geq 288$ V

The sampling frequency f_{sample} is usually chosen to be a multiple of the nominal frequency f_{nom} of the frequency f of v_{PCC}. Note that possible errors introduced in the computation of V_{PCC} by variations in f are not substantial because f is usually well regulated and not expected to have a wide variation, as will be seen in Section 3.3. Once V_{PCC} is within an abnormal range, it is usual to let the PV system run for a number of line cycles to verify that the abnormal voltage is sustained and not momentary before shutdown, thus preventing nuisance tripping of the PV system. Figure 3.3 shows a block, created in Dymola [28], that takes in the sensed signal and outputs its rms value. The code within the block, written in Modelica modeling language, is given in Appendix A.

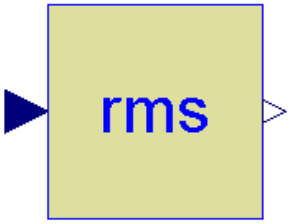


Fig. 3.3 Dymola root-mean-square (rms) computation block

3.3 Abnormal Frequencies

IEEE 1547 Clause 4.2.4 states that if the frequency f of v_{PCC} is within one of the ranges given in Table 3.2, the PV system(s) connected to the PCC shall cease to provide energy to the utility grid within the indicated clearing time. One method, which will be used herein to compute f on the fly, is to use the zero crossings of v_{PCC}. Another method is through the oscillator of a phase lock loop (PLL)—since this method is more involved and may have a relatively slower response, it will not be discussed further. As in the abnormal voltages case, to avoid nuisance tripping of the PV systems, it is customary to confirm that the abnormal frequency is sustained over several line cycles, within the allowable clearing time, before shutting down the PV systems. The Dymola block that was created to compute f is shown in Fig. 3.4 while its internal code is provided in Appendix A.

Table 3.2 Interconnection system response to abnormal frequencies [42]

Frequency Range (Hz)	Clearing Time (s)
$f > 60.5$	0.16
$f < 59.3$	0.16

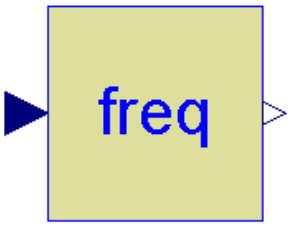


Fig. 3.4 Dymola frequency computation block

3.4 Power Quality

If PV systems inject dc currents into the utility grid, magnetic components such as the cores of distribution transformers might saturate, leading to unwanted power distortions [48]. As a result, IEEE 1547 Clause 4.3.1 requires that a PV system shall not inject dc current greater than 0.5% of its full rated output current at the PCC. Furthermore, IEEE 1547 Clause 4.3.3 states that the harmonic current injection into the utility grid at the PCC shall not exceed the limits given in Table 3.3, with the total harmonic distortion (THD) limit of 5%. Whether a PV system satisfies the dc and harmonic current limits depends on its inverter design and can be checked at the time of design and testing. While

a spectrum analyzer can be used to obtain the frequency content of the PV system output current in hardware, a similar task can be done during the modeling stage by running the simulated output current through a fast Fourier transform (FFT). A MATLAB code to perform the FFT and compute the THD is given in Appendix A and examples of its outcome will be shown in Sections 3.6.1 and 3.6.2.

Table 3.3 Maximum harmonic current distortion in percent of current [42]

Individual harmonic order h (odd harmonics)	**h < 11**	**11 ≤ h < 17**	**17 ≤ h < 23**	**23 ≤ h < 35**	**35 ≤ h**	**Total harmonic distortion**
Percent (%)	4.0	2.0	1.5	0.6	0.3	5.0
Even harmonics are limited to 25% of the odd harmonic limits above.						

3.5 Islanding

An important requirement of IEEE 1547 [42] is the prevention of islanding, which can occur when distributed resources continue to power a section of the utility grid after that section has been disconnected from the utility power source [44, 46, 49]. Since such a case is hazardous to utility personnel and equipment, IEEE 1547 Clause 4.4.1 states that the PV system converter/inverter shall detect that islanding has occurred and cease to energize the disconnected section within two seconds of the formation of the island.

An islanding scenario may be better understood by looking at Fig. 3.2; if the power into the local RLC load perfectly matches the power from the PV system (i.e. $P_{PV} = P_{load}$ and $Q_{PV} = Q_{load}$), then no power will flow from the utility grid (i.e. $\Delta P = 0$ and $\Delta Q = 0$). Therefore, when the switch opens due to a fault on the grid, the PV system will not notice any change or disturbance and will continue providing power to the local load, consequently forming an island. This represents a shock hazard to the utility personnel if the latter were to carry out maintenance on the live side of the switch. This is why the PV system islanding detection method (IDM) shall satisfy the IEEE 1547 Clause 4.4.1.

3.5.1 Local Load

Since the performances of IDMs depend on the local resonant RLC load, it is worthwhile to review the characteristics of such a load. The resonant frequency f_0 of the parallel RLC load is given as

$$f_0 = \frac{1}{2\pi\sqrt{LC}}. \tag{3.2}$$

Its quality factor Q_f, defined as 2π times the maximum energy stored to the energy dissipated per cycle [47], reduces to

$$Q_f = R\sqrt{\frac{C}{L}} = \omega_0 RC = \frac{R}{\omega_0 L}, \text{ where} \tag{3.3}$$

$$\omega_0 = 2\pi f_0. \tag{3.4}$$

For a given Q_f and f_0, R, L, and C can be computed using the following equations [50]:

$$R = \frac{V^2}{P}, \tag{3.5}$$

$$L = \frac{V^2}{2\pi f_0 P Q_f}, \text{ and} \tag{3.6}$$

$$C = \frac{PQ_f}{2\pi f_0 V^2}, \tag{3.7}$$

where P is the rated power of the PV system and V is the nominal operating voltage of the system. For example, for $Q_f = 1.0$, $f_0 = 60$ Hz, $P = 185$ W, and $V = 240$ V, Equations (3.5)–(3.7) result in 311.4 Ω, 0.826 H, and 8.52 μF for R, L, and C, respectively.

The local load impedance Z_{load}, which will be essential in analyzing the different IDMs hereinafter, at an operating frequency f is

$$Z_{load} = \left(\frac{1}{R} + \frac{1}{j\omega L} + j\omega C\right)^{-1} = \frac{1}{\frac{1}{R} - j\left(\frac{1}{\omega L} - \omega C\right)}, \text{ where} \tag{3.8}$$

$$\omega = 2\pi f. \tag{3.9}$$

The magnitude and phase of Z_{load} are

$$\left|Z_{load}\right| = \frac{1}{\sqrt{\frac{1}{R^2} + \left(\frac{1}{\omega L} - \omega C\right)^2}} = \frac{R}{\sqrt{1 + \left[R\left(\frac{1}{\omega L} - \omega C\right)\right]^2}} = \frac{R}{\sqrt{1 + Q_f^2\left(\frac{f_0}{f} - \frac{f}{f_0}\right)^2}}, \text{ and} \tag{3.10}$$

$$\angle Z_{load} = 0 - \left[-\tan^{-1}\left(\frac{\frac{1}{\omega L} - \omega C}{\frac{1}{R}}\right)\right] = \tan^{-1}\left[R\left(\frac{1}{\omega L} - \omega C\right)\right] = \tan^{-1}\left[Q_f\left(\frac{f_0}{f} - \frac{f}{f_0}\right)\right]. \tag{3.11}$$

Equations (3.10) and (3.11) can be used to plot the magnitude and phase of the parallel RLC load given in the above example as a function of frequency f, as shown in Fig. 3.5. As can be seen, the load is net inductive for frequencies below the resonant frequency f_0 (60 Hz), net capacitive above f_0, and purely resistive at f_0.

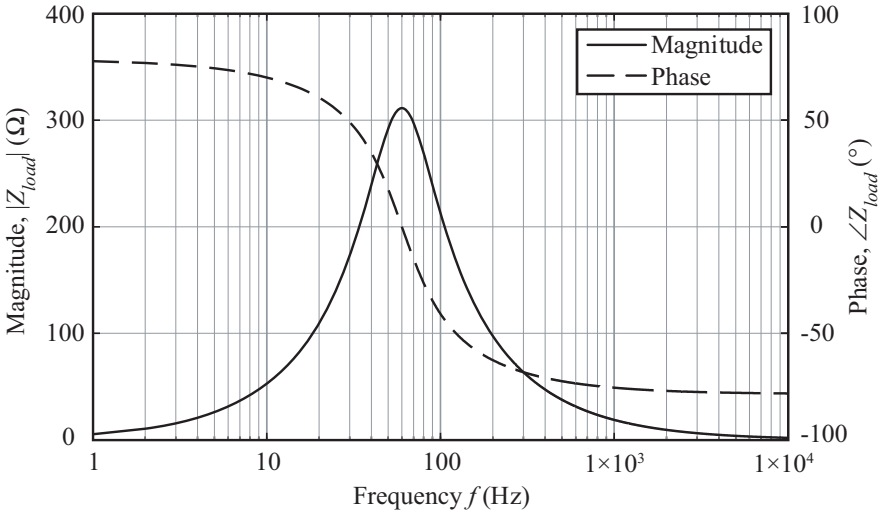


Fig. 3.5 Magnitude and phase of an example parallel RLC load

Taking the phase of the voltage v_{PCC} at the PCC as reference (i.e. $\angle v_{PCC} = 0°$) and the fact the current i_{load} into the local RLC load is given by

$$i_{load} = \frac{v_{PCC}}{Z_{load}}, \tag{3.12}$$

the phase θ_{iload} of i_{load}, as a function of the frequency f, can be expressed as

$$\theta_{iload}(f) = \angle i_{load} = \angle v_{PCC} - \angle Z_{load} = -\tan^{-1}\left[Q_f\left(\frac{f_0}{f} - \frac{f}{f_0}\right)\right]. \tag{3.13}$$

3.5.2 Underfrequency Protection and Overfrequency Protection

As discussed above in Section 3.3, PV systems shall shut down if the frequency f at the PCC is within the abnormal ranges given in Table 3.2. As such, it is mandatory for PV systems to be equipped with underfrequency protection and overfrequency protection, UFP/OFP. These protections can be executed either by using some kind of relay in hardware or in the firmware of the PV system inverter. In either case, the UFP/OFP can prevent islanding under most loads connected in parallel at the PCC [41], as long as the loads do not have resonant frequencies that lie within the normal frequency range. If this

is not the case, when the switch in the system in Fig. 3.2 opens because of a fault or for required servicing, for a PV system inverter operating with current control and unity power factor, the frequency f at the PCC will drift to match the resonant frequency f_0 of the local RLC load and islanding will remain undetected.

It is thus interesting to note that there is a set of RLC loads, with an infinite range of quality factors, that will lead to an islanding frequency f that lies between 59.3 Hz and 60.5 Hz, inclusive. This set of loads can be presented on a Q_f versus f_0 load parameter space [47], as shown by the shaded area in Fig. 3.6. This area is called the nondetection zone (NDZ) of UFP/OFP since islanding cannot be detected for loads within this area. However, there are very few loads in this NDZ that exist in a realistic utility system [41]. Nevertheless, when the anti-islanding capability of a PV system inverter is tested as per the IEEE 1547.1 test standard Clause 5.7.1 [50], a local RLC load having a Q_f of 1.0 ± 0.05 and f_0 within the underfrequency and overfrequency trip limits (see Table 3.2) and as close to the nominal frequency as possible shall be placed in parallel with the inverter. Under such a load, referring to Fig. 3.6, islanding will clearly remain undetected and the PV system will fail the test. Since no action is taken to drive f outside of the normal frequency range, UFP/OFP is considered a passive islanding detection method (IDM).

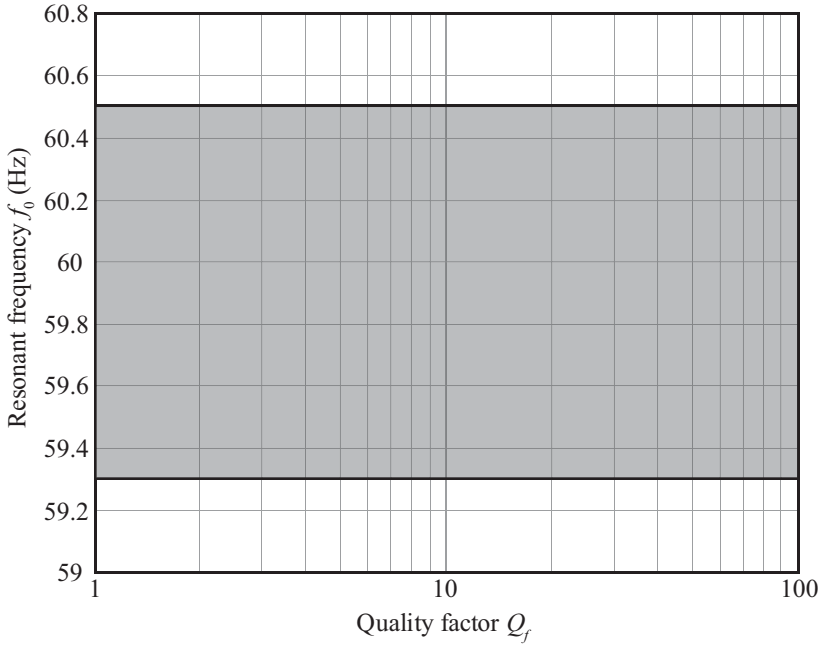


Fig. 3.6 Nondetection zone for UFP/OFP

3.5.3 Active Frequency Drift

The goal of active IDMs is to have the frequency f drift into the abnormal frequency range so that the UFP/OFP, which is a compulsory feature, shut downs the PV system and prevents islanding. The active frequency drift (AFD) IDM [41, 43-45, 47] does so by commanding a slightly distorted current out of the inverter, with its frequency being δf higher than f and with some dead time, as shown in Fig. 3.7. The frequency of the output current in the n^{th} cycle, $f_{i(n)}$, is obtained from f in the previous cycle, $f_{(n\text{-}1)}$, as follows:

$$f_{i(n)} = f_{(n-1)} + \delta f \ . \tag{3.14}$$

The nonzero portion of the output current command for the inverter is then generated as

$$i_{AFD(n)} = \sqrt{2} I \sin\left[2\pi \left(f_{(n-1)} + \delta f \right) t \right], \tag{3.15}$$

where, based on the amount of power P_{out} that needs to be delivered to the utility grid, the root-mean-square (rms) value I is determined as

$$I = \frac{P_{out}}{V_{PCC}} \ . \tag{3.16}$$

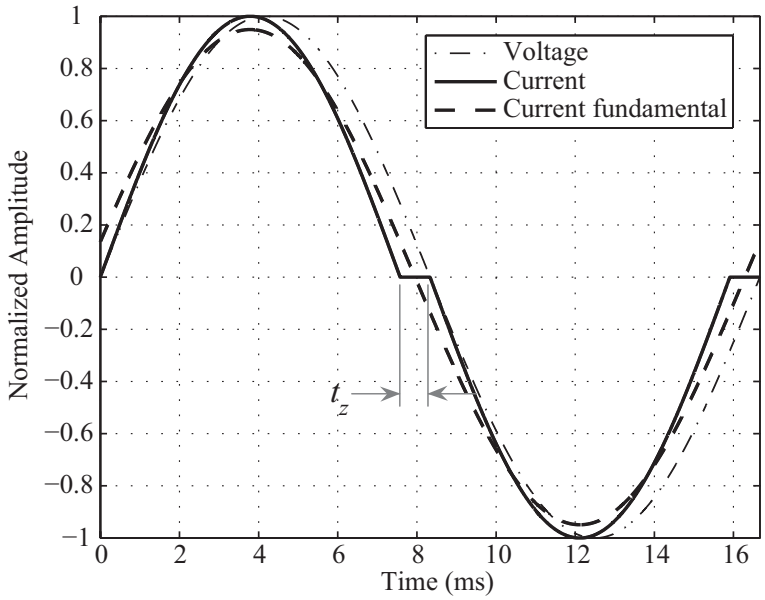


Fig. 3.7 AFD current waveform and its fundamental with respect to voltage waveform

Figure 3.7 also includes the fundamental of the current waveform to show its phase with respect to the voltage. During islanding, v_{PCC} will tend to synchronize with the fundamental of the current, thus leading to a drift in f. As long as the islanding condition persists, the frequency drift will continue, until a steady-state frequency is reached [43].

The theoretical nondetection zone (NDZ) of the AFD IDM can be obtained by deriving an expression relating the steady-state frequency during islanding to the characteristic of the local RLC load. The dead time t_z in Fig. 3.7 is given by

$$t_z = \frac{1}{2}\left(\frac{1}{f} - \frac{1}{f_i}\right) = \frac{1}{2}\left(\frac{1}{f_{(n)}} - \frac{1}{f_{(n-1)} + \delta f}\right). \tag{3.17}$$

With the reasonable assumption that $f_{(n)} \approx f_{(n-1)} = f$,

$$t_z = \frac{1}{2}\left(\frac{1}{f} - \frac{1}{f + \delta f}\right) = \frac{1}{2}\left[\frac{\delta f}{f\left(f + \delta f\right)}\right]. \tag{3.18}$$

It is important to note that the expression for t_z is wrongly derived in [47] leading to NDZs that do not match simulation results. As can be seen in Fig. 3.7, the fundamental of the current leads the voltage by $t_z/2$. Therefore, letting T_v be the period of the voltage, the phase θ_{AFD} of the inverter output current with respect to v_{PCC} can be expressed as

$$\frac{\theta_{AFD}}{2\pi} = \frac{t_z/2}{T_v} = \frac{t_z f}{2} = \frac{f}{4}\left[\frac{\delta f}{f\left(f + \delta f\right)}\right] \Rightarrow \theta_{AFD}\left(f\right) = \frac{\pi \delta f}{2\left(f + \delta f\right)}. \tag{3.19}$$

During islanding, $\theta_{iload}\left(f\right) = \theta_{AFD}\left(f\right)$. Therefore, from (3.13) and (3.19),

$$-\tan^{-1}\left[Q_f\left(\frac{f_0}{f} - \frac{f}{f_0}\right)\right] = \frac{\pi \delta f}{2\left(f + \delta f\right)}. \tag{3.20}$$

The desired expression relating f to the characteristic of the RLC load is obtained by solving (3.20) for f_0, resulting in

$$f_0 = \frac{f}{2Q_f}\left\{\sqrt{4Q_f^2 + \tan^2\left[\frac{\pi \delta f}{2\left(f + \delta f\right)}\right]} - \tan\left[\frac{\pi \delta f}{2\left(f + \delta f\right)}\right]\right\}. \tag{3.21}$$

Using (3.21), for a given Q_f and δf, f_0 can be found for a given frequency f. With f chosen to be the lower and upper trip limit frequencies (59.3 and 60.5 Hz, respectively) and sweeping Q_f for a fixed δf, Fig. 3.8 is obtained.

Figure 3.8 shows the loci of loads, with f_0 and Q_f, that will lead to islanding frequencies equal to the trip frequencies, for different values of δf. For each δf, the loci form an upper and lower boundary and the area enclosed by the boundaries, including the boundaries, represents the NDZ of the AFD IDM. During islanding, any load with f_0 and

Q_f that lies in this area will lead to a frequency f that is within normal frequencies and islanding will therefore remain undetected.

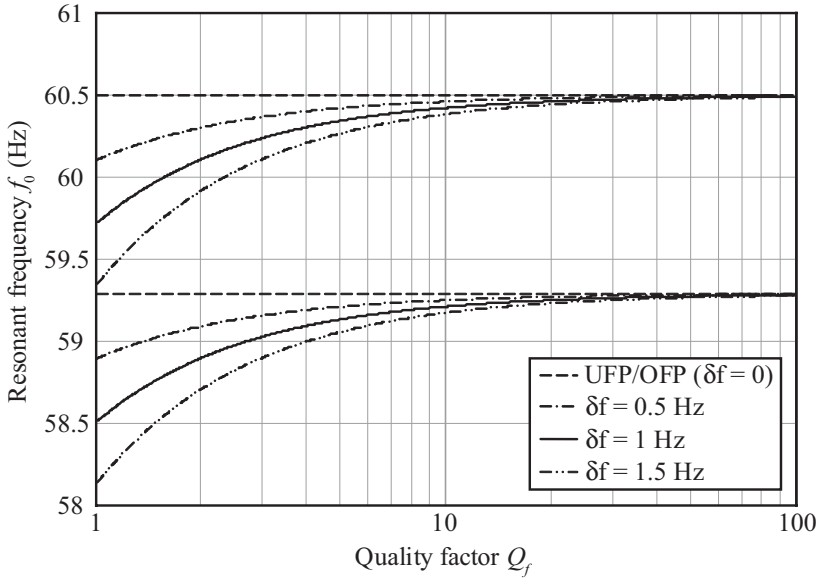


Fig. 3.8 Nondetection zone for AFD

Figure 3.8 also shows that the boundaries for the UFP/OFP NDZ can be obtained by setting δf to zero, which effectively disables the effect of the AFD IDM. In other words, in the absence of an active IDM like AFD, f is simply the resonant frequency f_0 of the local RLC load. In this case, any load with resonant frequency f_0 between 59.3 and 60.5 Hz will lead to undetected islanding conditions. It is also interesting to see that, while AFD helps a PV system inverter pass the IEEE 1547.1 Clause 5.7.1 test requirement with a load having a Q_f of 1.0 ± 0.05 and f_0 within the trip limits, it does not shrink the NDZ, but merely shifts it to a different set of loads.

3.5.4 Slip Mode Frequency Shift

The slip mode frequency shift (SMS) IDM consists in introducing a deviation in the power factor of the PV system to drift the frequency f at the PCC into the abnormal frequency range in the absence of the utility grid. The output current command for the inverter is generated such that

$$i_{SMS(n)} = \sqrt{2} I \sin\left[2\pi f_{(n-1)} t + \theta_{SMS}\right], \text{ where} \tag{3.22}$$

$$\theta_{SMS} = \theta_m \sin\left(\frac{\pi}{2}\frac{f_{(n-1)} - f_g}{f_m - f_g}\right). \tag{3.23}$$

Assuming $f_{(n)} \approx f_{(n-1)} = f$,

$$\theta_{SMS}(f) = \theta_m \sin\left(\frac{\pi}{2}\frac{f - f_g}{f_m - f_g}\right). \tag{3.24}$$

In (3.23) and (3.24), f_g is the grid frequency and f_m is the frequency at which θ_{SMS} is at its maximum deviation θ_m. Frequency f_m is chosen such that, during islanding, the deviation is high enough to bring f within the abnormal range. Reference [47] uses $f_m = f_g + 3$ Hz. When $f = f_g$, θ_{SMS} is zero, but an unstable operating point [41]. Figure 3.9 shows θ_{SMS} for $\theta_m = 5°$ and 10°, with $f_g = 60$ Hz and $f_m = 63$ Hz.

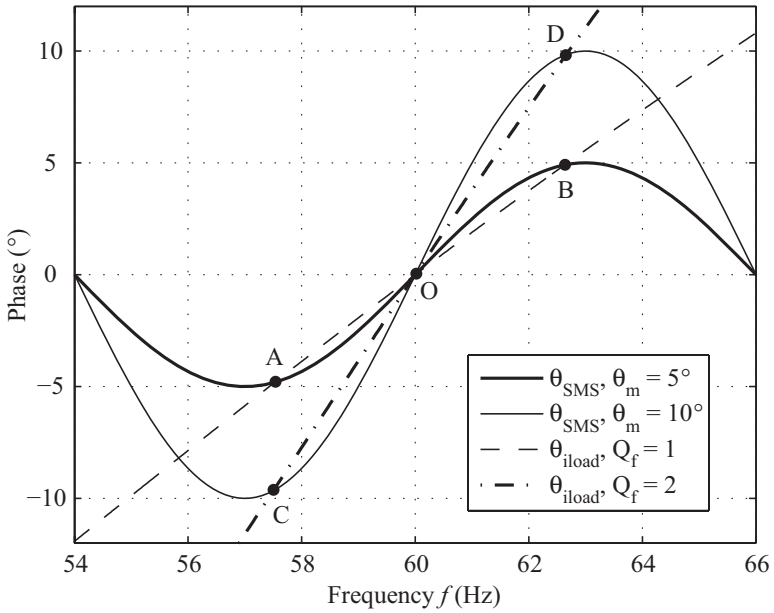


Fig. 3.9 Intersections of load lines and disturbance functions

As long as the grid is present, it acts as a forcing function and maintains an undistorted output current with unity power factor at the nominal frequency of 60 Hz (point *O*). Under islanding conditions, the operating frequency moves to one of the stable points where θ_{iload} intersects θ_{SMS}. For example, an inverter having θ_m set to 5° and connected to a load with $Q_f = 1$ and $f_0 = 60$ Hz will have f shift towards either point *A* or *B*. If the frequency at point *A* or *B* lies outside of the frequency trip limits, islanding will be detected. However, for a load with $Q_f = 2$ and $f_0 = 60$ Hz, the only point of intersection, although unstable, is *O*. As such, the operating frequency remains at 60 Hz and islanding remains undetected. If θ_m is set to 10°, the inverter frequency will then settle to point *C* or *D* under such a load.

Figure 3.9 clearly shows that the SMS IDM has NDZs that depend on θ_m. To find these NDZs, an expression relating the steady-state islanding frequency and the resonant load characteristic has to be derived. During an islanding condition,

$$\theta_{iload}(f) = \theta_{SMS}(f) \Rightarrow -\tan^{-1}\left[Q_f\left(\frac{f_0}{f} - \frac{f}{f_0}\right)\right] = \theta_m \sin\left(\frac{\pi}{2}\frac{f - f_g}{f_m - f_g}\right). \quad (3.25)$$

Solving (3.25) for f_0 leads to the wanted expression:

$$f_0 = \frac{f}{2Q_f}\left\{\sqrt{4Q_f^2 + \tan^2\left[\theta_m \sin\left(\frac{\pi}{2}\frac{f - f_g}{f_m - f_g}\right)\right]} - \tan\left[\theta_m \sin\left(\frac{\pi}{2}\frac{f - f_g}{f_m - f_g}\right)\right]\right\}. \quad (3.26)$$

From (3.26), given Q_f and θ_m, f_0 can be found such that f equals the trip frequency limits. For different values of θ_m, sweeping Q_f leads to loci of f_0 that form upper and lower boundaries as shown in Fig. 3.10. For each θ_m, the upper and lower boundaries (inclusive) enclose the NDZ of the SMS IDM using this specific θ_m.

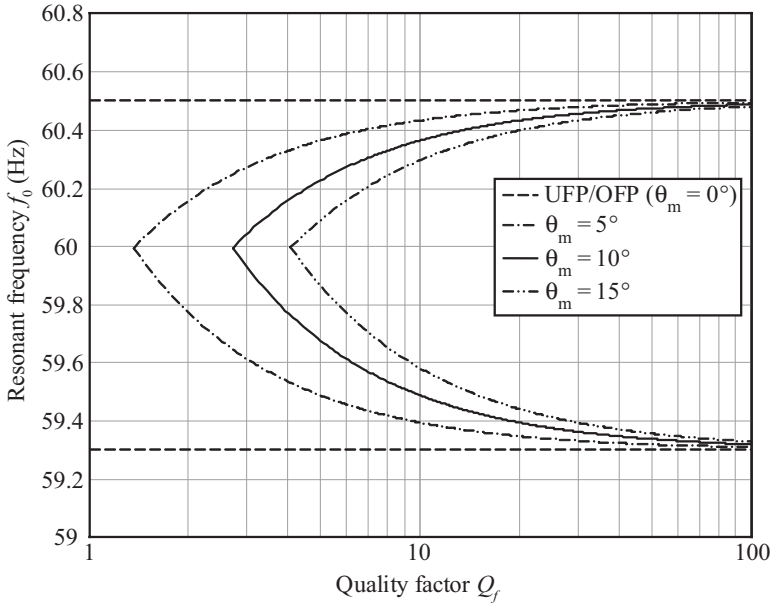


Fig. 3.10 Nondetection zone for SMS

Futhermore, Fig. 3.10 confirms that islanding cannot be detected with a Q_f = 2 and f_0 = 60 Hz load when θ_m = 5º, but this is not the case when θ_m = 10º, as shown in Fig. 3.9 and discussed above. It is also interesting to see that the case with θ_m = 0 corresponds to the UFP/OFP IDM. Unlike the AFD IDM, SMS not only can make an inverter pass the IEEE 1547.1 test, but it also narrows the NDZs—this implies that there are fewer resonant loads for which islanding can remain undetected.

3.5.5 Sandia Frequency Shift

Referring to the current waveform in Fig. 3.7 and with the period of the voltage waveform being T_v, reference [43] defines the chopping fraction *cf* as

$$cf = \frac{2t_z}{T_v}. \tag{3.27}$$

Under islanding conditions, the Sandia frequency shift (SFS) IDM increases *cf* by some kind of positive feedback every line cycle. One way is to scale and add the difference between the frequency *f* at the PCC and the expected nominal grid frequency f_g to the initial *cf*, cf_0 [47]. Therefore, *cf* for the current line cycle can be expressed as

$$cf_{(n)} = cf_0 + k\left(f_{(n-1)} - f_g\right), \tag{3.28}$$

where *k* is the scaling factor (called accelerating gain in [47]). As long as the grid is present, the second term in (3.28) is zero. In terms of δf, $cf_{(n)}$ is given as

$$cf_{(n)} \approx f_{(n)}\left(\frac{1}{f_{(n)}} - \frac{1}{f_{(n-1)} + \delta f}\right). \tag{3.29}$$

Knowing $cf_{(n)}$ and assuming that $f_{(n)} \approx f_{(n-1)}$, δf can be computed as

$$\delta f_{(n)} = f_{(n-1)}\left(\frac{cf_{(n)}}{1 - cf_{(n)}}\right). \tag{3.30}$$

The output current command for the inverter is then generated as

$$i_{SFS(n)} = \sqrt{2}I\sin\left[2\pi\left(f_{(n-1)} + \delta f_{(n)}\right)t\right]. \tag{3.31}$$

In a similar analysis to the AFD IDM,

$$\frac{\theta_{SFS}}{2\pi} = \frac{t_z/2}{T_v} = \frac{cf_{(n)}}{4}. \tag{3.32}$$

Combining (3.28) and (3.32) and assuming $f_{(n)} \approx f_{(n-1)} = f$,

$$\theta_{SFS}(f) = \frac{\pi}{2}\left[cf_0 + k\left(f - f_g\right)\right]. \tag{3.33}$$

During islanding,

$$\theta_{iload}(f) = \theta_{SFS}(f) \Rightarrow -\tan^{-1}\left[Q_f\left(\frac{f_0}{f} - \frac{f}{f_0}\right)\right] = \frac{\pi}{2}\left[cf_0 + k\left(f - f_g\right)\right]. \tag{3.34}$$

Solving (3.34) for f_0 leads to the following equation:

$$f_0 = \frac{f}{2Q_f}\left\{\sqrt{4Q_f^2 + \tan^2\left[\frac{\pi}{2}\left[cf_0 + k\left(f - f_g\right)\right]\right]} - \tan\left[\frac{\pi}{2}\left[cf_0 + k\left(f - f_g\right)\right]\right]\right\}. \quad (3.35)$$

From (3.35), given Q_f and cf_0, f_0 can be found such that f equals the trip frequency limits. With cf_0 fixed at 0.024, corresponding to a δf_0 of 1.5 Hz, for different values of k, sweeping Q_f leads to sets of f_0 that form the upper and lower boundaries as shown in Fig. 3.11. For each k, the upper and lower boundaries (inclusive) enclose the NDZ of the SFS IDM that uses this particular value of k. It is also interesting to see that the case with $k = 0$ and $\delta f_0 = 0$ corresponds to UFP/OFP and that the case with $k = 0$ and $\delta f_0 = 1.5$ Hz corresponds to an AFD IDM with $\delta f = 1.5$ Hz. In other words, without the accelerating factor k, the SFS method reduces to the AFD method. Basically, the SFS IDM brings together features from both AFD and SMS by shifting down and narrowing the original NDZ of UFP/OFP.

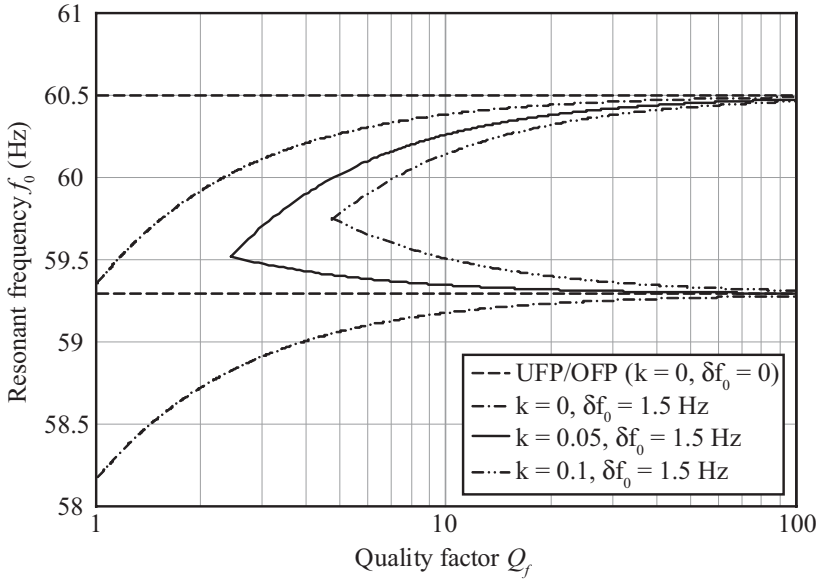


Fig. 3.11 Nondetection zone for SFS

3.5.6 IDM Dymola Blocks

Dymola blocks have been created to generate the PV system inverter output current commands i^* for the AFD, SMS, and SFS IDMs as per Equations (3.15), (3.22), and (3.31), respectively. One such block is shown in Fig. 3.12. The Modelica code within the block for each IDM is provided in Appendix A. The block takes as inputs the voltage v_{PCC} to which the current command is synchronized, V_{PCC} from the output of the rms

computation block shown in Fig. 3.3, the frequency f of the v_{PCC} from the output of the frequency computation block shown in Fig. 3.4, and the desired output power P_{out}. A disable port is also included to suppress the output of the block if either abnormal voltages or abnormal frequencies are detected.

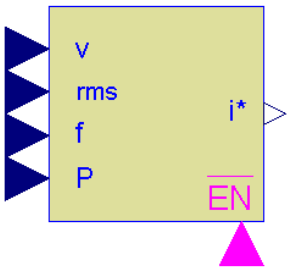


Fig. 3.12 Dymola block for IDM current command generation

3.6 Output Stage Simulations

In Dymola, all the blocks discussed above can be put together and simulated with the microinverter output stage as shown in Fig. 3.13. The rms of the grid voltage is set to 240 V for the line-to-line voltage of a typical household split-phase system. A voltage source block is used in lieu of the bus capacitor. Its voltage is nominally set to 400 V to ensure that the bus voltage, even in the presence of ripple, is always above the grid voltage peak of 339.4 V. A local resonant RLC load with adjustable Q_f and f_0 is placed in parallel with the microinverter output stage and the grid.

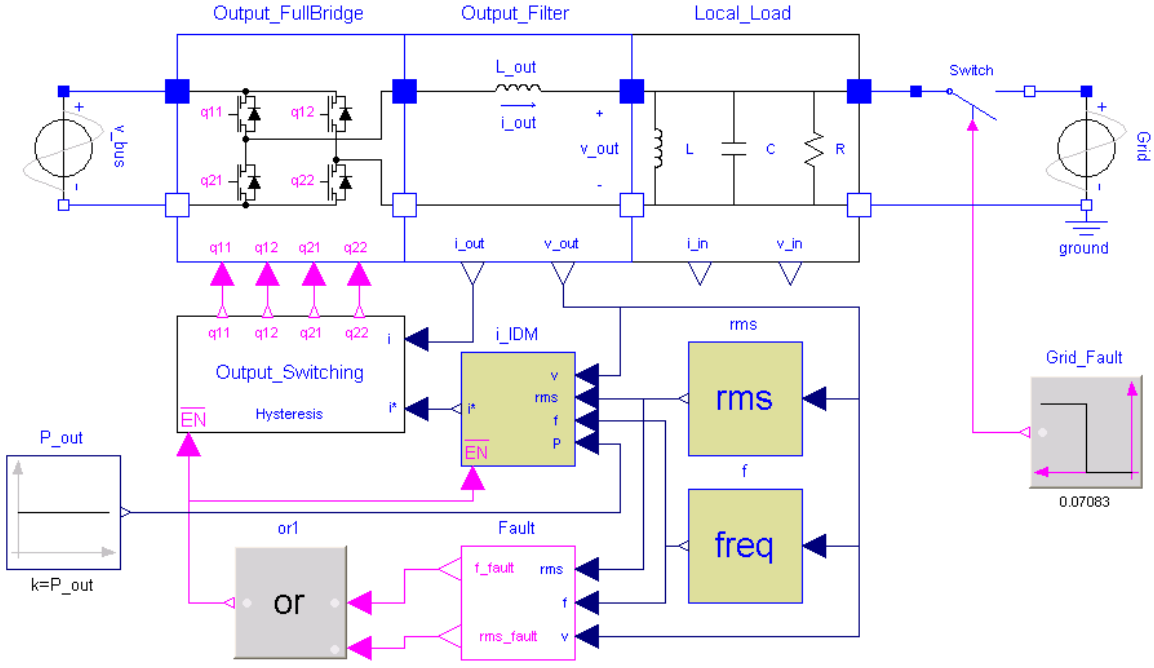


Fig. 3.13 Dymola setup to simulate output stage

Given the intricate current command waveforms needed for the AFD and SFS IDMs, hysteresis control [51] lends itself well to the control of the output current i_{out}. With the denotation Δi_{out} for the desired peak-to-peak output current ripple, the generation of the switching signals for the output full-bridge inverter using hysteresis control is given as

$$q_{o11} = q_{o22} = \begin{cases} 1, & \text{if } i_{out} < i^* - \Delta i_{out}/2 \\ 0, & \text{otherwise} \end{cases}$$
$$q_{o12} = q_{o21} = \begin{cases} 1, & \text{if } i_{out} > i^* + \Delta i_{out}/2 \\ 0, & \text{otherwise} \end{cases} \quad . \tag{3.36}$$

One shortcoming of hysteresis control is that the switching frequency cannot be fixed and is dictated by Δi_{out} and the output inductor L_{out} in this configuration. With L_{out} set to 15 mH and Δi_{out} to 0.2 A, the switching frequency was found to range from about 18 to 65 kHz in simulation. Lower switching frequencies can be achieved by increasing L_{out} and/or Δi_{out} at the expense of a bigger magnetic component and more distorted i_{out}. However, hysteresis control is very robust [51] in that it prevents any ripple on the bus from being transmitted to the output and distorting i_{out}.

In the Fig. 3.13 setup, the outputs of the rms and frequency blocks are fed into a fault detector block, which checks for abnormal conditions at every zero-crossing of v_{PCC}. The rms and frequency fault signals generated by the block are ORed to provide a single fault signal. If a fault on either the rms or the frequency is detected, the fault signal goes high after a prescribed number of line cycles and disables the output switching block and the IDM current command block. The Modelica code within the fault detector block is provided in Appendix A. Hereinafter, P_{out} will be set to 185 W to be consistent with the maximum power point of the PV module used in the input stage in Chapter 2. An islanding condition is created by opening the switch at 0.07083 s, which coincides with one of the peaks of v_{PCC}.

3.6.1 AFD Performance

The setup in Fig. 3.13 was simulated with the AFD IDM current command with δf = 1.5 Hz and the local RLC load set to Q_f = 1.0 and f_0 = 60 Hz (i.e. 311.4 Ω, 0.826 H, and 8.52 μF). Under normal conditions (that is, no islanding), one cycle of the output current i_{out} is shown in Fig. 3.14, with its fast average clearly being i^*, as prescribed by the hysteresis control scheme defined in (3.36).

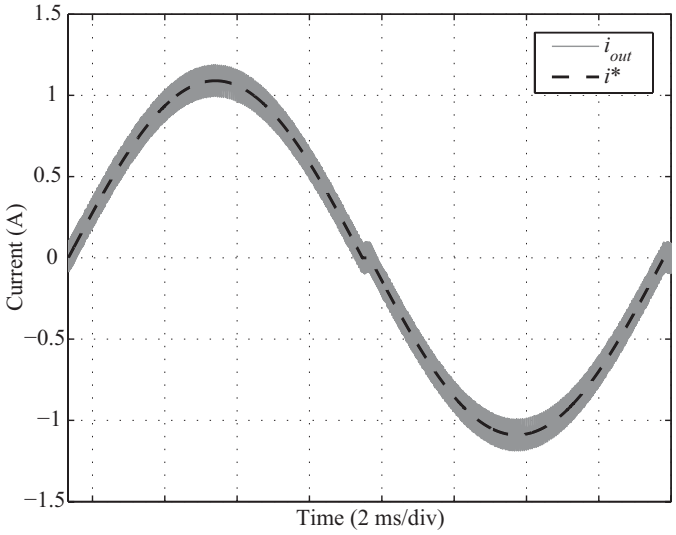


Fig. 3.14 i_{out} and i^* when δf = 1.5 Hz with AFD IDM

The harmonic content of i_{out} is illustrated in Fig. 3.15—only the first 40 harmonics are presented, conforming with IEEE 1547.1 Clause 5.11.1. These harmonics meet the IEEE 1547 limits (see Table 3.3), which are also included in Fig. 3.15. The total harmonic distortion, computed using the first 40 harmonics as per IEEE 1547.1 Clause 5.11.1, is 2.5%, which is well within the 5% limit. If all harmonics are included, the THD goes up to 8.0%. Lower THD can be achieved by decreasing the ripple current Δi_{out}; however, due to the hysteresis control, the switching frequency range will be higher, with more switching events, thus increasing the processing time in simulation and switching losses in hardware.

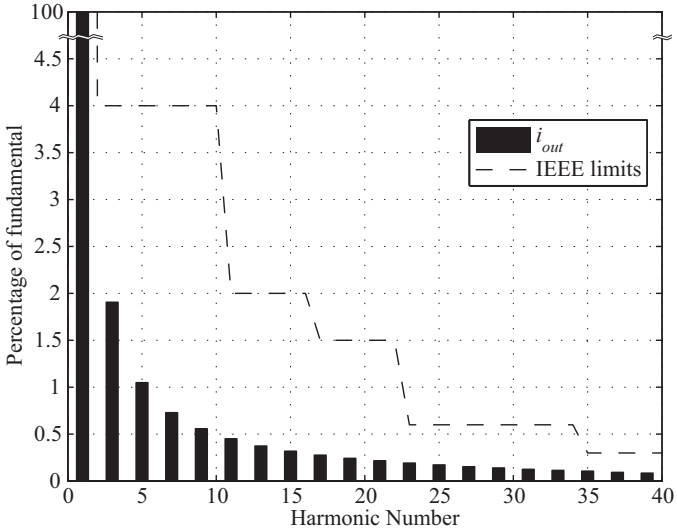


Fig. 3.15 Harmonic content of i_{out} when δf = 1.5 Hz with AFD IDM

The time-domain simulation waveforms for i_{out}, v_{PCC}, and f are shown in Fig. 3.16. As can be seen, f starts drifting soon after the grid is disconnected. The frequency fault is detected in the following line cycle when f crosses the upper limit, but the fault detector block is set to wait three line cycles before setting the fault signal high. Once the fault signal goes high, the output switching and i^* are disabled, thus turning off the output stage of the microinverter and stopping power delivery to the local RLC load. The islanding condition is detected in about five line cycles from the formation of the island, well within the allowed two seconds.

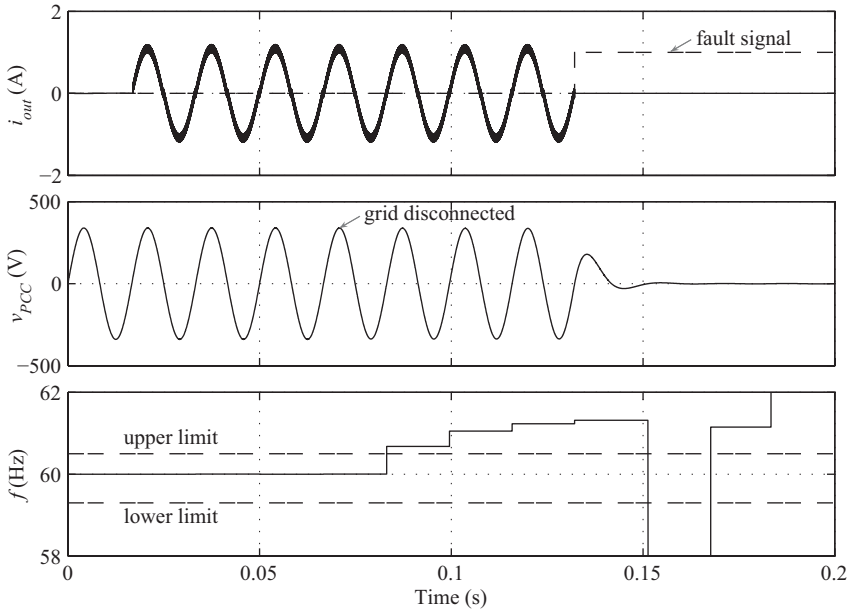


Fig. 3.16 AFD islanding detection when $\delta f = 1.5$ Hz, $Q_f = 1.0$, and $f_0 = 60$ Hz

With the local RLC load set to $Q_f = 3.0$ and $f_0 = 60$ Hz (i.e. 311.4 Ω, 0.275 H, and 25.6 μF), Fig. 3.17 shows the resulting waveforms. Referring to Fig. 3.8, such a load falls into the nondetection zone (NDZ) of an AFD IDM with $\delta f = 1.5$ Hz. In other words, the islanding condition would remain undetected. The waveforms in Fig. 3.17 confirm that this is indeed the case. While f starts drifting right after the grid is disconnected, it does not drift far enough to get into the abnormal frequency ranges. Instead, f reaches a steady value that is just lower than the upper limit and the microinverter output stage keeps energizing the local resonant load even two seconds after the formation of the island. Technically, this case validates the NDZ shown in Fig. 3.8, but does not violate IEEE 1547 Clause 4.4.1, which only applies to a load nominally set to have $Q_f = 1.0$ and $f_0 = 60$ Hz.

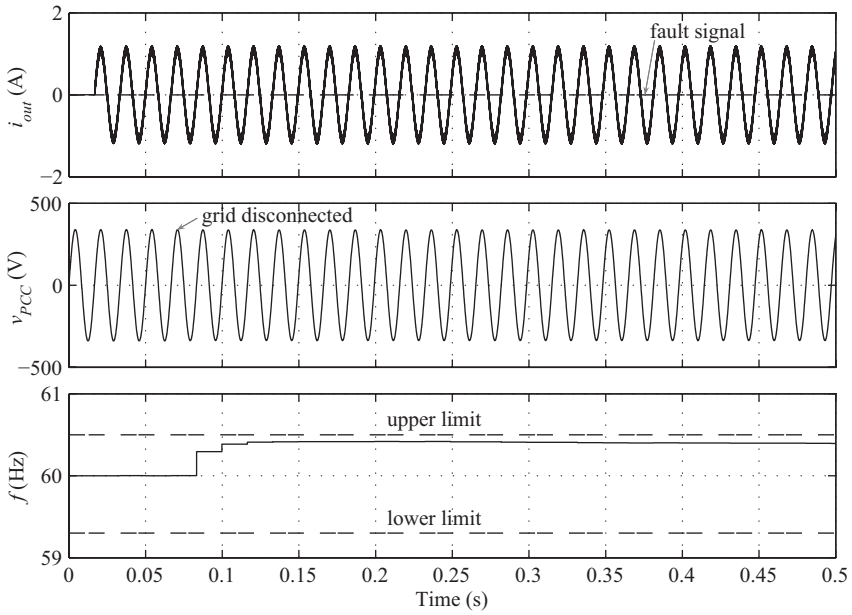


Fig. 3.17 AFD islanding nondetection when δf = 1.5 Hz, Q_f = 3.0, and f_0 = 60 Hz

3.6.2 SMS Performance

Simulating the Fig. 3.13 setup with the SMS IDM current command with θ_m = 10° and an RLC load of Q_f = 1.0 and f_0 = 60 Hz leads to the steady-state i_{out} shown in Fig. 3.18 in the absence of islanding conditions. In this case, i_{out} does not present any distortion, except from the switching ripple. This is confirmed by its harmonic content in Fig. 3.19, dominated by the fundamental, while the switching ripple shows up in the higher harmonics not shown in the figure. THD is 0.01% for the first 40 harmonics and 7.5% with all harmonics included. As for the AFD IDM, the requirements in Clauses 4.3.1 and 4.3.3 of IEEE 1547 are met.

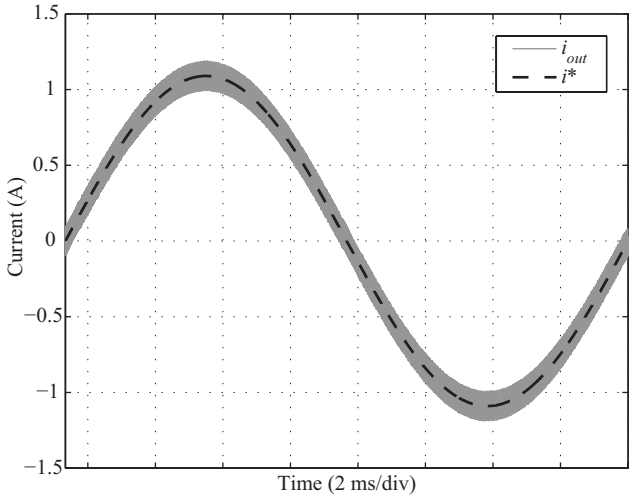


Fig. 3.18 i_{out} and i* when θ_m = 10° with SMS IDM

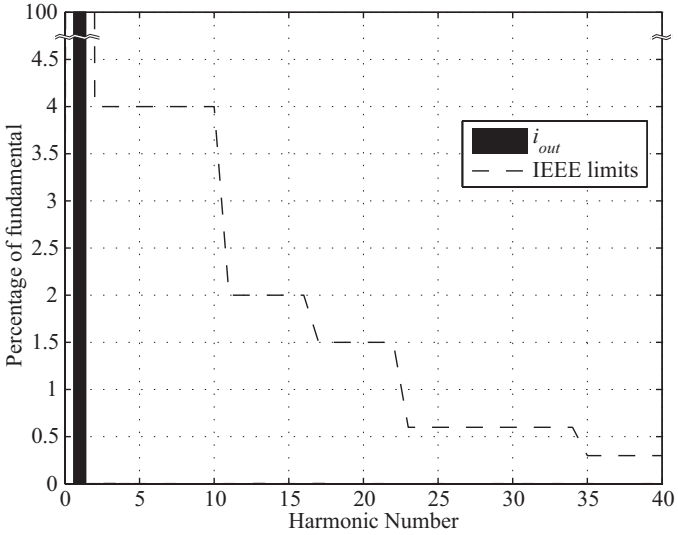


Fig. 3.19 Harmonic content of i_{out} when $\theta_m = 10°$ with SMS IDM

The simulated waveforms are given in Fig. 3.20 and, as expected from Fig. 3.10, the island is detected. Once the island is formed, the frequency starts decreasing and crosses the lower limit about 15 line cycles later. The fault signal is triggered in an additional three line cycles and the output stage ceases to produce power. When the Q_f is changed to 3.0 to provide a resonant load within the NDZ, Fig. 3.21 confirms that islanding is not detected. The frequency f hardly changes after the grid is disconnected and remains in the normal range even after the allowed two seconds.

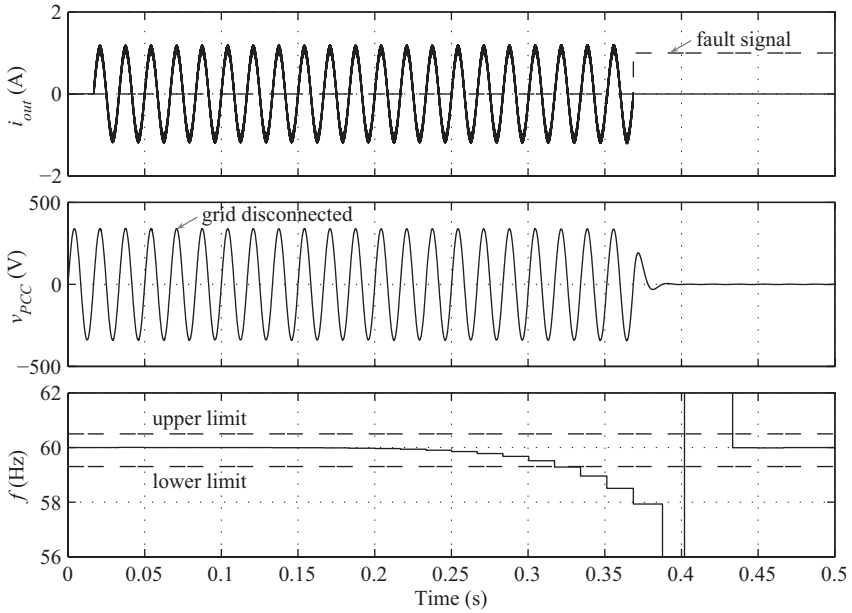


Fig. 3.20 SMS islanding detection when $\theta_m = 10°$, $Q_f = 1.0$, and $f_0 = 60$ Hz

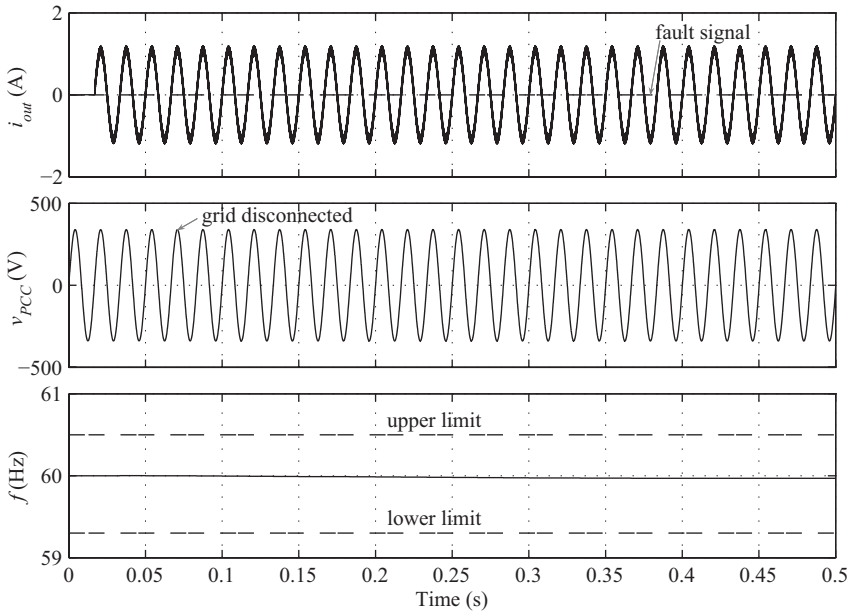


Fig. 3.21 SMS islanding nondetection when $\theta_m = 10°$, $Q_f = 3.0$, and $f_0 = 60$ Hz

3.6.3 SFS Performance

As implied in Section 3.5.5, as long as the utility grid is present, the current command in the SFS IDM is the same as that in AFD IDM when $\delta f_0 = \delta f$. Therefore, with $\delta f_0 =$ 1.5 Hz, during normal conditions, the harmonic content of i_{out} is the same as in Fig. 3.15. With $k = 0.05$, $Q_f = 1.0$, and $f_0 = 60$ Hz, although Fig. 3.22 shows that islanding is detected in about the same time as in the AFD case, the frequency drift is much bigger due to the accelerating factor k.

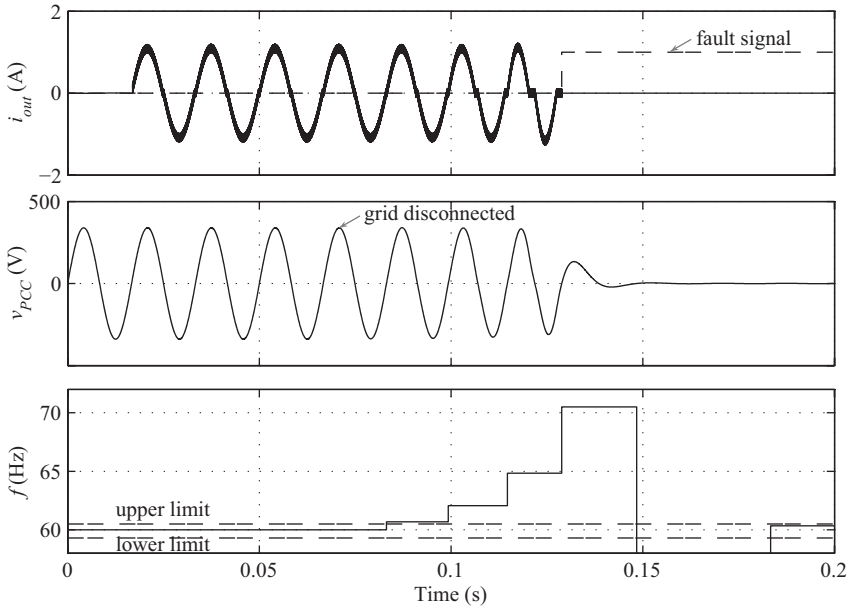


Fig. 3.22 SFS islanding detection when $k = 0.05$, $\delta f_0 = 1.5$ Hz, $Q_f = 1.0$, and $f_0 = 60$ Hz

With $k = 0.05$ and $\delta f_0 = 1.5$ Hz, Fig. 3.11 dictates that a load with $Q_f = 3.0$ and $f_0 = 59.6$ Hz shall lead to an island being undetected. Simulating the output stage with such a load results in the waveforms in Fig. 3.23. Power is still being delivered to the load after the grid is disconnected and f stays within the acceptable range.

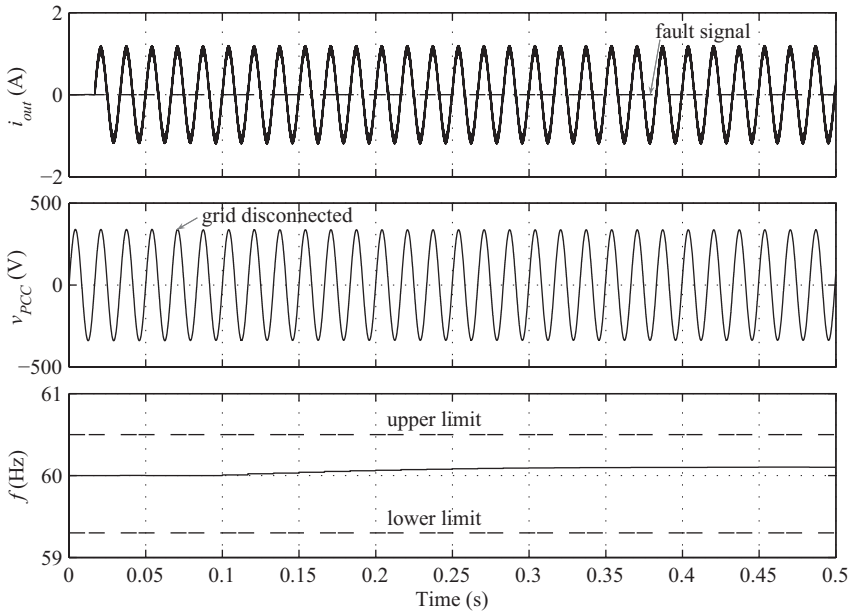


Fig. 3.23 SFS islanding nondetection when $k = 0.05$, $\delta f_0 = 1.5$ Hz, $Q_f = 3.0$, and $f_0 = 59.6$ Hz

It is interesting to note that, while the above simulations verified that the NDZs derived for the AFD, SMS, and SFS IDMs correctly predicted the detection and nondetection of an island, they do not provide any information about the duration of the island before it is detected, if it can be detected. Therefore, there might be cases that take more than two seconds to detect the formation of an island.

3.7 Average-Value Model

From the above, it can be seen that, due to the use of hysteresis control, the inverter output current has a fast average that is equal to the commanded current. The switching ripple can be neglected without any loss in the dynamics of the system. An average-value model (AVM), shown in Fig. 3.24, can be devised for the output inverter. The fast-average output current can be modeled as a controlled current source equal to the current command i^* and, assuming an ideal inverter, the input current source is governed by

$$i_{in} = \frac{v_{out} i_{out}}{v_{in}} = \frac{v_{out} i^*}{v_{in}}. \tag{3.37}$$

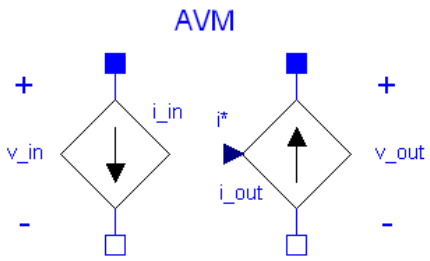


Fig. 3.24 Dymola average-value model for output full-bridge inverter

The output full-bridge inverter, along with the output filter, can thus be replaced by the AVM block as in Fig. 3.25. Since switching is neglected, the output switching block with hysteresis control is removed and the current command i^* is fed directly into the AVM such that $i_{out} = i^*$.

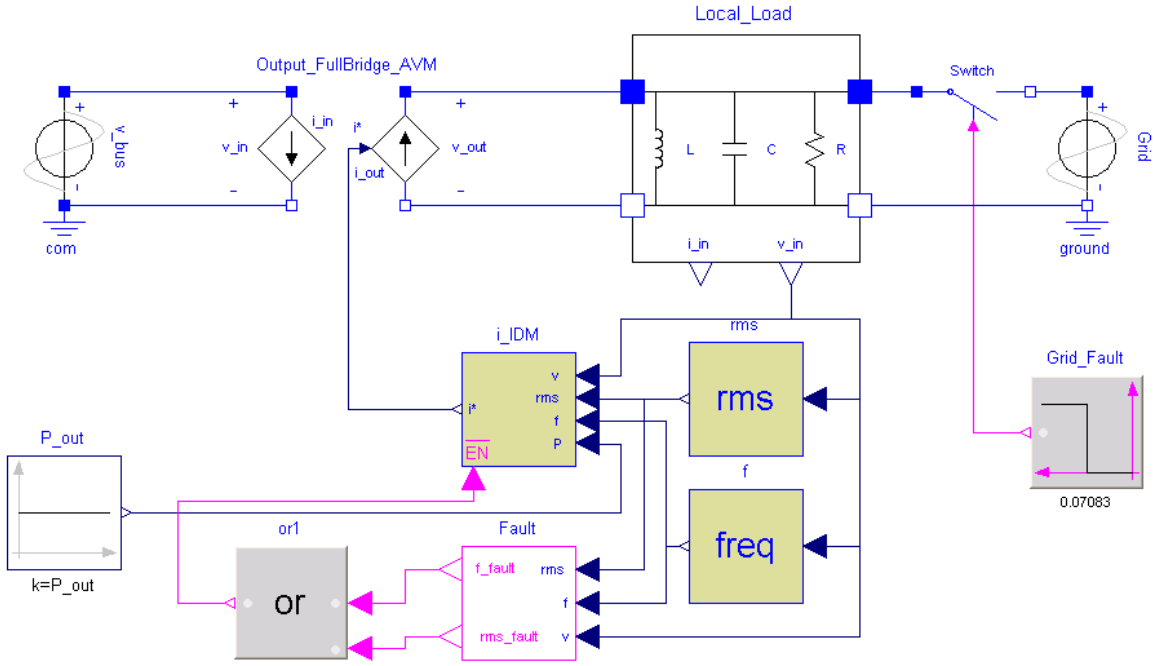


Fig. 3.25 Dymola output stage setup using output full-bridge AVM

With the resonant RLC load set to $Q_f = 1.0$, and $f_0 = 60$ Hz, the above setup was simulated using AFD, SMS, and SFS current command blocks. The corresponding time-domain waveforms are presented in Figs. 3.26–3.28, respectively. While the waveforms for AFD and SFS match the switch-level waveforms perfectly, those for SMS are slightly different in that the frequency drifts in the opposite direction. This is because, based on Fig. 3.9, there are two stable points—one above the nominal 60-Hz grid frequency and the other below. Apart from this difference, islanding is detected in about the same amount of time. Additional simulations have also confirmed that the NDZs for each of

the three IDMs apply to the output stage using the full-bridge inverter AVM. Using the AVM instead of the switch-level version of the output full-bridge inverter not only decreases the simulation time, but also allows for the multiple simulations of several microinverters running in parallel with different permutations of IDMs as will be covered in Chapter 5.

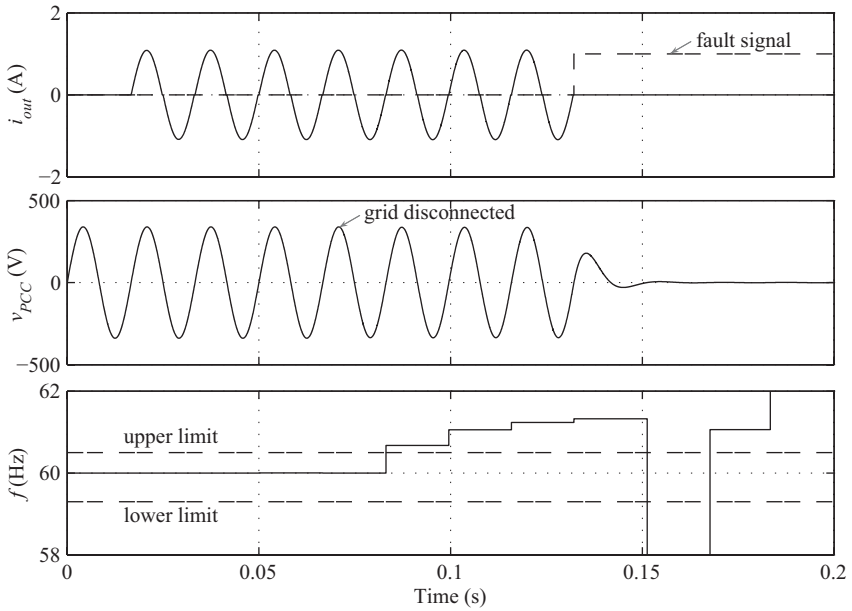


Fig. 3.26 AFD islanding detection with AVM when δf = 1.5 Hz, Q_f = 1.0, and f_0 = 60 Hz

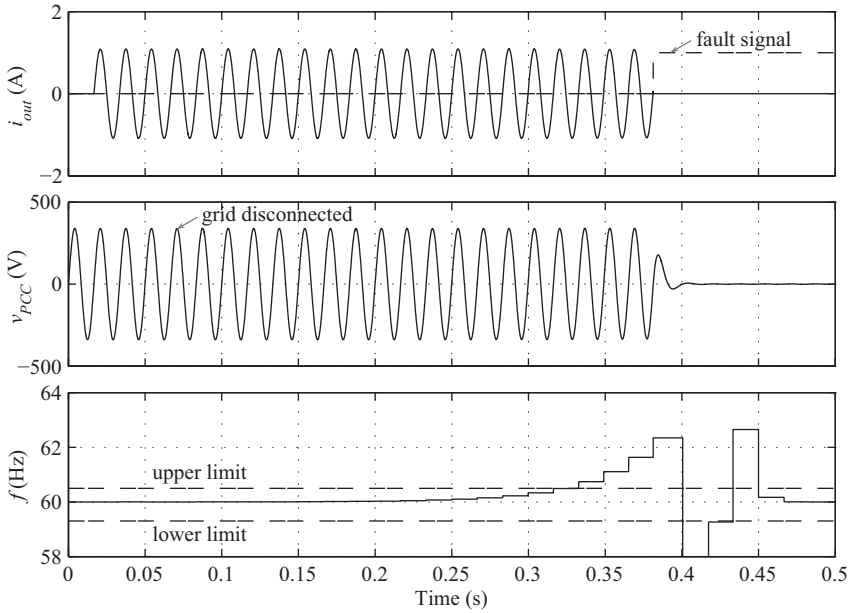


Fig. 3.27 SMS islanding detection with AVM when θ_m = 10°, Q_f = 1.0, and f_0 = 60 Hz

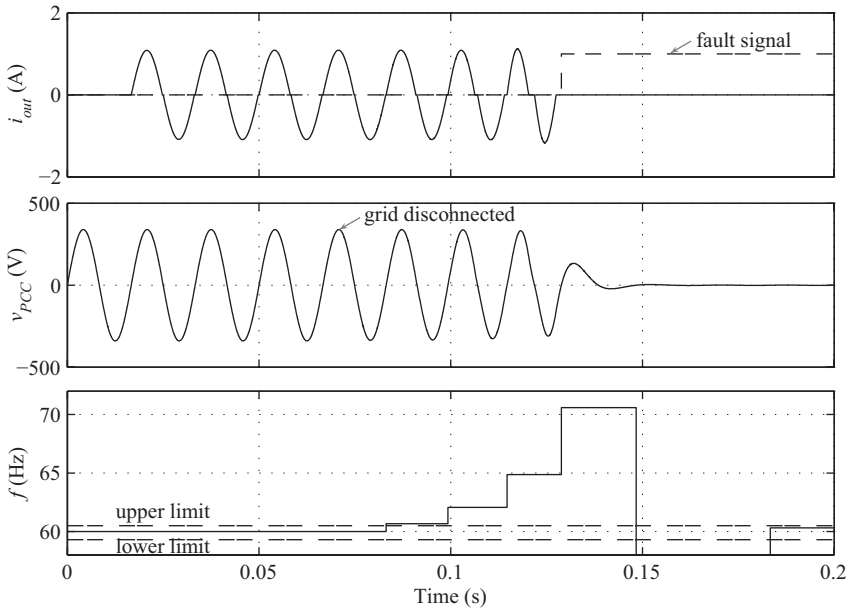


Fig. 3.28 SFS islanding detection with AVM when $k = 0.05$, $\delta f_0 = 1.5$ Hz, $Q_f = 1.0$, and $f_0 = 60$ Hz

4 ENERGY STORAGE

4.1 Overview

The input and output stages of the microinverter have been analyzed separately in Chapters 2 and 3, respectively. This chapter examines the overall operation and control of the interconnection of the two stages forming the microinverter, which when paired with a photovoltaic (PV) module at the input forms an ac PV module. More specifically, the management of the resulting double-frequency energy when connecting the ac PV module to the utility grid, as shown in Fig. 4.1, will be investigated.

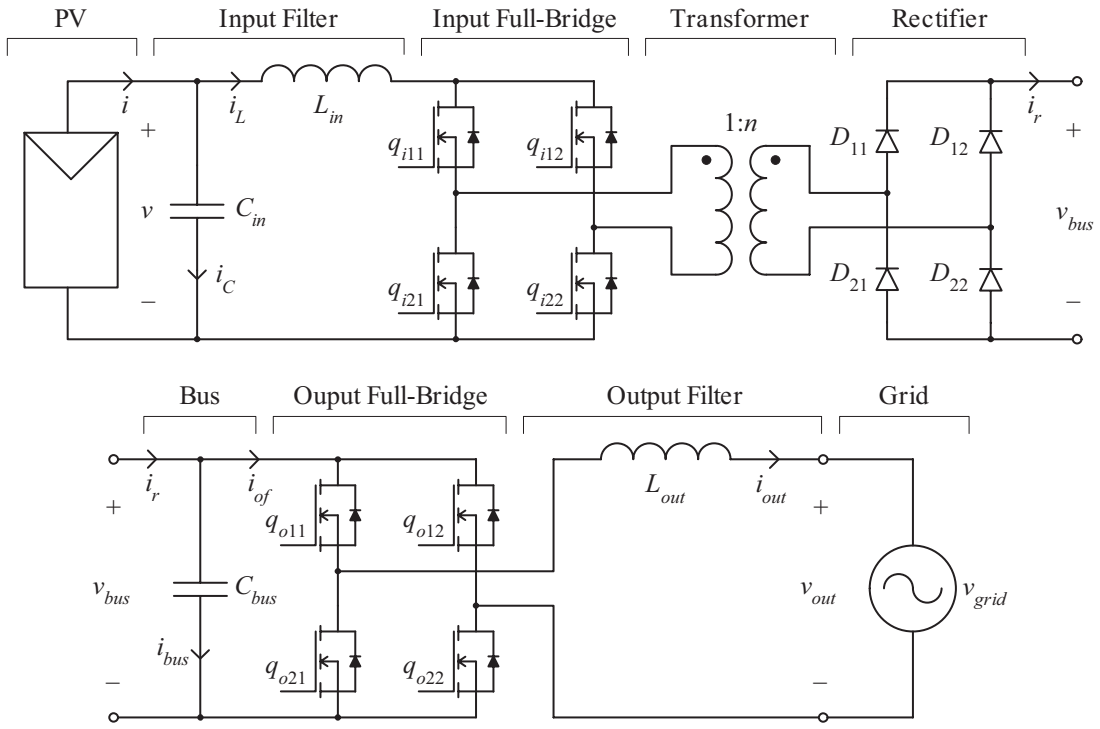


Fig. 4.1 AC PV module connected to the utility grid

With the ac PV module connected to the grid, its output voltage v_{out}, which in this case is the same as the grid voltage v_{grid}, can be formulated as

$$v_{out}(t) = \sqrt{2}V_{out}\sin(\omega t)\,, \tag{4.1}$$

where V_{out} is the root-mean-square (rms) of v_{out} and ω is angular frequency given by

$$\omega = 2\pi f\,, \tag{4.2}$$

with f being the frequency of v_{grid}. Assuming hereinafter that the ac PV module always has unity power factor, the output current i_{out} can be expressed as

$$i_{out}(t) = \sqrt{2}I_{out}\sin(\omega t)\,, \tag{4.3}$$

where I_{out} is the rms value of i_{out}. The instantaneous output power p_{out} is thus

$$p_{out}(t) = v_{out}(t) i_{out}(t) = 2V_{out} I_{out} \sin^2(\omega t) . \tag{4.4}$$

With the fact that the average output power P_{out} is

$$P_{out} = V_{out} I_{out} \tag{4.5}$$

and some trigonometric manipulation, (4.4) can be written as

$$p_{out}(t) = P_{out} - P_{out} \cos(2\omega t) = P_{out} + p_{df}(t) . \tag{4.6}$$

Equation (4.6) implies that p_{out} consists of a dc component P_{out} and a ripple component p_{df} varying at twice the grid frequency. For the case where P_{out} = 185 W (matching the maximum photovoltaic (PV) module power in Chapter 2) and f = 60 Hz, Fig. 4.2 shows how p_{out} varies with time.

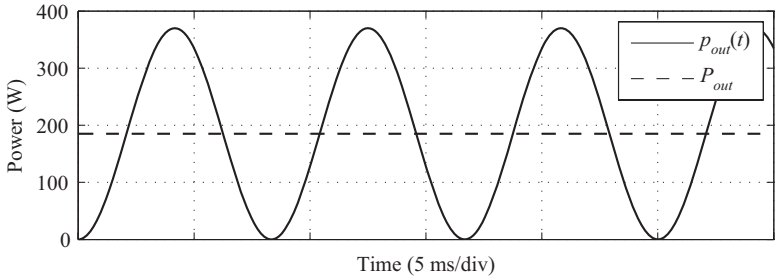


Fig. 4.2 Microinverter instantaneous output power

Ideally, the PV module dc power p equals P_{out}. Therefore, conservation of energy dictates that the double-frequency power p_{df}, shown explicitly in Fig. 4.3, should be managed elsewhere within the microinverter. Separating p_{df} from P_{out} is termed "power decoupling" in [25, 52]. According to [19], there are two ways of processing p_{df}: passive filters and active filters—one possible implementation of each will be covered hereinafter. While the former can be readily implemented with the topology in Fig. 4.1 as will be shown in Section 4.2, Section 4.3 will show how the latter requires additional circuitry and control.

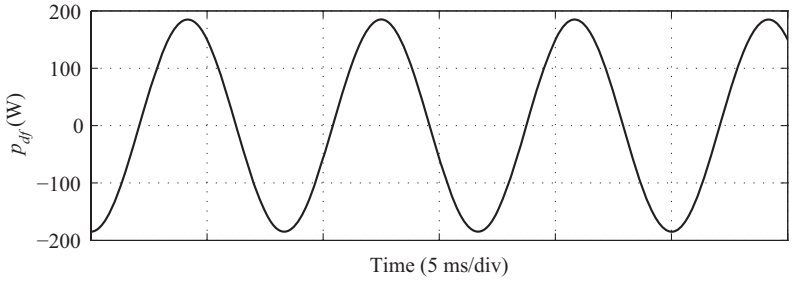


Fig. 4.3 Double-frequency power

4.2 Passive Filter

Integrating the double-frequency power

$$p_{df}(t) = -P_{out}\cos(2\omega t) \tag{4.7}$$

over time results in a double-frequency energy

$$W_{df}(t) = -\frac{P_{out}}{2\omega}\sin(2\omega t)\,, \tag{4.8}$$

which is illustrated in Fig. 4.4 for P_{out} = 185 W and f = 60 Hz. As can be seen, energy has to be stored and delivered in order to generate p_{df}. This can be done passively by using either C_{in} or C_{bus} in Fig. 4.1 [25]. However, since the PV module voltage v is considerably lower than the bus voltage v_{bus}, a much higher capacitance is needed for C_{in} as compared to C_{bus} for a given amount of energy. Therefore, one of the simplest and most effective [19] forms of passive filter is to have C_{bus} handle W_{df} to provide p_{df}.

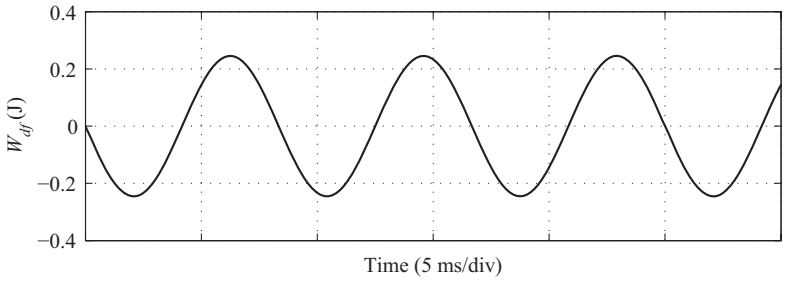


Fig. 4.4 Double-frequency energy

If v_{bus} is maintained high enough above the peak of v_{grid}, it can be allowed to have some ripple without dropping below v_{grid}, thus ensuring proper operation of the output full-bridge converter. Denoting

$$v_{bus}(t) = V_{bus0} + \tilde{v}_{bus}(t)\,, \tag{4.9}$$

where V_{bus0} is the nominal bus voltage and $\tilde{v}_{bus}$ is the allowed ripple, the bus current i_{bus} can be formulated as

$$i_{bus}(t) = C_{bus}\frac{d\tilde{v}_{bus}(t)}{dt} = -\frac{P_{out}}{V_{bus0}}\cos(2\omega t)\,. \tag{4.10}$$

Consequently,

$$\tilde{v}_{bus}(t) = -\frac{P_{out}}{2\omega C_{bus}V_{bus0}}\sin(2\omega t)\,, \tag{4.11}$$

which also exhibits a double-frequency variation, with a peak-to-peak ΔV_{bus} given by

$$\Delta V_{bus} = \frac{P_{out}}{\omega C_{bus} V_{bus0}}. \tag{4.12}$$

Therefore, for a desired ΔV_{bus}, C_{bus} can be computed using

$$C_{bus} = \frac{P_{out}}{2\pi f V_{bus0} \Delta V_{bus}}. \tag{4.13}$$

With the peak of v_{grid} being 339 V for a typical 240-V split-phase system, setting V_{bus0} to 400 V allows for a conservative 60-V ΔV_{bus}. Plugging these numbers, P_{out} = 185 W, and f = 60 Hz, into (4.13) results in a C_{bus} of 20.4 μF. Using a standard 22-μF capacitor for C_{bus} will keep ΔV_{bus} within 55.8 V as long as P_{out} is less than 185 W. This will be the case hereinafter since the PV module has a maximum power point (MPP) of 185 W.

4.2.1 Control Topology

It was shown in Chapters 2 and 3 that the input and output stages of the microinverter can be controlled independently of each other. Since the input stage is dedicated to performing the maximum power point tracking (MPPT) of the PV module, the output stage can be used to regulate v_{bus} by adjusting the output power P_{out}, which eventually adjusts the output current i_{out}. This is similar to the control concept outlined in [53], although applied to different circuit topologies therein. As shown in [53], it also possible to have the input stage regulate v_{bus} while the output stage does the MPPT; but this control method suffers from poor dynamic response and can become unstable if more output power than can be supplied by the PV module is commanded.

On the other hand, if the PV module voltage v can be higher than the peak of v_{grid}, the input boost stage is not needed and the output stage can be used as the sole stage [53, 54]. In this case, controlling the output current can perform both the MPPT and voltage regulation of the passive filter capacitor, which is placed in parallel with the PV module. However, if the passive filter capacitor is not adequately sized, double-frequency voltage oscillation will be imposed on the PV module, thus affecting the energy harvest. This is clearly the case in [54].

Referring back to the microinverter in Fig. 4.1, in steady state, P_{out} should equal the input power p from the PV module less losses in the circuit. However, if the average of v_{bus} is lower than V_{bus0}, P_{out} needs to be reduced to let C_{bus} store more of the energy coming from the input, thus increasing v_{bus}. Conversely, if the average of v_{bus} is higher

than V_{bus0}, P_{out} has to be increased to reduce the amount of energy stored in C_{bus}, thereby decreasing v_{bus}. This can be realized by using a proportional-integral (PI) control that adjusts P_{out} by driving the error between the average of v_{bus} and a bus voltage command v_{bus}* to zero. The voltage v_{bus}* is set to be equal to V_{bus0}. The resulting P_{out} is then fed into the islanding detection method (IDM) current command block as covered in Chapter 3. The overall control topology is depicted in Fig. 4.5.

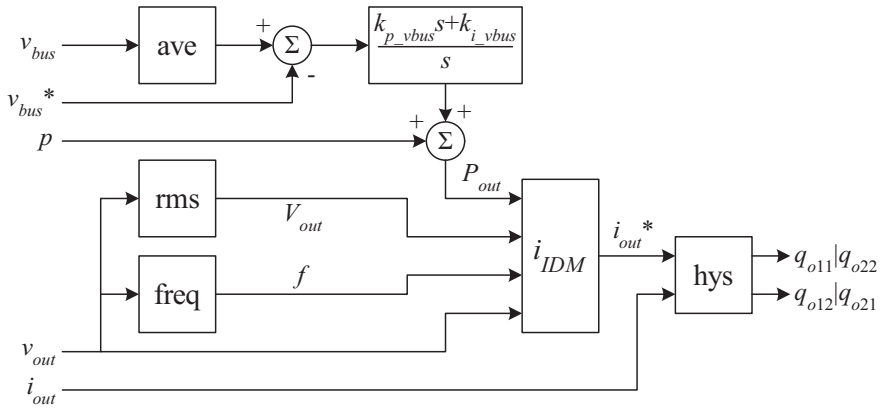


Fig. 4.5 Control topology for passive filter

In this control topology, it is important to ensure not only that the bus voltage control loop has enough bandwidth for v_{bus} to nominally track v_{bus}*, but also that the closed loop is stable. The bandwidth and stability of the bus voltage loop can be verified from the v_{bus}* to v_{bus} transfer function, which is derived in Appendix B as

$$\frac{v_{bus}(s)}{v_{bus}^*(s)} = \frac{V_{bus0}k_{p_vbus}s + V_{bus0}k_{i_vbus}}{C_{bus}V_{bus0}^2 s^2 + \left(k_{p_vbus}V_{bus0} - I_{out0}V_{out0}\right)s + V_{bus0}k_{i_vbus}}. \tag{4.14}$$

The parameters in (4.14) are set as follows:

$$\begin{aligned} C_{bus} &= 22\ \mu\text{F} \\ V_{bus0} &= 400\ \text{V} \\ k_{p_vbus} &= 1\ \text{A} \\ k_{i_vbus} &= 10\ \text{A/s} \\ V_{out0} &= 240\ \text{V} \\ I_{out0} &= 185\ \text{W}/240\ \text{V} = 0.77\ \text{A} \end{aligned} \tag{4.15}$$

Figure 4.6 shows the resulting magnitude of $v_{bus}(s)/v_{bus}^*(s)$ as a function of frequency. As can be seen, the closed loop has a bandwidth of 24.8 Hz, which is adequate since v_{bus} only has to track a dc value of V_{bus0}.

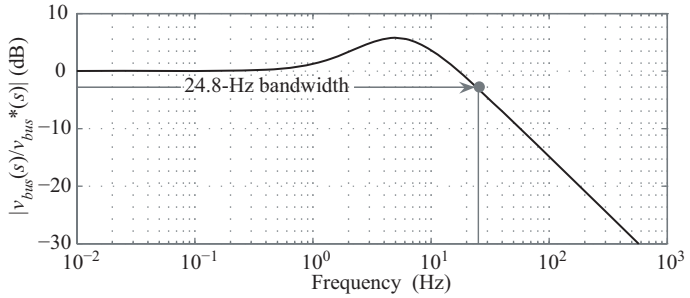


Fig. 4.6 Bandwidth of bus voltage control loop

Figure 4.7 shows the Bode plot of the loop gain of (4.14). The loop gain is expressed as

$$\ell_{vbus}(s) = \frac{V_{bus0}k_{p_vbus}s + V_{bus0}k_{i_vbus}}{C_{bus}V_{bus0}^2 s^2 - I_{out0}V_{out0}s}. \tag{4.16}$$

The plot confirms that the bus voltage control loop is stable with a phase margin of 57°.

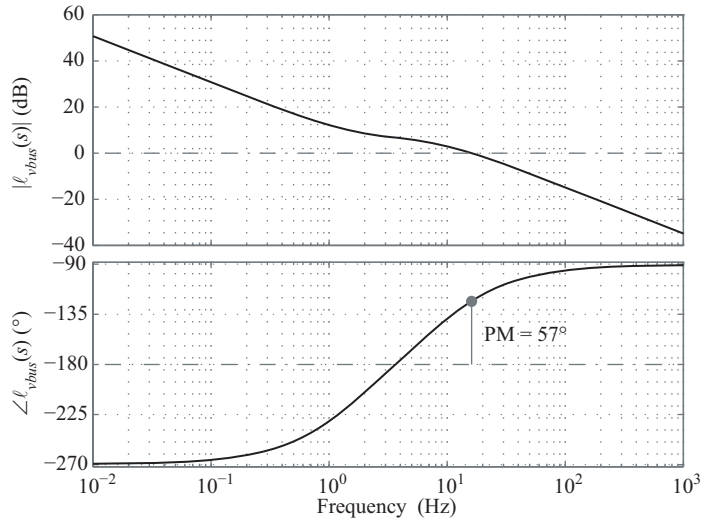


Fig. 4.7 Bode plot of bus voltage control loop gain

On the other hand, it is interesting to see that the transfer function $v_{bus}(s)/i_{out}(s)$, derived in Appendix B and given by

$$\frac{v_{bus}(s)}{i_{out}(s)} = -\frac{V_{bus0}V_{out0}}{C_{bus}V_{bus0}^2 s - I_{out0}V_{out0}}, \tag{4.17}$$

has a magnitude that corresponds to an effective bus impedance of about 36 Ω at 120 Hz, as illustrated in Fig. 4.8. At an output current of 0.77 A, as set in (4.15), this impedance translates to a 27.8-V peak voltage or a 55.6-V peak-to-peak ripple—this correlates with the value obtained from (4.12) for ΔV_{bus}.

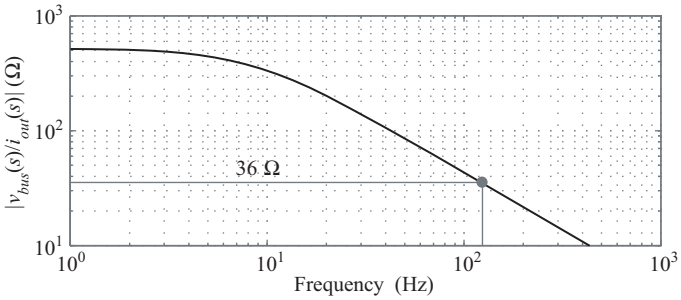


Fig. 4.8 Effective bus impedance

4.2.2 Switch-Level Simulation

Now that the stability of the control topology has been established, the dynamics of the system can be studied by simulating the complete ac PV module, connected to the utility grid. Table 4.1 shows the settings used for the parameters of the microinverter and its control.

Table 4.1 Microinverter and control parameter settings

Parameter	Setting
C_{in}	3.3 μF
L_{in}	100 μH
C_{bus}	22 μF
L_{out}	15 mH
v_{bus}*	400 V
k_{p_acm}	0.3 V/A
k_{i_acm}	10 kV/As
k_{p_vbus}	1 A
k_{i_vbus}	10 A/s

The Dymola setup of the grid-tied ac PV module, with all the required control blocks discussed above and in the preceding chapters, is shown in Fig. 4.9. The output current command block can readily be changed to use one of the three IDMs discussed in Chapter 3—active frequency drift (AFD), slip mode frequency shift (SMS), or Sandia frequency shift (SFS). Since the dynamics of the ac PV module have been found to be the same regardless of the IDM, AFD will be used hereinafter. PV systems with several ac PV modules with different IDMs will be examined in Chapter 5. The insolation G is set to 1000 W/m^2 and the temperature T to 25 ºC such that the PV module has a MPP of 185 W.

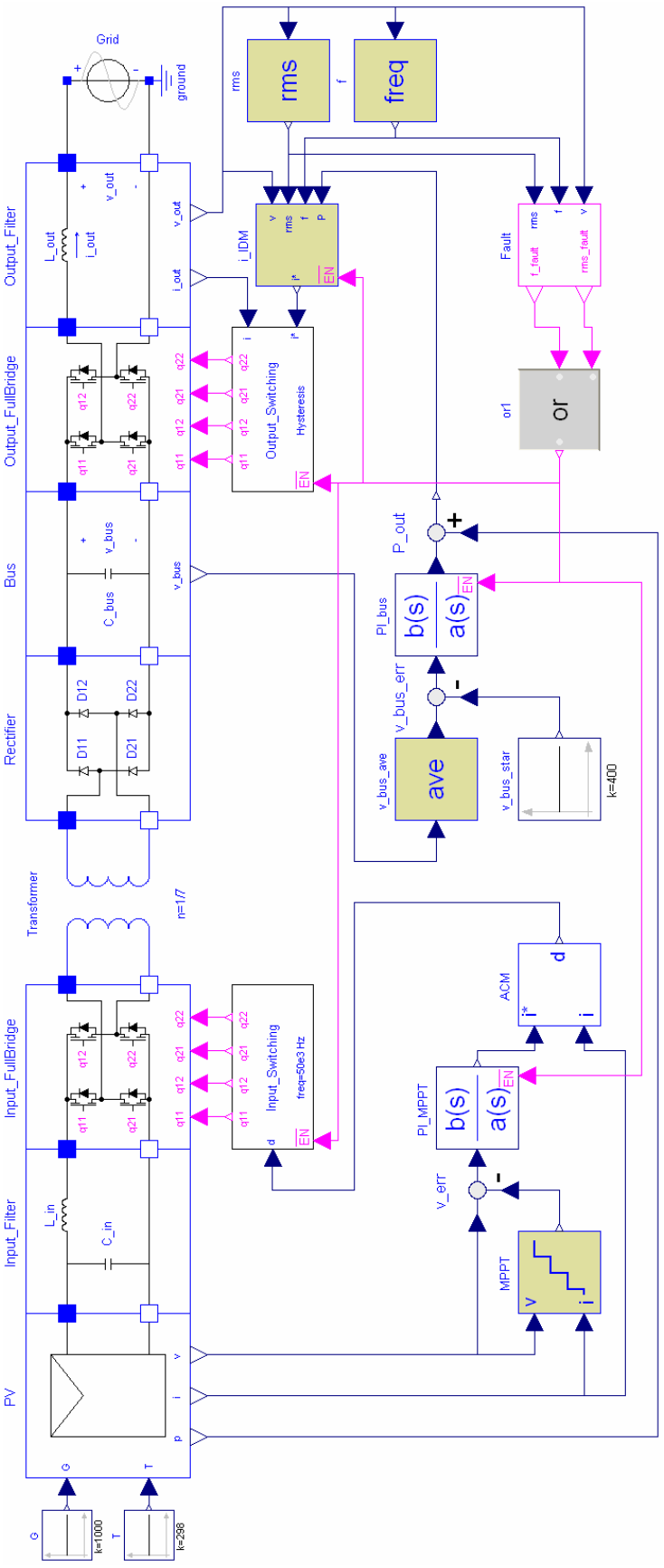


Fig. 4.9 Dymola setup for grid-tied ac PV module with passive filter

Figure 4.10 shows a few key waveforms—v_{bus}, v_{out}, i_{out}, p, and P_{out}—resulting from the simulation of the Dymola setup in Fig. 4.9. The ac PV module is set to start processing power after one line cycle (i.e. after 1/60 s). As can be seen, at start-up, there is an inrush current from the utility grid. This inrush current charges up the bus capacitor C_{bus} through the body diodes of the MOSFETs of the output full-bridge converter, which effectively acts as a rectifier. At the one line cycle mark, the MPPT block rapidly brings p to the MPP of the PV module. However, since the average of v_{bus} is slightly below v_{bus}*, P_{out} is throttled back by the PI control until the average of v_{bus} equals v_{bus}*. At this point, P_{out} closely follows p. The difference between P_{out} and p is due to power loss from diode voltage drops in the rectifier and on resistances in the switches.

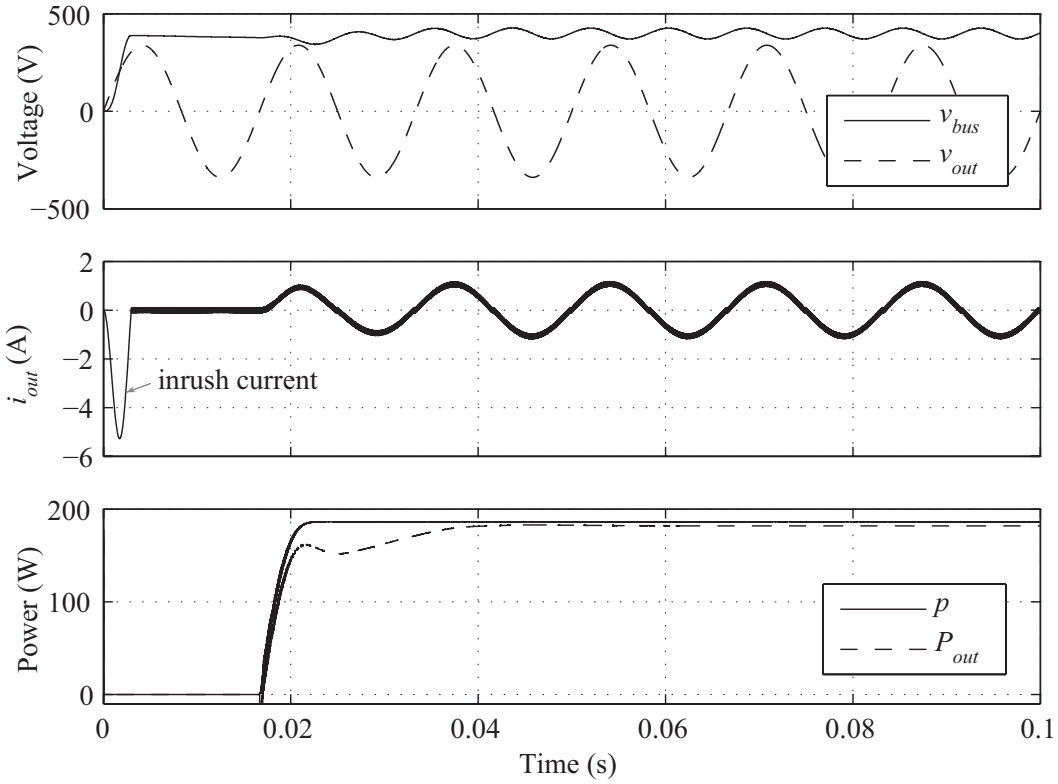


Fig. 4.10 Simulation waveforms of grid-tied ac PV module with passive filter

4.2.3 Average-Value Model Simulation

The detailed simulation of the ac PV module runs successfully, captures all the intricate dynamics of the system, and leads to the expected bus voltage ripple. However, it is computationally intensive and takes relatively long to simulate, making it hard or almost impossible to examine the transient response of the ac PV module under rapid changes in insolation. To alleviate these issues, the input and output full-bridge

converters, along with the input and output filters, can be replaced by the average-value models (AVMs) introduced in Chapters 2 and 3.

Figure 4.11 shows the simulated waveforms resulting from the Dymola setup with the AVMs, shown in Fig. 4.12. As can be seen in Fig. 4.12, the control configuration remains unchanged. Since there is no inrush current due to the lack of switches and diodes, C_{bus} is given an initial voltage condition equal to v_{bus}*. During steady state, P_{out} is higher than p because there is no power loss and also because of the discontinuity in the AFD current that requires more power to be delivered to the grid in a shorter time period. If SMS is used instead of AFD for the output current command, since there is no discontinuity in i_{out}, P_{out} is practically the same as p. Apart from these subtle differences and the switching ripples, these waveforms match those in Fig. 4.10. More importantly, under similar simulation settings, the CPU integration time for the AVM setup is only 4.55 s while it is 164 s for the detailed switch-level simulation.

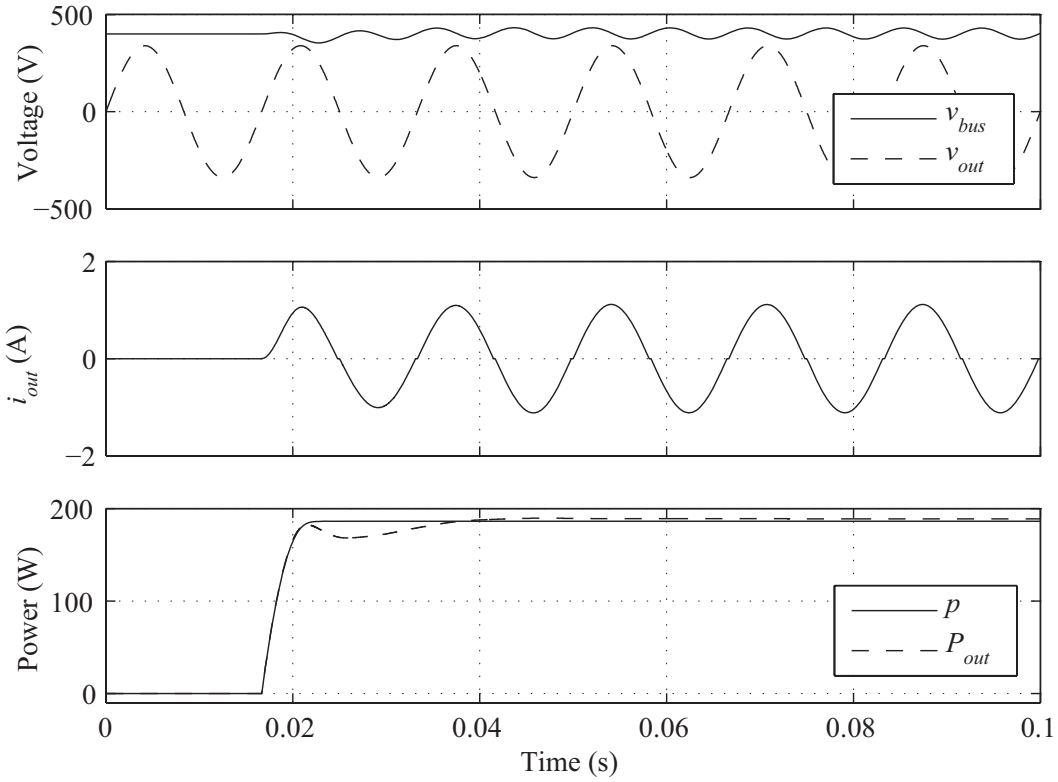


Fig. 4.11 Simulation waveforms of average-value model of ac PV module with passive filter

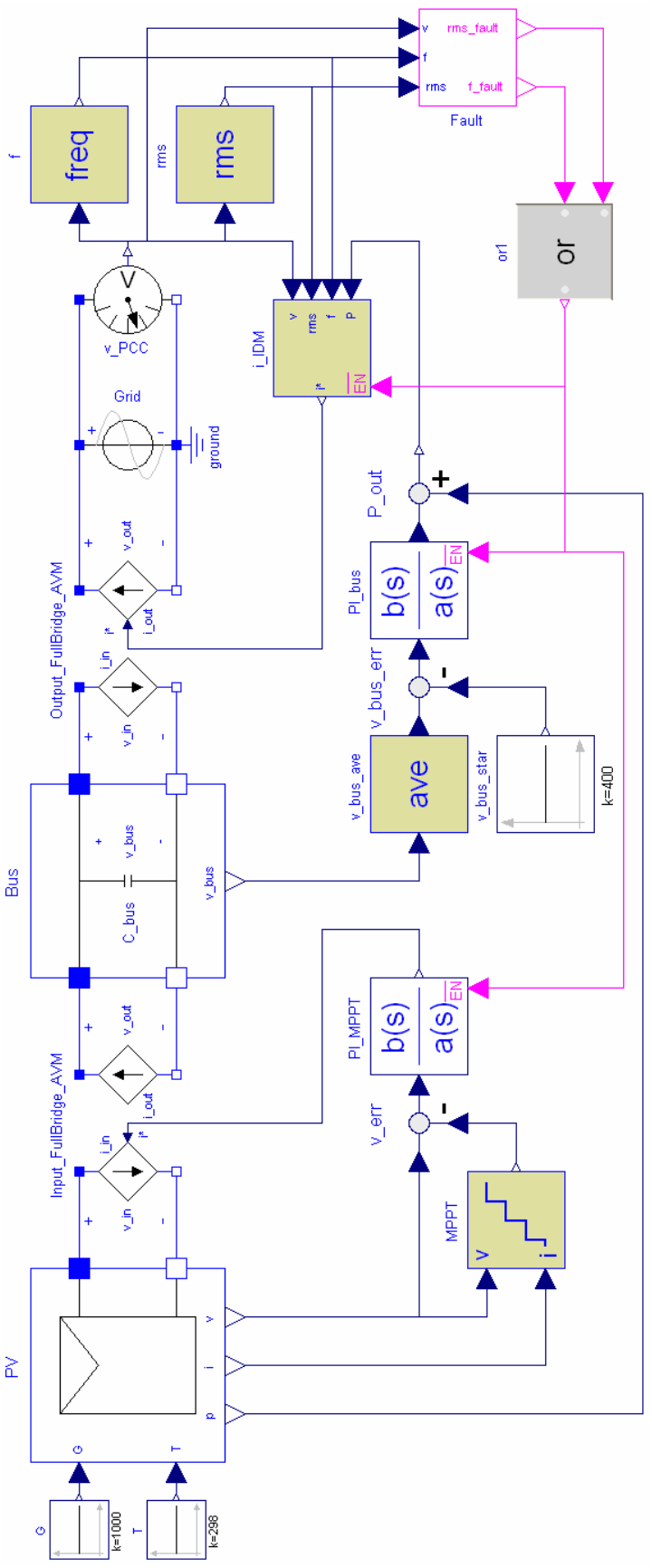


Fig. 4.12 Average-value model of ac PV module with passive filter

With the shorter simulation time for the AVM implementation, the transient response of the ac PV module can be studied. The same varying insolation profile as in Section 2.4.3 is used here. The waveforms shown in Fig. 4.13 confirm the proper behavior of the ac PV module and its control under decreasing and increasing insolation. It is worth noting that the MPPT algorithm still performs perfectly, as in Chapter 2, and that the ripple on v_{bus} gets smaller at lower power, as would be expected from the above derivations.

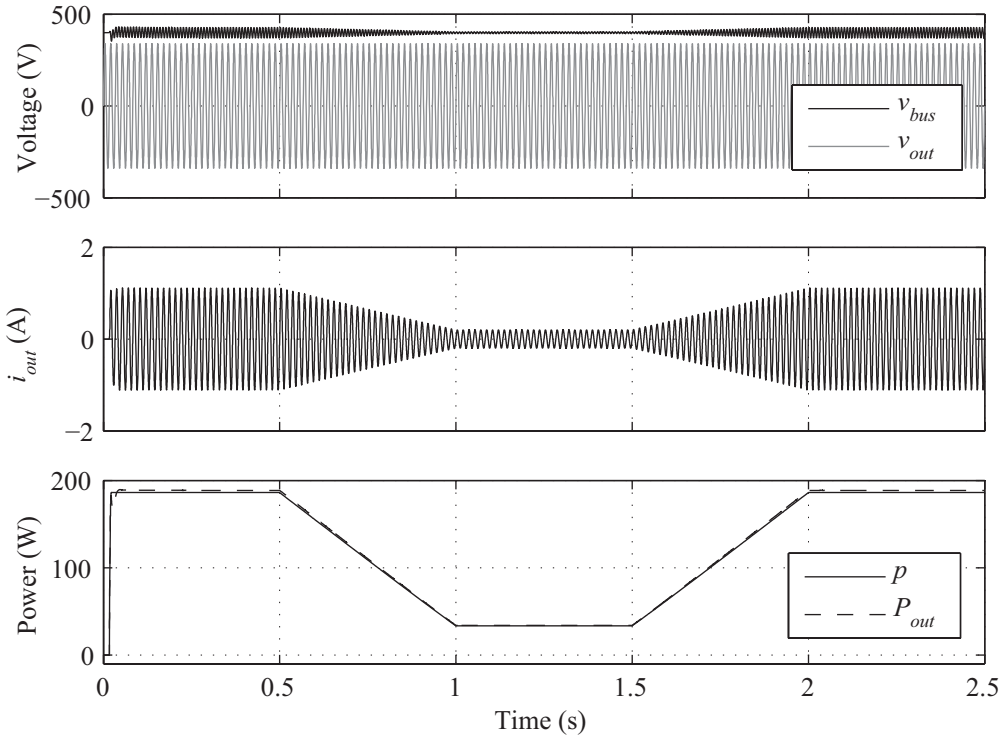


Fig. 4.13 Waveforms under rapid insolation changes for ac PV module with passive filter

4.3 Active Filter

When the bus capacitor C_{bus} is used as the passive filter to manage the double-frequency energy flow, its nominal voltage is constrained to be above the grid voltage v_{grid} and voltage ripple is also limited, resulting in a relatively big capacitor value. The energy stored in C_{bus}, given by

$$W_{bus}(t) = \frac{1}{2} C_{bus} v_{bus}^2(t), \tag{4.18}$$

can be plotted as in Fig. 4.14, when P_{out} = 185 W. As can be seen, the nominal energy stored is 1.76 J, when only the 0.49-J peak-to-peak oscillation accounts for the double-energy flow. This implies that the energy stored in C_{bus} is not being used effectively.

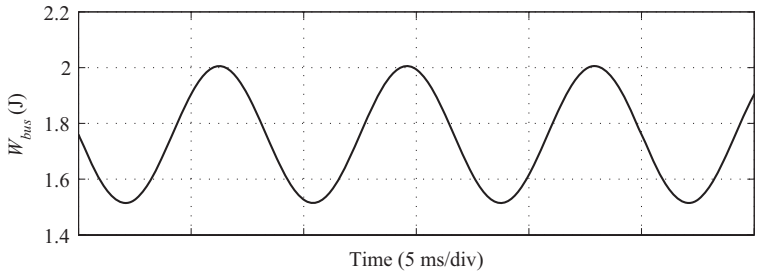


Fig. 4.14 Energy variation in passive filter

If the double-frequency energy flow is actively diverted from C_{bus} to another capacitor C_{af}, appropriately termed the active filter [19], then the voltage across C_{af} can be allowed to have a wider variation without preventing v_{bus} from remaining above the peak of v_{grid}. Based on [19, 55], given the allowable voltage variation, a minimum capacitance value can be derived to store the exact amount of energy needed for p_{df}. The derivation starts by letting the voltage v_{af} across C_{af} be sinusoidal as

$$v_{af}(t) = V_{af} \sin(\omega t + \theta). \tag{4.19}$$

The current i_{af} flowing into C_{af} is

$$i_{af}(t) = C_{af} \frac{dv_{af}(t)}{dt} = \omega C_{af} V_{af} \cos(\omega t + \theta). \tag{4.20}$$

The corresponding instantaneous power p_{af} is thus given as

$$p_{af}(t) = v_{af}(t) i_{af}(t) = \frac{1}{2} C_{af} V_{af}^2 \omega \sin(2\omega t + 2\theta). \tag{4.21}$$

Since the goal of the active filter is to have p_{af} be equal to p_{df} given in (4.7),

$$\frac{1}{2} C_{af} V_{af}^2 \omega \sin(2\omega t + 2\theta) = -P_{out} \cos(2\omega t) = P_{out} \sin\left(2\omega t - \frac{\pi}{2}\right). \tag{4.22}$$

Equating the coefficients and arguments of the sinusoids results in

$$C_{af} = \frac{P_{out}}{\pi f V_{af}^2}, \tag{4.23}$$

which is the minimum capacitance value for a given V_{af}, and

$$\theta = -\frac{\pi}{4}. \tag{4.24}$$

According to [19, 55], since the energy stored in a capacitor depends on the square of its voltage, having

$$v_{af}(t) = \left| V_{af} \sin(\omega t + \theta) \right| \tag{4.25}$$

does not affect the minimum capacitance value, but allows for a two-quadrant converter for the active filter port. One such converter is a synchronous buck converter shown in Fig. 4.15, where v_{af} can vary from 0 V up to v_{bus}.

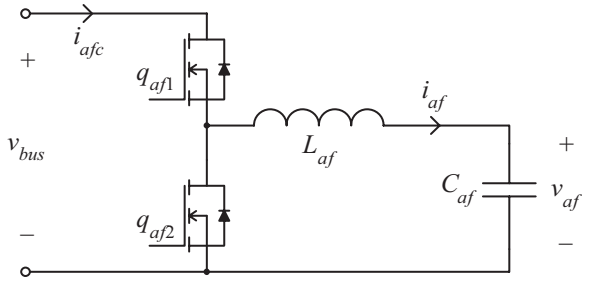


Fig. 4.15 Active filter converter

With V_{af} = 350 V (to leave some margin from a nominal v_{bus} of 400 V), C_{af} is computed to be about 8 μF from (4.23). If a standard 10-μF capacitor is used, V_{af} will be about 313 V. In this case, v_{af} and i_{af}, along with the energy W_{af} stored in C_{af}, are shown in Fig. 4.16. As can be seen, just the right amount of energy of 0.49 J is stored in C_{af}.

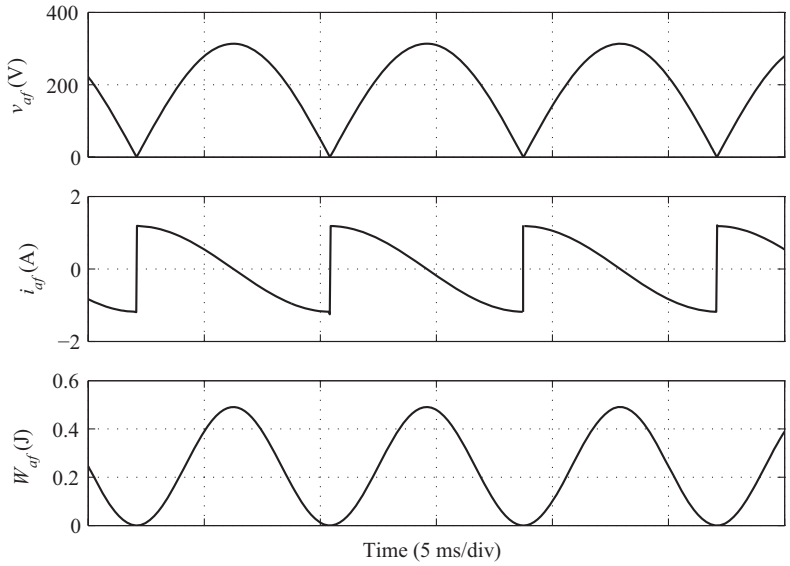


Fig. 4.16 Ideal active filter waveforms

While in theory the waveforms in Fig. 4.16 can be achieved by the buck converter in Fig. 4.15, in practice it is not trivial to ensure that the energy flow during each cycle is perfectly balanced to vary between 0 and 0.49 J. Whenever there is any mismatch between the input power from the PV module and the power delivered to the grid, the energy required from the active filter may vary from cycle to cycle. If W_{af} is allowed to go to zero, there may be times when the active filter will not be able to support p_{df}.

For this reason, it is a good practice to store some extra energy in C_{af}. For example, Fig. 4.17 shows W_{af} when C_{af} stores an additional 0.05 J. The corresponding active filter voltage v_{af} and current i_{af} can then be obtained by

$$v_{af}(t) = \sqrt{\frac{2W_{af}(t)}{C_{af}}}\text{, and} \tag{4.26}$$

$$i_{af}(t) = \frac{p_{af}(t)}{v_{af}(t)} = \frac{p_{df}(t)}{v_{af}(t)}, \tag{4.27}$$

respectively. Both v_{af} and i_{af} are also shown in Fig. 4.17. It is interesting to note that this formulation leads to a continuous current waveform, unlike that in Fig. 4.16—a continuous current command lends itself better to such current controllers as the average current mode (ACM) control used in the input stage of the microinverter.

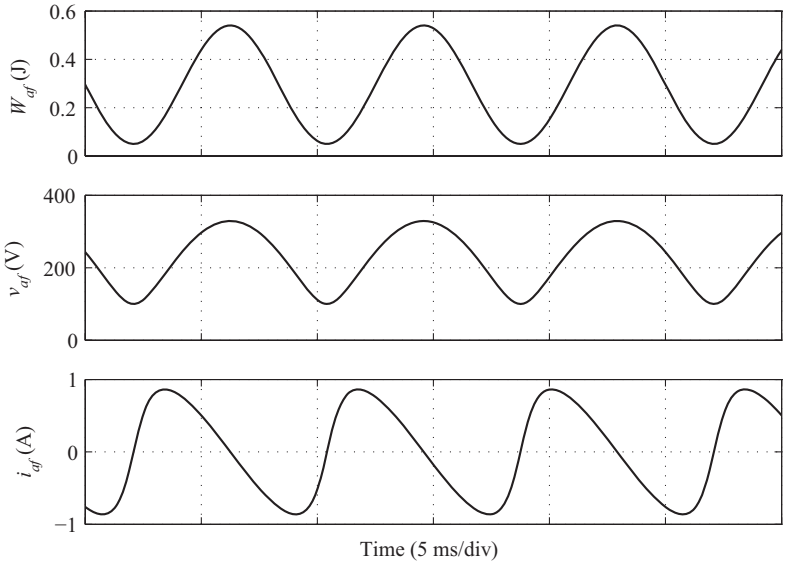


Fig. 4.17 Waveforms resulting from energy offset

4.3.1 Control Topology

Controlling the current i_{af} into C_{af} to follow the current waveform shown in Fig. 4.17 should lead to the corresponding voltage v_{af} and thus the required double-frequency power p_{af}. To generate a current command i_{af}* like i_{af} in Fig. 4.17, based on (4.27), v_{af} and p_{af} need to be known instantaneously. Voltage v_{af} can be easily sensed in hardware. A target p_{af}, denoted as p_{af}*, can be generated based on the fact that diverting the double-frequency energy from C_{bus} implies that the double-frequency voltage ripple on the v_{bus} needs to be mitigated. Based on [56], this can be achieved by using a PI control to force

v_{bus} to be equal to a desired dc voltage command v_{bus}*, as illustrated in Fig. 4.18. An intermediate step, represented by the limit block, is included such that a lower and an upper voltage limit can be placed on v_{af} according to:

$$\begin{cases} i_{af}{}^* = \max\left(0, \hat{i}_{af}\right), \text{ if } v_{af} < V_{af_min} \\ i_{af}{}^* = \min\left(0, \hat{i}_{af}\right), \text{ if } v_{af} > V_{af_max} \\ i_{af}{}^* = \hat{i}_{af}, \text{ otherwise} \end{cases}. \tag{4.28}$$

On the other hand, the average of v_{af} is commanded to be at a desired dc voltage level v_{af}* by using a second PI control to adjust the average output power P_{out}, which is then used to generate the output current command i_{out}*.

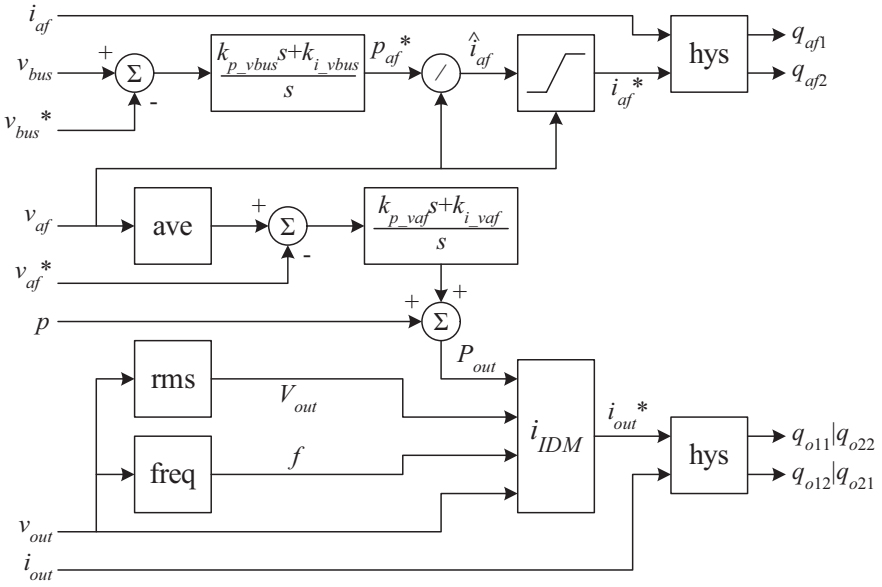


Fig. 4.18 Control topology for active filter, based on [56]

Choosing the appropriate proportional and integral gains for the two PI controls in Fig. 4.18 is essential to ensure that both loops are stable and have sufficient bandwidth for proper tracking. Derived in Appendix B, the close-loop transfer functions for the v_{bus} and v_{af} control loops, along with their corresponding loop gains, are given as follows:

$$\frac{v_{bus}(s)}{v_{bus}{}^*(s)} = \frac{V_{bus0}k_{p_vbus}s + V_{bus0}k_{i_vbus}}{C_{bus}V_{bus0}^2 s^2 + \left(k_{p_vbus}V_{bus0} - I_{out0}V_{out0}\right)s + V_{bus0}k_{i_vbus}} \tag{4.29}$$

$$\ell_{vbus}(s) = \frac{V_{bus0}k_{p_vbus}s + V_{bus0}k_{i_vbus}}{C_{bus}V_{bus0}^2 s^2 - I_{out0}V_{out0}s} \tag{4.30}$$

$$\frac{v_{af}(s)}{v_{af}{}^{*}(s)} = \frac{k_{p_vaf}s + k_{i_vaf}}{C_{af}V_{af0}s^2 + k_{p_vaf}s + k_{i_vaf}} \tag{4.31}$$

$$\ell_{vaf}(s) = \frac{k_{p_vaf}s + k_{i_vaf}}{C_{af}V_{af0}s^2} \tag{4.32}$$

The parameters in (4.29)–(4.32) are set as follows:

$$\begin{aligned} &C_{bus} = 3.3\ \mu\text{F} && C_{af} = 10\ \mu\text{F} && I_{out0} = 0.77\ \text{A} \\ &V_{bus0} = 400\ \text{V} && V_{af0} = 250\ \text{V} && V_{out0} = 240\ \text{V} \\ &k_{p_vbus} = 10\ \text{A} && k_{p_vaf} = 0.5\ \text{A} \\ &k_{i_vbus} = 40\ \text{kA/s} && k_{i_vaf} = 15\ \text{A/s} \end{aligned} \tag{4.33}$$

Figure 4.19 shows that the v_{bus} control loop (4.29) has a bandwidth of 1.8 kHz and Fig. 4.20 confirms the stability of the loop by the 62° phase margin in the Bode plot of (4.30).

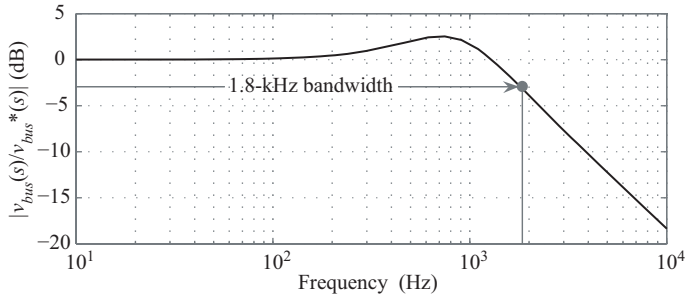


Fig. 4.19 Bandwidth of bus voltage control loop

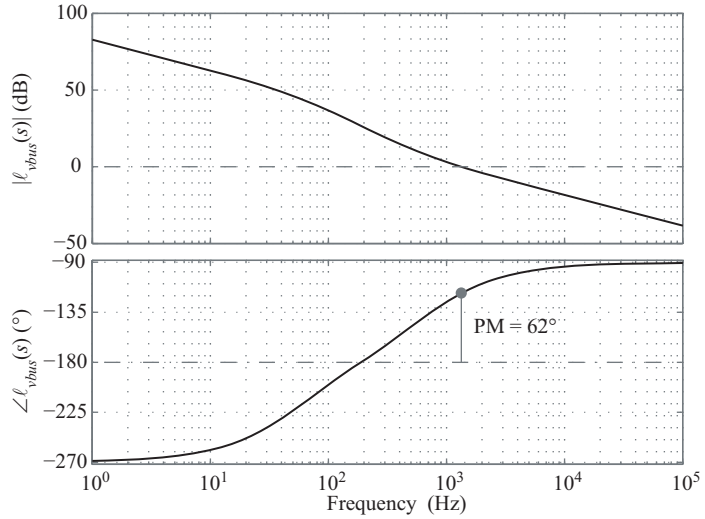


Fig. 4.20 Bode plot of bus voltage control loop gain

Similarly, the v_{af} control loop (4.31) is shown to have a bandwidth of 36.3 Hz in Fig. 4.21, which is sufficient for v_{af} to track the dc value of v_{af}*, and the Bode plot of (4.32) shows a phase margin of 82° in Fig. 4.22.

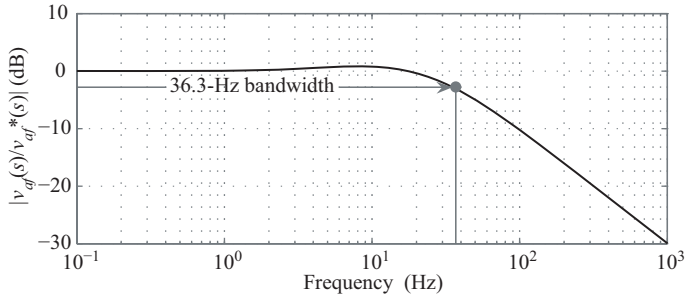


Fig. 4.21 Bandwidth of active filter voltage control loop

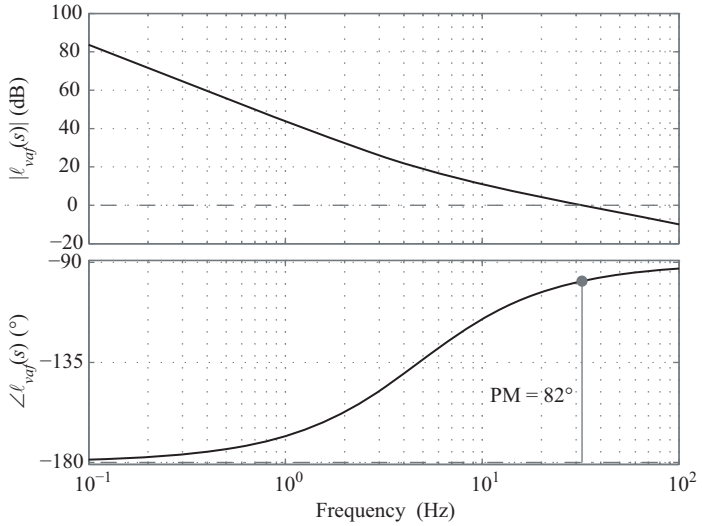


Fig. 4.22 Bode plot of active filter voltage control loop gain

Additionally, Fig. 4.23 shows that the transfer function $v_{bus}(s)/i_{out}(s)$, given by

$$\frac{v_{bus}(s)}{i_{out}(s)} = \frac{V_{bus0}V_{out0}s}{C_{bus}V_{bus0}^2 s^2 + \left(k_{p_vbus}V_{bus0} - I_{out0}V_{out0}\right)s + V_{bus0}k_{i_vbus}}, \tag{4.34}$$

as derived in Appendix B, has a magnitude of 4.54 Ω at 120 Hz. This corresponds to a peak voltage of 3.5 V, which is considerably lower than the passive filter case and confirms that most of the double-frequency energy is expected to be handled by the active filter.

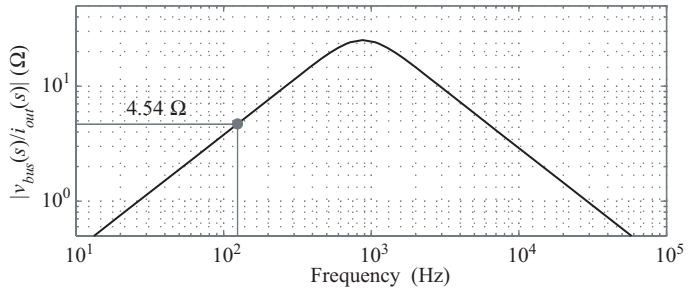


Fig. 4.23 Effective bus impedance in the presence of active filter

4.3.2 Switch-Level Simulation

Figure 4.24 shows simulated waveforms resulting from the detailed switch-level Dymola setup, shown in Fig. 4.25, of the ac PV module with the active filter port. The control is set up as in Fig. 4.18 and the parameters are set as in (4.33). In addition, 1 mH is used for L_{af} and hysteresis control with a 1-A peak-to-peak ripple is employed to control i_{af} to follow i_{af}*. The microinverter starts processing power after one line cycle. The startup transient only lasts for a couple of line cycles before steady state is reached. It is worth noting how i_{af} is limited until v_{af} is brought into range with the PI control adjusting P_{out} accordingly with respect to p. Clearly, the ripple on v_{bus} is minimal and has been confirmed to match the 3.5-V peak mentioned above.

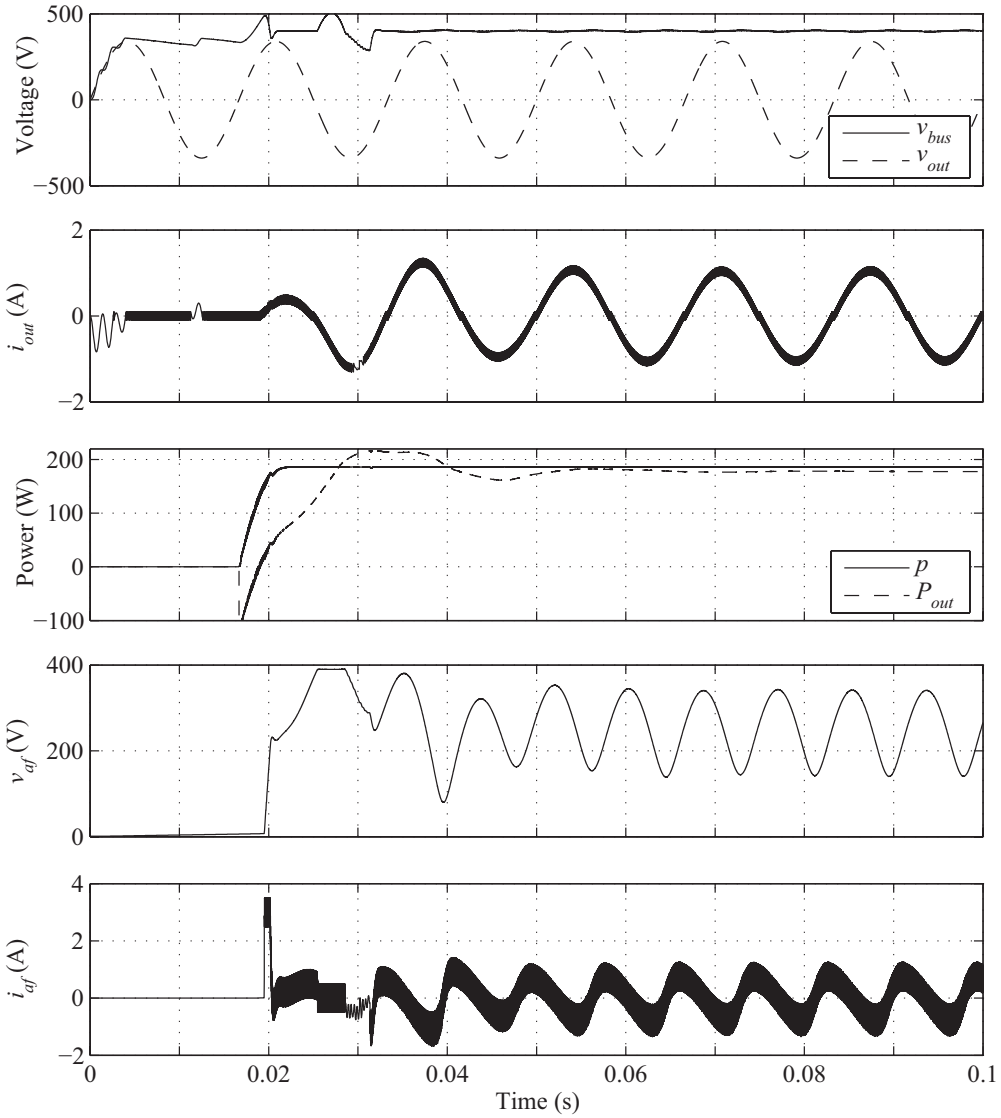


Fig. 4.24 Simulation waveforms of grid-tied ac PV module with active filter

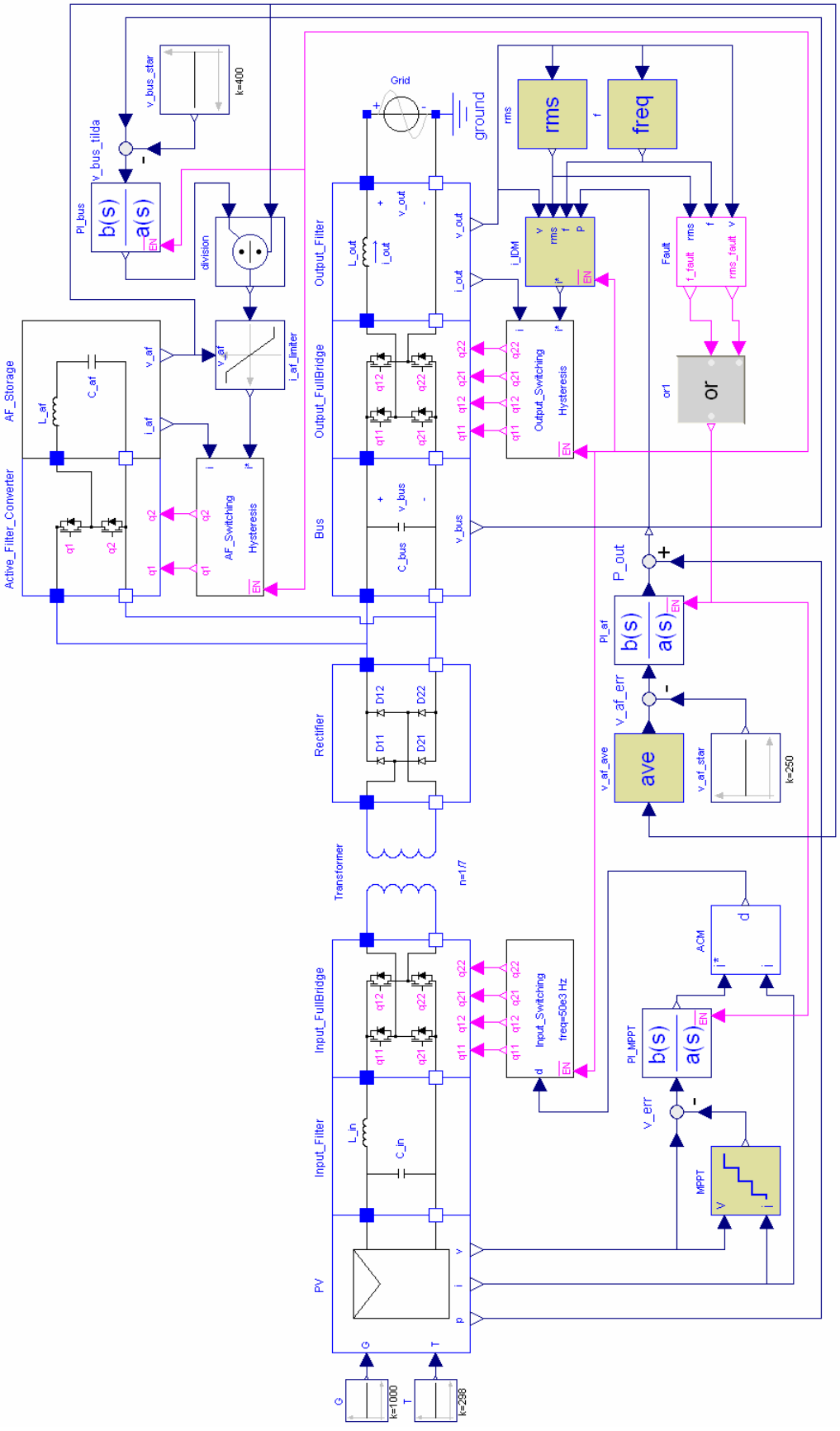


Fig. 4.25 Dymola setup for grid-tied ac PV module with active filter

4.3.3 Average-Value Model Simulation

With the additional active filter port and more switching events, the detailed simulation setup in Fig. 4.25 takes even longer to run than the passive filter setup in Fig. 4.9. The switching converters, together with the filters, can be replaced with the AVMs. The same AVM as the output full-bridge converter can be used for the active filter buck converter. The waveforms shown in Fig. 4.26 result from the Dymola setup in Fig. 4.27. Despite the absence of switching ripples and the need for initial voltage conditions on the capacitors, the waveforms closely match those in Fig. 4.24, during both the startup transient and steady state. Moreover, the CPU integration time reported by Dymola is 6.91 s for the AVM setup and 310 s for the detailed switch-level simulation.

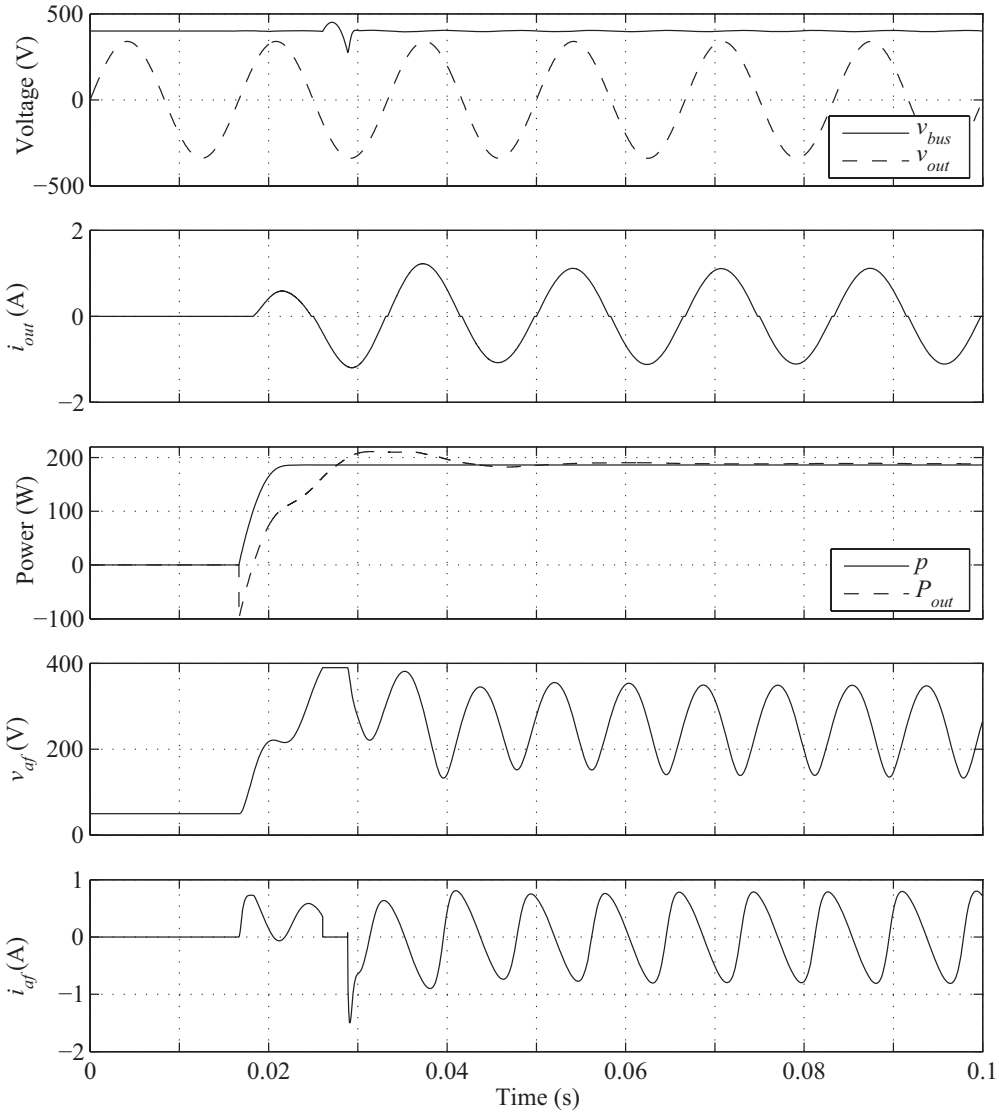


Fig. 4.26 Simulation waveforms of average-value model of ac PV module with active filter

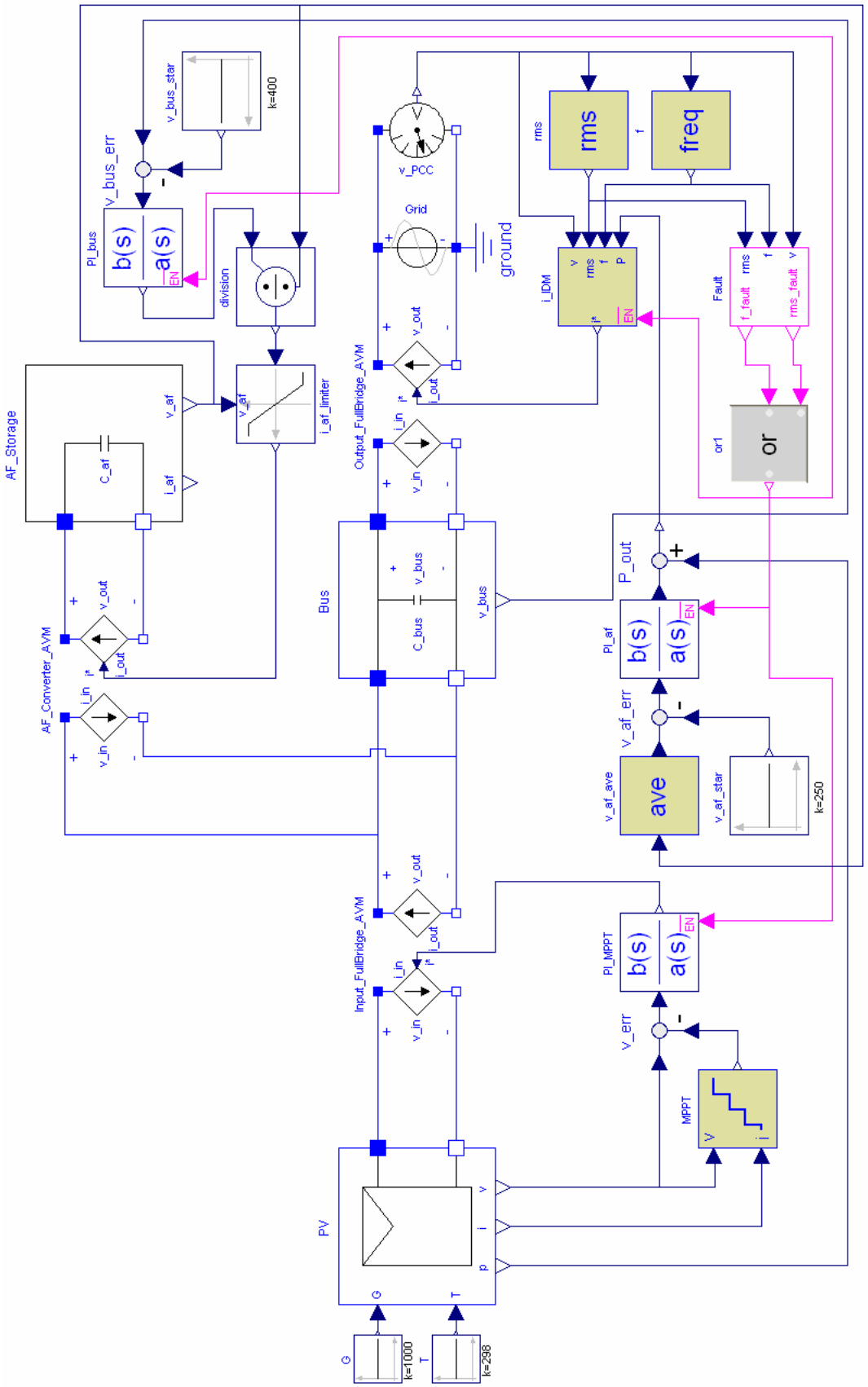


Fig. 4.27 Average-value model of ac PV module with active filter

Using the same insolation profile as in Section 4.2.3 and the AVM setup in Fig. 4.27, the transient response of the ac PV module with active filter can be investigated under rapidly decreasing and increasing insolation. The outcome of the simulation is shown in Fig. 4.28. As can be observed, all the waveforms are well behaved with the MPPT algorithm continuously tracking the MPP of the PV module, v_{bus} tracking v_{bus}*, and the average of v_{af} staying at v_{af}*. As expected, the amplitude of v_{af} decreases when less double-frequency energy is needed at low power levels.

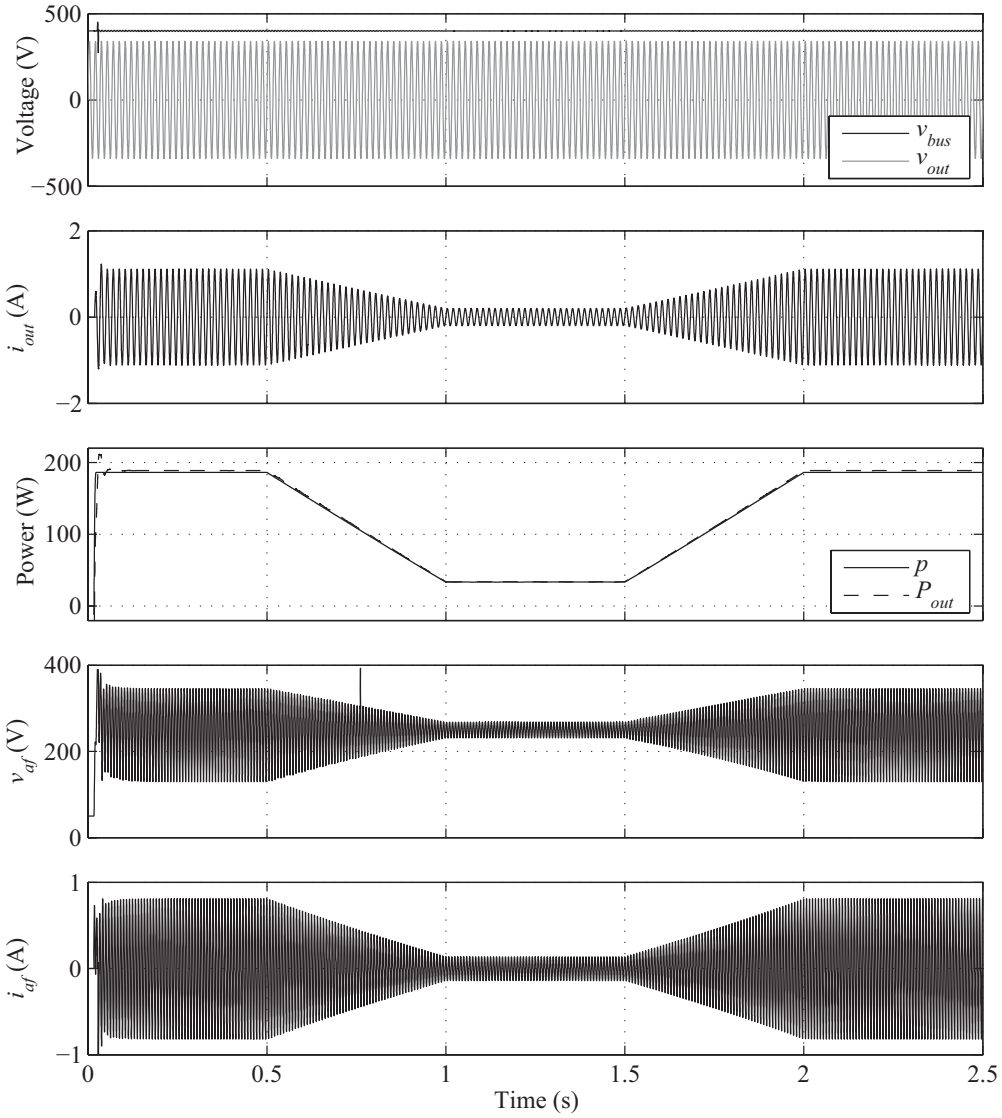


Fig. 4.28 Waveforms under rapid insolation changes for ac PV module with active filter

5 MULTI-INVERTER SYSTEM

5.1 Overview

Photovoltaic (PV) systems with multiple grid-tied inverters and the interaction among the inverters and the utility grid have not been fully explored. According to [41], the "multiple inverter case definitely warrants further investigation" and the "effect of multiple inverters on some islanding protection schemes is not completely clear." While the authors in [57] have tested up to four 5.5-kW inverters in parallel and shown that they meet the 2-s islanding detection time limit [42], all four inverters used the same islanding detection method (IDM). In [58], the authors derived equations to study the stability of a four-inverter PV system, but all the inverters were identical and the control system employed was not apparent. Reference [59] studied the effects and interaction of inverters with different IDMs, but only two inverters were used in parallel. On the other hand, the authors in [60] and [61] have assessed the waveform harmonic distortion in a five-inverter system and large-scale PV installations with multiple grid-connected inverters, respectively—in both cases, all the inverters were from the same manufacturer and other aspects of the system were not considered. Up to four ac PV modules were tested in [62] and, in some cases, islanding was shown to remain undetected. However, no detail is given on either the ac PV modules or the IDMs that were used.

This chapter will investigate multi-inverter systems by focusing on residential-scale PV systems with ac PV modules. At present, most residential PV systems consist of one or two central or string inverter(s). When there are two inverters, they are usually identical and wired in a master-slave configuration for a split-phase system. In such systems, concerns about violating the requirements of the IEEE 1547 standard [42], as discussed in Chapter 3, are probably minimal. However, with the introduction of ac PV modules on the market, forthcoming residential PV systems will more likely have more than two ac PV modules, although a single ac PV module is possible for a much lower power scale. Furthermore, there might be systems with a mixture of ac PV modules from different manufacturers—the likelihood of the microinverters and control systems within these modules being identical will be very low. Consequently, it is essential to better understand the behavior of such systems and their compliance with the standards.

A PV system with n ac PV modules, not necessarily identical, connected in parallel is shown in Fig. 5.1. As in Chapter 3, a resonant RLC load may be placed in parallel with the PV system. As per IEEE 1547, if the frequency f of the voltage v_{PCC} at the point of common coupling (PCC) and/or its root-mean-square (rms) value V_{PCC} are outside of the normal ranges (see Tables 3.1 and 3.2), the PV system shall cease to supply power within the allowable clearing times. Moreover, when an island is created when the switch opens due to a fault on the grid or a scheduled maintenance, the PV system has to shut down within two seconds of the formation of the island, even if its output power perfectly matches the power consumption of the local load. The PV system shutting down implies that every single ac PV module has to shut down, such that the total output current i_{PV} goes to zero.

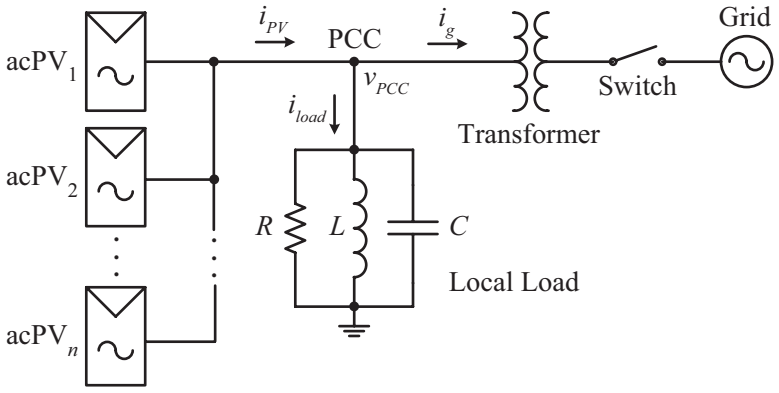


Fig. 5.1 PV system with multiple ac PV modules

Hereinafter, a PV system of up to 10 ac PV modules (i.e. n = 10) will be considered. Each ac PV module can be modeled as one of the ac PV modules analyzed in Chapter 4—either with passive filter (PF) or active filter (AF), each of which can include one of the three IDMs discussed in Chapter 3, namely active frequency drift (AFD), slip mode frequency shift (SMS), and Sandia frequency shift (SFS). In other words, there are six possible ac PV modules, whose blocks, created in Dymola, are shown in Fig. 5.2. These blocks are made up of the complete average-value model (AVM) shown in either Fig. 4.12 or Fig. 4.27. The AVMs are chosen over the switch-level models because of the substantial gain in simulation time, as reported in Chapter 4, and also because simulating up to10 ac PV modules simultaneously is computationally intensive. As in the previous chapters, the modules are rated at 185 kW, resulting in a system of up to 1.85 kW, which is a good representation of a typical residential setup.

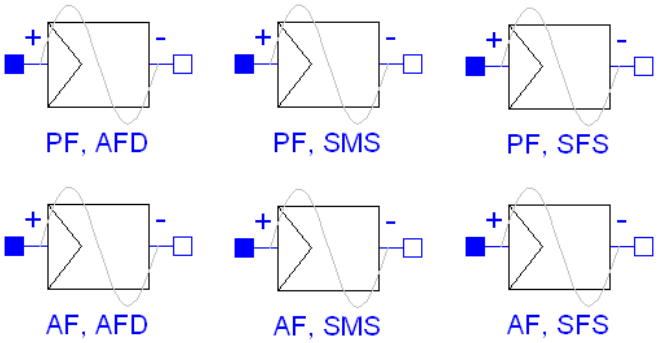


Fig. 5.2 Dymola ac PV module blocks

Figure 5.3 shows the Dymola setup to simulate the PV system. The ac PV modules can be chosen to be any or a combination of those in Fig. 5.2. They can also be removed to construct a system with fewer modules. The insolation G and temperature T can be controlled independently for each module. In every case that will be investigated in the subsequent subsections, the local RLC load will be designed to have a resonant frequency f_0 of 60 Hz and a quality factor Q_f of 1.0, as per the IEEE 1547.1 standard [50], and to always consume the total power that can be generated by the PV system. This ensures the worst case scenario, mainly under islanding conditions. The response of the system under abnormal grid conditions will be covered in Section 5.2. The ability of the system to detect islanding with ac PV modules using the same IDM or a combination of two IDMs will be looked at in Sections 5.3 and 5.4, respectively. Section 5.5 will show how several ac PV modules in parallel can improve the quality of the power delivered.

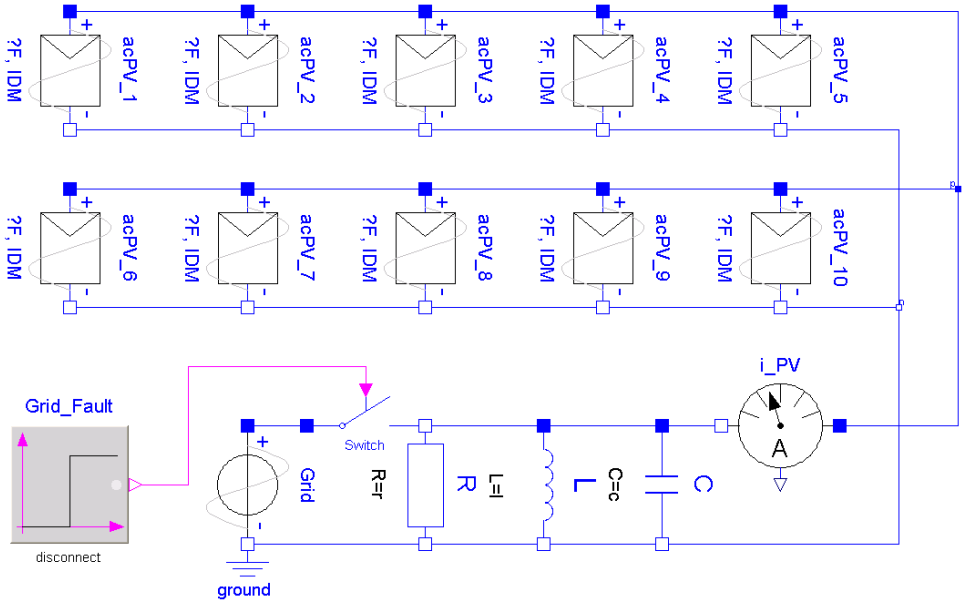


Fig. 5.3 Dymola setup to simulate PV system with multiple ac PV modules

5.2 Abnormal Grid Conditions

With the setup in Fig. 5.3 having 10 ac PV modules with PF and AFD, after a simulation time of 0.05 s, the rms value V_g of grid voltage v_g is set to start deviating linearly over 0.05 s from its nominal of 240 V to 86% of the nominal (i.e. 206.4 V), which is lower than the 88% limit (i.e. 211.2 V). This is illustrated in Fig. 5.4, where the change in amplitude can also be noted in v_{PCC}, which essentially equals v_g. Since, as in Chapter 3, every ac PV module is set to wait three line cycles after an abnormal condition is detected before shutting down, the fault signal takes that long to go high and i_{PV} to zero. Comparable behaviors were observed when V_g exceeds the upper limit and when other combinations of IDMs were used, indicating that it should not be a problem for a multi-inverter PV system to detect abnormal grid voltages, even in the presence of a local resonant load with perfect power match.

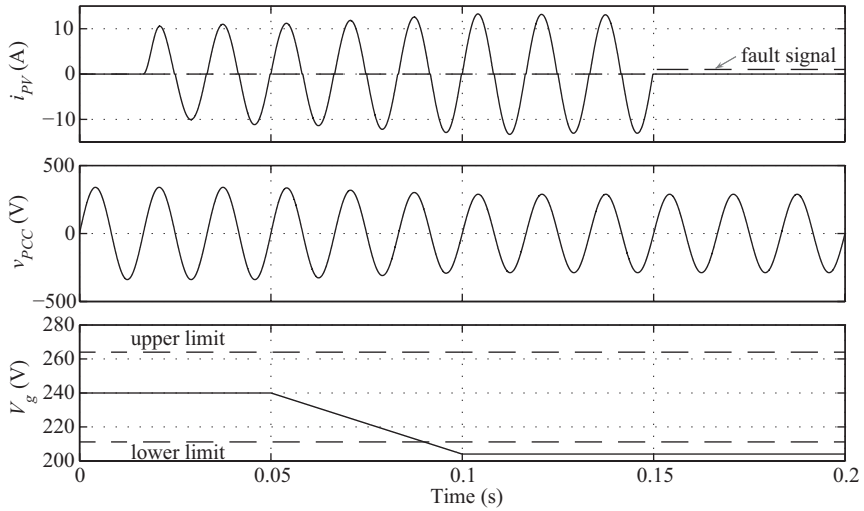


Fig. 5.4 Shutdown of a PV system with 10 ac PV modules due to abnormal grid voltage

On the other hand, while V_g is kept constant at its nominal of 240 V, the grid frequency f_g is controlled to drift out of the normal range. As shown in Fig. 5.5, starting at a 60-Hz nominal at 0.05 s, f_g decreases linearly over 0.05 s to 59.1 Hz—this is lower than the 59.3-Hz limit. In this case, due to the interaction with the local RLC load, the ac PV modules detect the abnormal frequency within a shorter time and shut down properly, as can be seen by the fault signal and i_{PV}. Several other simulations with f_g violating the upper limit and the ac PV modules using different permutations of IDMs confirmed that detecting abnormal grid frequencies is not an issue for a multi-inverter PV system.

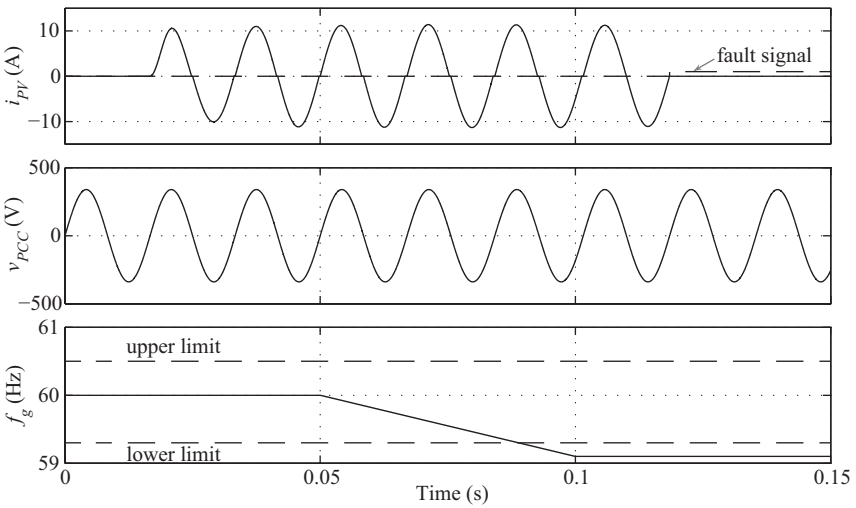


Fig. 5.5 Shutdown of a PV system with 10 ac PV modules due to abnormal grid frequency

5.3 Islanding Detection in a PV System with Identical IDMs

Detecting islanding conditions has been a bigger concern than detecting abnormal grid conditions in multi-inverter PV systems. As an example of the islanding detection performance of a PV system that consists of ac PV modules with identical IDMs, the ac PV modules in the Fig. 5.3 setup were configured to be of the PF type with AFD. The system was simulated with G and T set to 1000 W/m^2 and 25 °C, respectively, for all the modules. The grid is disconnected at 0.07083 s to form an island. As can be seen in Fig. 5.6, the frequency f at the PCC drifts out of the normal range and is detected by all the modules at 0.13214 s, when the fault signal goes high and i_{PV} to zero. Therefore, in this case, the islanding detection time is 61.3 ms.

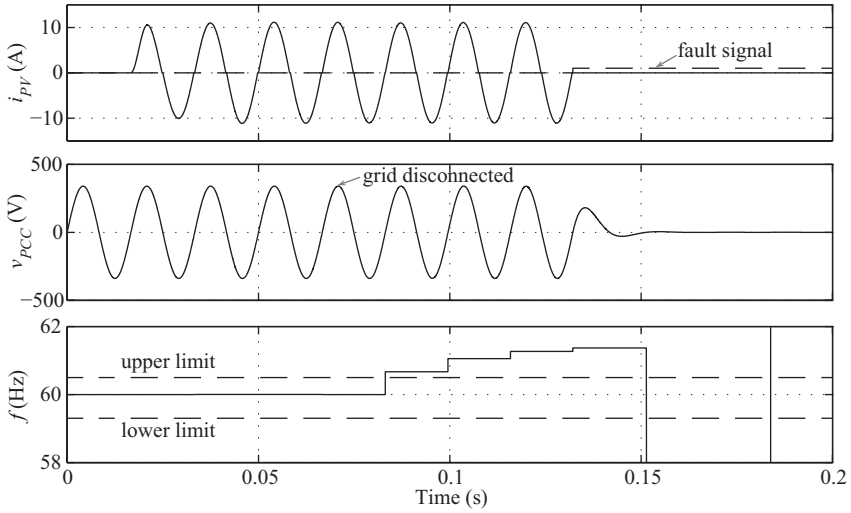


Fig. 5.6 Islanding detection in a PV system of 10 ac PV modules with AFD

The same experiment was run with all the modules being of AF type, but no difference could be noted. This is due to the fact that the way the double-frequency energy is managed within the microinverter does not affect its interaction with the utility grid. Therefore, the observations made hereinafter apply to ac PV modules of both PF and AF types. Table 5.1 shows the islanding detection times for PV systems with an increasing number of ac PV modules, using each of the three IDMs, at 1000 W/m^2 and 25 °C. It is interesting to note that increasing the number of ac PV modules does not change the detection time when AFD or SFS is used. On the other hand, not only is the detection time longer when using SMS, but also no particular trend can be observed. In AFD and SFS, deviation of *f* from the nominal during islanding depends on the current command dead time (see Fig. 3.7), which is well controlled. However, in SMS, there is no control on the trajectory of *f* from the unstable operating point to one of the stable operating points (see Fig. 3.9), explaining the randomness in detection time.

Table 5.1 Islanding detection time versus number of ac PV modules, at 1000 W/m^2 and 25 °C

	Islanding Detection Time (ms)		
Number of ac PV modules	**AFD**	**SMS**	**SFS**
1	61.3	310.5	57.9
2	61.3	393.9	57.9
3	61.3	344.3	57.9
4	61.3	344.4	57.9
5	61.3	344.5	57.9
6	61.3	344.2	57.9
7	61.3	464.7	57.9
8	61.3	344.3	57.9
9	61.3	310.9	57.9
10	61.3	414.8	57.9

To understand whether the time taken to detect an island is affected by the amount of power being processed by the ac PV modules, the setup in Fig. 5.3 was simulated while varying the insolation level, assuming that all the modules are subjected to the same insolation. Table 5.2 shows the recorded times as the insolation decreases. Once again, the detection times for AFD and SFS remain unchanged and match those in Table 5.1, whereas the detection time for SFS is still random and has no correlation with those in Table 5.1. This suggests that manufacturers of inverters with SMS should test their inverters under all possible conditions to make sure that the regulation is never violated.

Table 5.2 Islanding detection time versus insolation, with 10 ac PV modules at 25 °C

	Islanding Detection Time (ms)		
Insolation (W/m^2)	**AFD**	**SMS**	**SFS**
1000	61.3	414.8	57.9
900	61.3	398.1	57.9
800	61.3	443.8	57.9
700	61.3	414.7	57.9
600	61.3	448.4	57.9
500	61.3	365.1	57.9
400	61.3	348.5	57.9
300	61.3	327.6	57.9
200	61.3	364.5	57.9
100	61.3	348.1	57.9

5.4 Islanding Detection in a PV System with Mixed IDMs

The purpose of this section is to analyze how mixing ac PV modules with two different IDMs affects the islanding detection time of a PV system that consists of up to 10 ac PV modules.

5.4.1 PV System with AFD and SMS

The system in Fig. 5.3 was simulated with an increasing number of ac PV modules, each of which can use either AFD or SMS. The islanding detection time for every combination is given in Table 5.3. From this table, two observations can be made: (1) adding an ac PV module with AFD to a group of ac PV modules with SMS considerably decreases the detection time and (2) the more ac PV modules with SMS added to ac PV

Table 5.3 Islanding detection time for different combinations of ac PV modules with AFD and SMS

		Islanding Detection Time (ms)										
Number of ac PV modules with SMS	**10**	414.8										
	9	310.9	127.8									
	8	344.3	127.7	110.9								
	7	464.7	127.5	110.7	94.4							
	6	344.2	127.3	94.5	94.2	94.0						
	5	344.5	111.1	94.4	94.1	77.9	77.8					
	4	344.4	110.9	94.2	77.9	77.8	77.7	77.7				
	3	344.3	94.5	94.1	77.8	77.7	77.6	77.6	77.6			
	2	393.9	94.2	77.8	77.7	77.6	77.6	77.6	77.5	77.6		
	1	310.5	77.8	77.6	77.6	77.5	61.3	61.3	61.3	61.3	61.3	
	0		61.3	61.3	61.3	61.3	61.3	61.3	61.3	61.3	61.3	61.3
		0	**1**	**2**	**3**	**4**	**5**	**6**	**7**	**8**	**9**	**10**
		Number of ac PV modules with AFD										

modules with AFD, the longer the detection time. Figure 5.7 shows graphical representations of the data given in Table 5.3. Note that the islanding detection times for PV systems with SMS alone have been omitted from Fig. 5.7 to prevent the corresponding lengthier times from skewing the visual aspect of the bars.

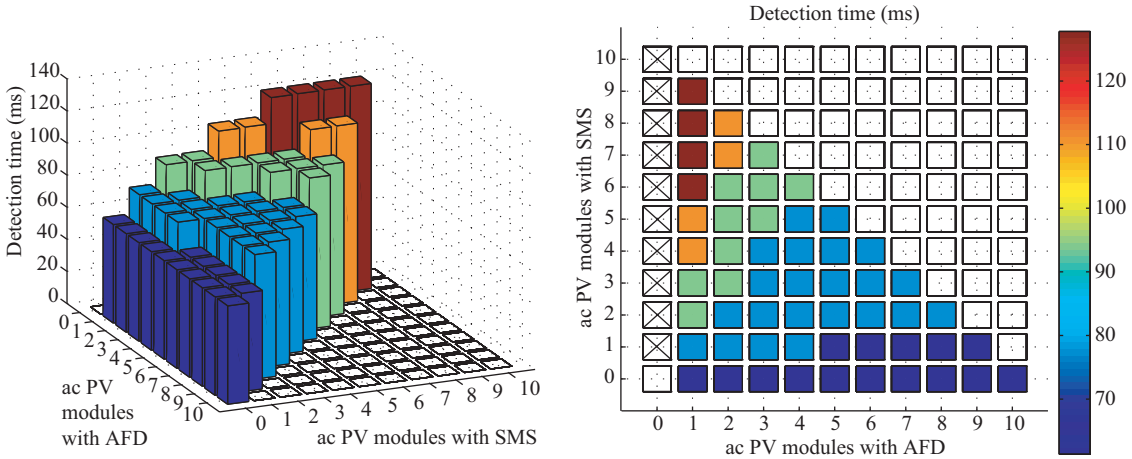


Fig. 5.7 Islanding detection time for different combinations of ac PV modules with AFD and SMS

If the islanding detection time of a PV system of ac PV modules with AFD has an islanding detection time—which is independent of the number of ac PV modules and insolation in the previous section as shown above—that is close to the 2-s time limit by design, then introducing ac PV module(s) with SMS into the system might be possibly violate this time limit. Therefore, a fully compliant PV system can be made to violate the regulations.

5.4.2 PV System with AFD and SFS

The islanding detection times of up to 10 ac PV modules using either AFD or SFS are given in Table 5.4 and graphically represented in Fig. 5.8. Since the detection times of both IDMs are well controlled, there is not a big variation throughout the table. Having more ac PV modules with AFD in the system brings a minimal increase in the islanding detection time—not a significant change to bring a PV system out of regulatory compliance. In other words, mixing ac PV modules using AFD and SFS should not represent any risk of having a PV system continuing to power an island for more than the allowed time limit of 2 s.

Table 5.4 Islanding detection time for different combinations of ac PV modules with AFD and SFS

Number of ac PV modules with SFS	Islanding Detection Time (ms)										
10	57.9										
9	57.9	58.5									
8	57.9	58.5	59.0								
7	57.9	58.6	59.1	59.4							
6	57.9	58.7	59.2	59.6	59.8						
5	57.9	58.8	59.4	59.7	60.0	60.2					
4	57.9	59.0	59.6	59.9	60.2	60.3	60.5				
3	57.9	59.2	59.8	60.2	60.4	60.5	60.6	60.7			
2	57.9	59.6	60.2	60.5	60.6	60.8	60.8	60.9	60.9		
1	57.9	60.2	60.6	60.8	60.9	61.0	61.1	61.1	61.1	61.1	
0		61.3	61.3	61.3	61.3	61.3	61.3	61.3	61.3	61.3	61.3
	0	**1**	**2**	**3**	**4**	**5**	**6**	**7**	**8**	**9**	**10**
	Number of ac PV modules with AFD										

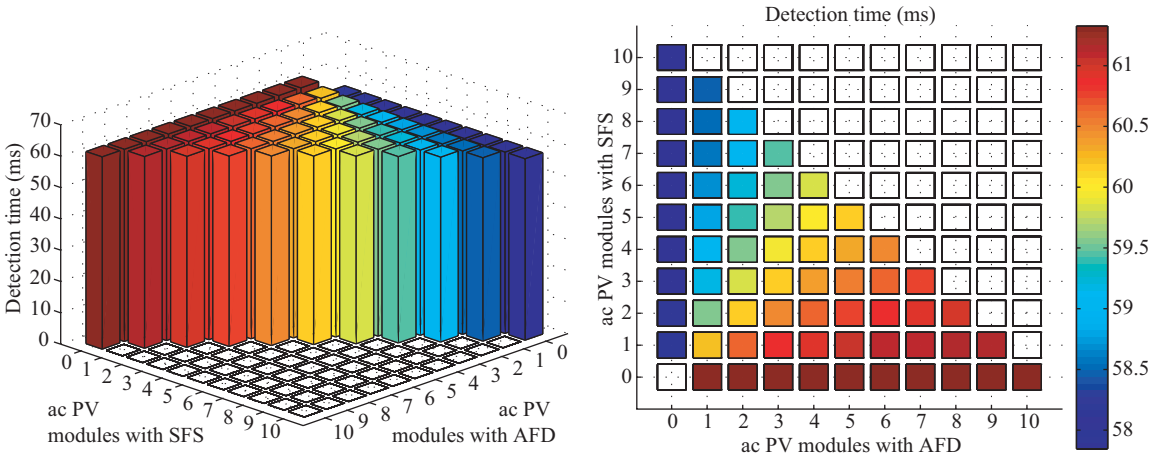


Fig. 5.8 Islanding detection time for different combinations of ac PV modules with AFD and SFS

5.4.3 PV System with SFS and SMS

A PV system consisting of ac PV modules with either SFS or SMS was simulated to detect an island after the amount of time given in Table 5.5 for every possible combination of up to 10 modules. Figure 5.9 illustrates the times for visual comparison. The similarity between Fig. 5.9 and Fig. 5.7 is obvious—here also, adding ac PV modules with SMS lengthens the islanding detection times. The only difference is that the islanding detection times show a slight improvement over the AFD IDM, thanks to the accelerating factor of the SFS IDM. All the above data clearly suggest that, unlike adding ac PV modules with AFD and/or SFS to a PV system, those with SMS demand that the system be tested to ensure compliance with the islanding detection requirement.

Table 5.5 Islanding detection time for different combinations of ac PV modules with SFS and SMS

Number of ac PV modules with SMS	Islanding Detection Time (ms)										
10	414.8										
9	310.9	127.4									
8	344.3	127.2	110.1								
7	464.7	127.0	94.1	93.4							
6	344.2	110.9	93.9	93.1	77.1						
5	344.5	110.5	93.6	77.3	76.8	76.4					
4	344.4	110.1	93.1	76.9	76.4	76.0	75.6				
3	344.3	93.9	77.1	76.4	75.9	75.4	75.1	74.8			
2	393.9	93.1	76.4	75.6	75.1	74.6	74.2	73.9	73.7		
1	310.5	76.4	75.1	74.3	73.7	59.3	59.1	58.9	58.8	58.8	
0		57.9	57.9	57.9	57.9	57.9	57.9	57.9	57.9	57.9	57.9
	0	**1**	**2**	**3**	**4**	**5**	**6**	**7**	**8**	**9**	**10**
	Number of ac PV modules with SFS										

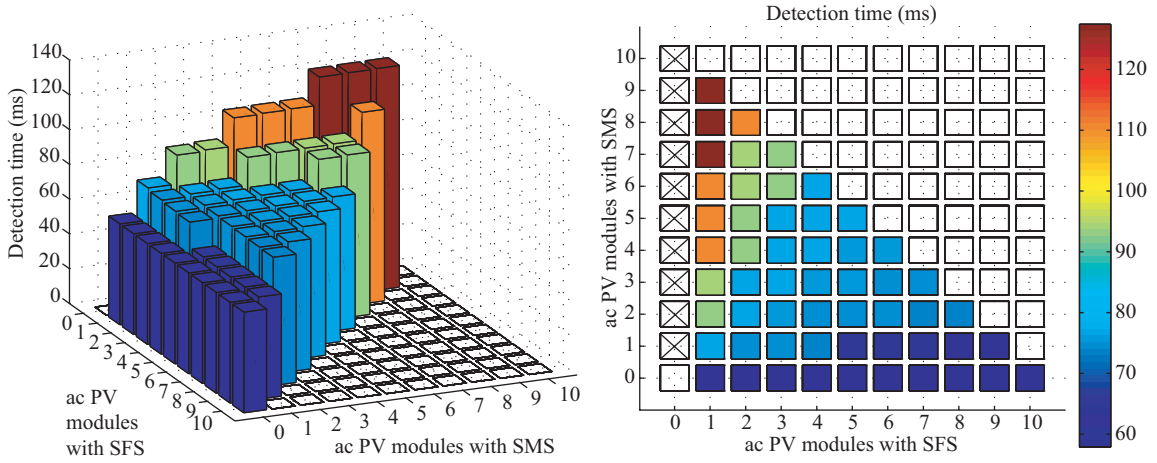


Fig. 5.9 Islanding detection time for different combinations of ac PV modules with SFS and SMS

5.5 Power Quality

Using AVMs to simulate the multi-inverter system does not capture the switching behavior of the system. Consequently, the harmonic content of the PV system output current i_{PV} cannot be analyzed. However, a simple simulation can be devised to show that the harmonic content of i_{PV} may be improved by having multiple ac PV modules in parallel and using pulse-width modulation (PWM) to generate the switching signals of their output full-bridge converters.

In this simple simulation, all the ac PV modules are assumed to use an output current command i_{out}* similar to the SMS one in Fig. 3.18, which is essentially sinusoidal, unlike the intricate AFD current command in Fig. 3.14. This allows the switching signals to be

generated by PWM instead of hysteresis. A duty ratio command d can be produced from i_{out}* and i_{out} using an average current mode (ACM) control similar to that used in the input stage of the microinverter. The PWM signal can be obtained by comparing d to a triangular carrier signal tri, such that

$$\text{PWM} = d > tri\ . \tag{5.1}$$

The switching signals are then given by

$$\begin{aligned} q_{o11} &= q_{o22} = \text{PWM} \\ q_{o12} &= q_{o21} = \overline{\text{PWM}}\ . \end{aligned} \tag{5.2}$$

Figure 5.10 shows these different signals with a carrier signal having a frequency of 42 kHz, which is the mean of the frequency range of 18 to 65 kHz reported for the hysteresis control in Section 3.6. As can be seen, the switching frequency of the switches in the output full-bridge converter is the same as the carrier frequency.

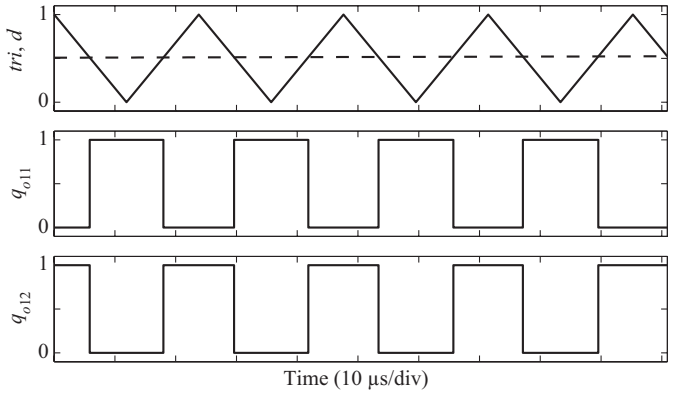


Fig. 5.10 PWM switching signals generation for the output full-bridge converter

Consider a PV system with four ac PV modules (i.e., $n = 4$) with carrier signals tri_1 through tri_4, respectively. If all the ac PV modules turn on and start processing power at the same time, with all of them having their carrier signals perfectly synchronized (i.e. $tri_1 = tri_2 = tri_3 = tri_4$), the total resulting current i_{PV} will look like the waveform shown in Fig. 5.11. The harmonics of i_{PV} around the switching frequency are shown in Fig. 5.12 and clearly exceed the IEEE limit of 0.3%. At the lower frequencies, only the fundamental is present, as in Fig. 3.19. If all the harmonics are taken into consideration, the THD is computed to be about 8.2% from the MATLAB code given in Appendix A. It is worth noting that, in this case, the harmonic content would be exactly the same for the output current of one of the ac PV modules.

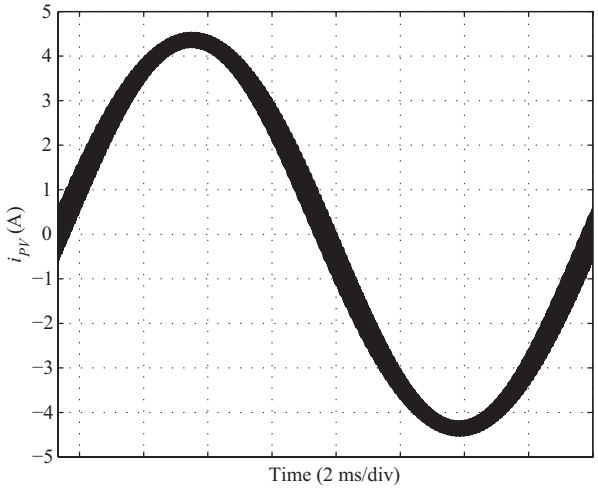


Fig. 5.11 Current i_{PV} with synchronized carrier signals

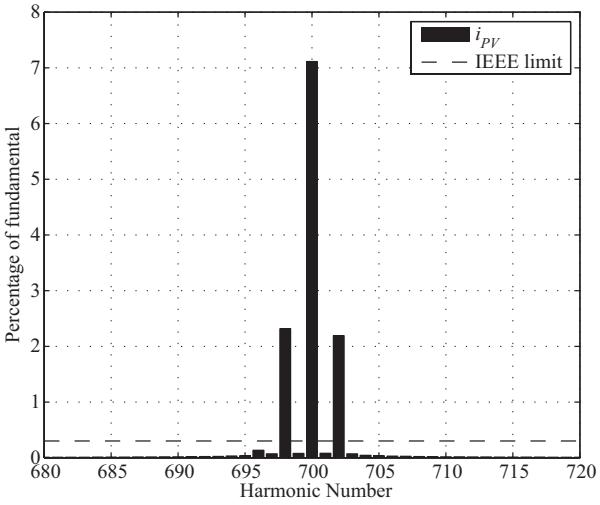


Fig. 5.12 Harmonics around switching frequency with synchronized carrier signals

However, in a real PV system, it is unlikely that all ac PV modules will turn on at the same time and even more unlikely that their carrier signals will be perfectly synchronized. In the isolated case where the four ac PV modules have their carrier signals 90° out of phase from each other, as shown in Fig. 5.13, Fig. 5.14 shows the resulting current i_{PV}. When compared to the waveform in Fig. 5.11, the difference is evident—the magnitude of the switching ripple has been considerably reduced. Figure 5.15 confirms that the harmonics around the switching frequency have been significantly attenuated, when compared to Fig. 5.12, and now do not violate the IEEE limit. In this case, with all the harmonics included, the THD is only 0.6%. Moreover, probable variation in output power from PV module to PV module may further add to this harmonic cancellation

behavior. Therefore, with statistical independence among ac PV modules, it is safe and realistic to assume that a PV system with a higher number of the ac PV modules will output a relatively clean current with very low THD. Interestingly, this current ripple canceling effect is very similar to that in multiphase dc-dc converters like in [63], wherein the PWM carriers are not randomly out of phase, but enforced to be so.

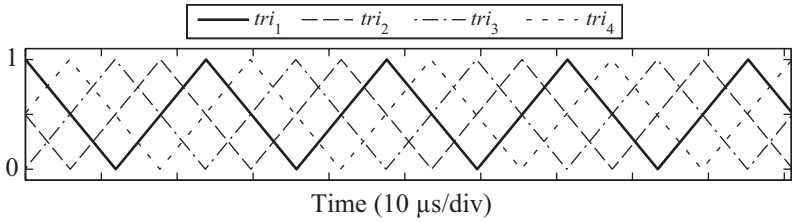


Fig. 5.13 Carrier signals 90° out of phase from each other

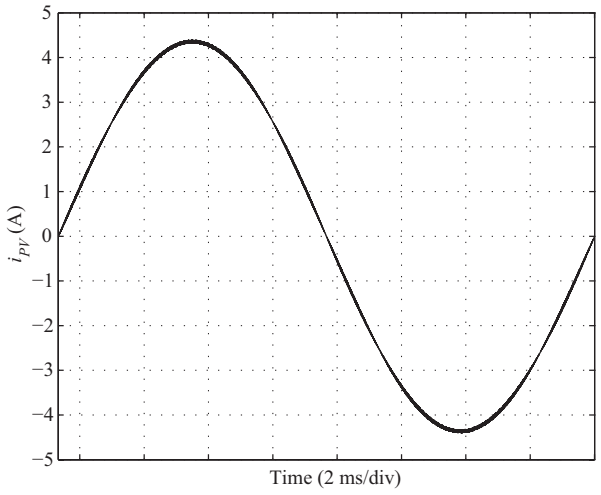


Fig. 5.14 Current i_{PV} with unsynchronized carrier signals

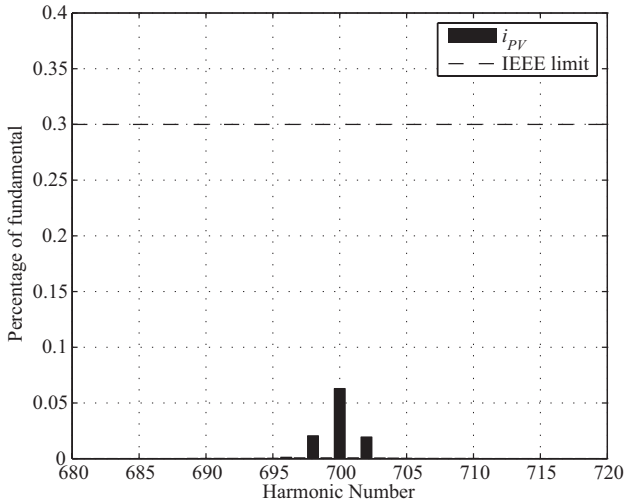


Fig. 5.15 Harmonics around switching frequency with unsynchronized carrier signals

6 CONCLUSION

A review of the electricity market in the U.S. over the past few years showed that electricity production from photovoltaic (PV) sources represents a very small fraction of the nation's total generation capacity. This is mostly due to the fact that the cost of electricity from PV systems is too high to compete with conventional energy sources. Only if PV electricity cost can reach a competitive level, that is grid parity, will PV systems be widely adopted. Regardless of the kind of grid parity—spot market, peak, retail, or cost parity—it is fundamental that the overall cost of PV systems goes down. Contrary to common belief, lowering PV module cost, which represents less than half of the total system cost, is not sufficient.

Alternating-current (ac) PV modules, on the other hand, can bring down the costs of the remaining sectors constituting a PV system, by providing simpler, faster, and less expensive installation and eliminating the need to replace inverters once or twice over the lifetime of the system with more reliable smaller inverters, usually called microinverters. Moreover, compared to systems with central or string inverters, those with ac PV modules are more reliable and provide higher energy yield. However, with several microinverters running at the same time in a PV system, as opposed to only one or two string or central inverter(s), it is particularly important to understand the behavior and dynamics of the system and its compliance with regulatory codes and standards when interconnected with the utility grid. This was done in this dissertation by modeling a complete ac PV module, with all the controls required for maximum energy harvest and code compliance, and simulating and analyzing PV systems with up to 10 such ac PV module models under different operating and atmospheric conditions.

The ac PV module model consisted in modeling the PV module and the microinverter and developing the controls for the microinverter to track the maximum power point (MPP) of the PV module, manage energy flow, and respond to abnormal grid conditions and islanding. Modeling a real PV module is not straightforward because of several parameters generally missing from its datasheet. A method of extracting these parameters using corner points of a standard characteristic PV module curve was reviewed. The current-voltage curves outputted by the resulting model for a particular module were shown to correlate very well with the curves given in its datasheet.

The choice of circuit topology for the microinverter was important because it had to be representative of a physical microinverter that should be not only reliable to match the lifetime of the PV module, but also compact and light to not compromise the mechanical integrity of the module. A cycloconverter-type inverter initially seemed to have the right properties, but its relatively low switching frequency, limited by its thyristors, and its need for excessively big passive filters to meet regulations rendered it unsuitable for an ac PV module. Therefore, a microinverter, which allows the use of MOSFETs as switches, higher switching frequency, and smaller passive components, was chosen.

The selected microinverter topology consists of an isolated boost input connected to a conventional full-bridge converter output stage through a direct-current (dc) bus capacitor. The purpose of the input stage is to continuously maximize the energy yield from the PV module and boost the PV module voltage for the bus capacitor. An optimized Perturb and Observe (P&O) maximum power point tracking (MPPT) algorithm, named *dP*-P&O, was analyzed, modeled, and simulated with a switch-level model of the input stage. It was shown that having the *dP*-P&O block output a voltage command, from which a current and duty ratio command were consecutively generated, provided fast and robust MPPT, even under rapid insolation variations. An average-value model (AVM) was also developed to replace the switch-level model of the input stage and proved to preserve all the dynamics of the system, except the switching ripple. More importantly, the AVM drastically reduced simulation times.

The output stage of the microinverter interfaces with the utility grid and thus, under abnormal grid conditions and islanding, has to respond according to well-defined codes and standards. Detecting islanding conditions was shown to be less trivial than detecting abnormal grid voltages and frequencies. Three different islanding detection methods (IDMs)—active frequency drift (AFD), slip mode frequency shift (SMS), and Sandia frequency shift (SFS)—were reviewed and their theoretical nondetection zones (NDZs) were presented. The validity of these NDZs was confirmed, in the presence of different local resonant loads, through simulations of the output stage, with both its switch-level model and AVM. For each IDM, the harmonic content of the current injected into the grid was shown to meet the harmonic limits and total harmonic distortion (THD) only if the first 40 harmonics are considered, as prescribed by the standards.

The PV module combined with the input and output stages forms an ac PV module. When connected to the grid, the ac PV module experiences energy flowing to and from the grid at double the grid frequency. It was shown that there are two ways to manage this double-frequency energy flow: by using either a passive filter or an active filter. The passive filter approach is easier to implement by simply using the bus capacitor to store the energy, but results in more capacitance. The output stage regulates the bus voltage in this case. The active filter technique uses less capacitance, but requires additional circuitry and control to divert the energy from the bus. The active filter regulates the bus voltage while the output stage regulates the active filter capacitor voltage. In both cases, the control topologies were analyzed and shown to be stable with adequate margins for proper tracking. Once again, using AVMs for the input, output, and even the active filter resulted in significant reduction in simulation time.

AVMs for ac PV modules, using either passive or active filter, allow for the simulation of the PV systems using numerous ac PV modules under different conditions without being excessively computationally intensive. In this dissertation, PV systems having up to 10 ac PV modules—representative of typical residential PV systems—were simulated. The ability of all ac PV modules to detect abnormal grid voltages and frequencies and shut down within the prescribed time limit was confirmed, regardless of the number and type of modules in the system or the kind of IDM used. In systems with ac PV modules using identical IDM, it was observed that neither the number of ac PV modules nor varying insolation affects the islanding detection time when AFD or SFS is used. However, under similar settings, the detection times with SMS are random. This is explained by the fact that the current command dead time in AFD or SFS is well controlled, while there is no control on the trajectory of the frequency from the unstable operating point to one of the stable operating points in the SMS formulation. On the other hand, simulations of PV systems with mixed IDMs showed that the more ac PV modules with SMS are added to systems using AFD or SFS, the longer the detection times. An initially fully compliant PV system can thus be made to violate the regulations. Interestingly, for ac PV modules using pulse-width modulation, the statistical independence among the modules was shown to significantly improve the THD of the current delivered to the grid, thanks to the harmonic cancellation behavior.

6.1 Future Work

While numerous interesting observations have been made via theoretical derivations and simulation results throughout this dissertation, they have to be compared with and validated against real hardware, both at the microinverter level and the PV system level. Therefore, it is necessary to implement the proposed microinverter in hardware. Careful attention has to be paid to component selection to ensure reliability, robustness, and compactness, as discussed previously. Mechanical requirements of attaching the microinverter to a PV module and interconnecting the ac PV modules will also have to be considered.

While a handful of control techniques have been introduced, reviewed, analyzed, and tested herein, the microinverter is definitely not limited to these. There are other MPPT algorithms, IDMs, and double-frequency energy management controls that might be as effective or even better. They should be incorporated in the models created for this dissertation and investigated in a fashion similar to that presented in the preceding chapters. It will be interesting to see how energy harvest from the PV module is affected by different MPPT techniques and whether it is possible to have an IDM without an NDZ.

Conversely, the control techniques covered in this dissertation are not limited to the proposed microinverter. As mentioned in the introduction, there are several different microinverter topologies. It will be a good experiment to see how easily the controls can be adapted to other topologies and which topology can result in the smallest, cheapest, and most efficient microinverter. More effort should also be put into further developing the cycloconverter-type inverter that was initially proposed for this work—faster thyristors are plausible with continuous improvement in the semiconductor field and it remains to be seen whether changes in the state machine control can help.

Although this work has focused on PV systems of residential type, it is also important to understand the behaviors and dynamics of larger scale systems with ac PV modules. If ac PV modules are to revolutionize the PV electricity market, they will need to be used in utility-scale systems. The question is whether there is a limit to the number of ac PV modules that can be used in a single system and whether there should be other codes and regulations that apply to such systems.

APPENDIX A CODES

A.1 MATLAB Code for PV Data Extraction

```
% Script to solve for R_s, R_sh, and n using PV module datasheet
% parameters.
% NOTE: this only works for PV cells in series! If cells or strings of
% cells are in parallel, consider each string separately.

% Trishan Esram
% 11/30/2008

clear all; close all; clc

% Constants:
k = 1.38065e-23;    % Boltzmann constant in J/K
q = 1.602e-19;      % electron charge in C
T_stc = 298;        % temperature at STC in K
V_t = k*T_stc/q;    % diode junction thermal voltage in V

% Parameters for BP 7185:
V_oc = 44.8;    % open-circuit voltage at STC in V
I_sc = 5.5;     % short-circuit current at STC in A
V_mpp = 36.5;   % voltage at MPP at STC in V
I_mpp = 5.1;    % current at MPP at STC in A
N = 72;         % number of cells

% Extract parameters:
% x(1) = R_s, x(2) = R_sh, x(3) = n
x=fsolve(@(x)PV_parameters_func(x,V_oc,I_sc,V_mpp,I_mpp,m,V_t),...
[0.5;1000;1]);

% Solutions:
R_s = x(1)  % PV module series resistance in ohms
R_sh = x(2) % PV module shunt resistance in ohms
n = x(3)    % emission coefficient (diode ideality factor)

function F = PV_parameters_func(x,V_oc,I_sc,V_mpp,I_mpp,N,V_t)
% Script containing the equations that need to be solved to find R_s,
% R_sh, and n using PV module datasheet parameters

% Trishan Esram
% 11/30/2008

% x(1) = R_s, x(2) = R_sh, x(3) = n
F = [-I_mpp + I_sc - (V_mpp + I_mpp*x(1) - I_sc*x(1))/x(2) - (I_sc -...
    (V_oc - I_sc*x(1))/x(2))*exp((V_mpp + I_mpp*x(1) - V_oc)/(x(3)*...
    N*V_t));
    I_mpp + V_mpp*(-((I_sc*x(2) - V_oc + I_sc*x(1))/(x(3)*N*V_t*...
    x(2)))*exp((V_mpp + I_mpp*x(1) - V_oc)/(x(3)*N*V_t)) - 1/x(2))...
    /(1 + x(1)*((I_sc*x(2) - V_oc + I_sc*x(1))/(x(3)*N*V_t*x(2)))...
    *exp((V_mpp + I_mpp*x(1) - V_oc)/(x(3)*N*V_t)) + x(1)/x(2));
    1/x(2) + (-((I_sc*x(2) - V_oc + I_sc*x(1))/(x(3)*N*V_t*x(2)))...
    *exp((I_sc*x(1) - V_oc)/(x(3)*N*V_t)) - 1/x(2))/(1 + x(1)*...
    ((I_sc*x(2) - V_oc + I_sc*x(1))/(x(3)*N*V_t*x(2)))*...
    exp((I_sc*x(1) - V_oc)/(x(3)*N*V_t)) + x(1)/x(2))];
```

A.2 Complete PV Module Model Modelica Code

```
model BP_BP_7185 "BP Solar BP 7185 module"
  // NOTE: Insolation AND temperature effects on current and voltage
  // and breakdown are included in this model.
  extends Modelica.Electrical.Analog.Interfaces.OnePort;

protected
  // Constants
  parameter Real T_STC(unit="K") = 298 "STC temperature";
  parameter Real G_STC(unit="W/m^2") = 1000 "STC insolation";
  parameter Real k(unit="J/K") = 1.38065e-23 "Boltzmann constant";
  parameter Real q(unit="C") = 1.602e-19 "electron charge";

  // Datasheet Parameters
  // V_oc(unit="V") = 44.8 "module open-circuit voltage at STC";
  // I_sc(unit="A") = 5.5 "module short-circuit current at STC";
  // V_mpp(unit="V") = 36.5 "module voltage at MPP at STC";
  // I_mpp(unit="A") = 5.1 "module current at MPP at STC";
  parameter Real k_i(unit="%/K") = 0.065
    "temperature coefficient of I_sc";
  parameter Real k_v(unit="V/K") = -0.16
    "temperature coefficient of V_oc";
  parameter Real N=72 "number of cells";

  // Extracted Parameters (using MATLAB)
  parameter Real n_d=1.4061 "diode quality (ideality) factor";
  parameter Real R_s(unit="ohm") = 0.2614 "module series resistance";
  parameter Real R_sh(unit="ohm") = 1474 "module shunt resistance";

  // Breakdown Parameters
  parameter Real a(unit="1/ohm") = 2.3e-3
    "fraction of ohmic current in avalanche breakdown";
  parameter Real V_br(unit="V") = -18 "breakdown voltage of one cell";
  parameter Real m=2 "exponent for avalanche breakdown";

  // Variables
  Real I(unit="A") "module current";
  Real V(unit="V") "module voltage";

  // Insolation/Temperature-Dependent Variables
  Real V_T(unit="V") "temperature-dependent junction thermal voltage";
  Real I_sc_T(unit="A") "temperature-dependent short-circuit current";
  Real V_oc_T(unit="V") "temperature-dependent open-circuit voltage";
  Real I_s_T(unit="A") "temperature-dependent dark saturation current";
  Real I_ph_T(unit="A")
    "temperature-dependent photo-generated current";

  Real I_sc_GT(unit="A")
    "insolation/temperature-dependent short-circuit current";
  Real V_oc_GT(unit="V")
    "insolation/temperature-dependent open-circuit voltage";
  Real I_ph_star(unit="A")
    "insolation/temperature-dependent photo-generated current";
  Real I_ph_GT(unit="A")
    "insolation/temperature-dependent photo-generated current";
  Real I_s_GT(unit="A")
```

```
    "insolation/temperature-dependent dark saturation current";

equation
  // Temperature dependence:
  V_T = k*T/q;
  I_sc_T = I_sc*(1 + k_i*(T - T_STC)/100);
  V_oc_T = V_oc + k_v*(T - T_STC);
  I_s_T = (I_sc_T - (V_oc_T - I_sc_T*R_s)/R_sh)*exp(-
    V_oc_T/(n_d*N*V_T));
  I_ph_T = I_s_T*exp(V_oc_T/(n_d*N*V_T)) + V_oc_T/R_sh;

  // Followed by insolation dependence:
  I_sc_GT = I_sc_T*G/G_STC;
  I_ph_star = I_ph_T*G/G_STC;
  V_oc_GT = ln((I_ph_star*R_sh - V_oc_GT)/(I_s_T*R_sh))*n_d*N*V_T;

  // Using all of the above:
  I_s_GT = (I_sc_GT - (V_oc_GT - I_sc_GT*R_s)/R_sh)*exp(-
    V_oc_GT/(n_d*N*V_T));
  I_ph_GT = I_s_GT*exp(V_oc_GT/(n_d*N*V_T)) + V_oc_GT/R_sh;

  // Module single-diode equation, including breakdown:
  I = I_ph_GT - I_s_GT*(exp((V + I*R_s)/(n_d*N*V_T)) - 1) - ((V +
    I*R_s)/R_sh)*(1 + a*(1 - (V + I*R_s)/(N*V_br))^(-m));

  // External pins assignment; current goes out of positive pin!
  i = -I;
  v = V;
end BP_BP_7185;
```

A.3 *dP*-P&O MPPT Algorithm Modelica Code

```
model dP_PandO "dP_PandO MPPT block"

  extends Modelica.Blocks.Interfaces.DiscreteBlockIcon;
  parameter Modelica.SIunits.Time samplePeriod=1/15e3;
  parameter Modelica.SIunits.Time startTime=0;
  parameter Integer nsamples=250
    "samples between updates (sampling frequency / update frequency)";
  parameter Integer half_nsamples=125
    "number samples half way between updates";
  parameter Real delta_coarse=0.25 "coarse perturbation step";
  parameter Real delta_fine=0.05 "fine perturbation step";
  parameter Real ThP(unit="W") = 0 "positive threshold for dP";
  parameter Real ThN(unit="W") = 0.5 "negative threshold for dP";
  parameter Real y_start=0.05 "initial condition for y";

protected
  parameter Integer nstore=3 "number of averaged points to store";
  Real p_store[nstore] "power samples";
  Real v_store[nstore] "voltage samples";
  Real p_sam[half_nsamples] "power samples";
  Real v_sam[half_nsamples] "voltage samples";
  Integer n(start=-1) "sample counter";
  Real p_ave "average power at current update";
  Real v_ave "average voltage at current update";
  Real delta_V "change in voltage between updates";
```

```
  Real delta_P "change in power between updates";
  Real delta_P2 "intermediate change in power";

algorithm
  // at every sample, run the following:
  when sample(startTime, samplePeriod) then
    for m in 1:(half_nsamples - 1) loop
      v_sam[m] := pre(v_sam[m + 1]);
      p_sam[m] := pre(p_sam[m + 1]);
    end for;
    v_sam[half_nsamples] := v;
    p_sam[half_nsamples] := v*i;
    n := pre(n) + 1;
  end when;

  // at every half_nsamples, run the following:
  when mod(n, half_nsamples) == 0 then
    p_ave := sum(p_sam[:])/(half_nsamples);
    v_ave := sum(v_sam[:])/(half_nsamples);

    for m in 1:(nstore - 1) loop
      v_store[m] := pre(v_store[m + 1]);
      p_store[m] := pre(p_store[m + 1]);
    end for;

    v_store[nstore] := v_ave;
    p_store[nstore] := p_ave;
  end when;

  // at every nsamples, run the following:
  when mod(n, nsamples) == 0 then
    delta_V := v_store[3] - v_store[1];
    delta_P := (p_store[2] - p_store[1]) - (p_store[3] - p_store[2]);
    delta_P2 := p_store[3] - p_store[2];

    if abs(delta_P2) < abs(delta_P) then
      // run basic dP-P&0 with fine delta
      if delta_P < 1e-6 and delta_P > -1e-6 then
        y := pre(y);
      else
        if delta_P > 0 then
          if delta_V > 0 then
            y := pre(y) + delta_fine;
          else
            y := pre(y) - delta_fine;
          end if;
        else
          if delta_V > 0 then
            y := pre(y) - delta_fine;
          else
            y := pre(y) + delta_fine;
          end if;
        end if;
      end if;
    else
      // run optimized dP-P&O with coarse delta
      if delta_P2 < 0 then
```

```
        if delta_P >= ThP then
          y := pre(y) - delta_coarse;
        else
          if delta_P <= ThN then
            if delta_V >= 0 then
              y := pre(y) - delta_coarse;
            else
              y := pre(y) + delta_coarse;
            end if;
          else
            if delta_V < 1e-6 and delta_V > -1e-6 then
              y := pre(y) - delta_coarse;
            else
              y := pre(y);
            end if;
          end if;
        end if;
      else
        if delta_P >= ThP then
          y := pre(y) + delta_coarse;
        else
          if delta_P <= ThN then
            if delta_V <= 0 then
              y := pre(y) + delta_coarse;
            else
              y := pre(y) - delta_coarse;
            end if;
          else
            if delta_V < 1e-6 and delta_V > -1e-6 then
              y := pre(y) + delta_coarse;
            else
              y := pre(y);
            end if;
          end if;
        end if;
      end if;
    end if;
  end when;

end dP_PandO;
```

A.4 Modelica Code to Compute Root-Mean-Square (rms)

```
model RMS
  "Computes moving root-mean-square value of input signal"

  extends Modelica.Blocks.Interfaces.DiscreteBlockIcon;
  parameter Modelica.SIunits.Time samplePeriod=1/(15e3)
    "sampling period";
  parameter Integer nsamples=250
    "number of samples to process (sampling frequency / cycle
    frequency)";

protected
  Real u_sam[nsamples] "samples of input";

equation
```

```
  when sample(0, samplePeriod) then
    for i in 1:(nsamples - 1) loop
      u_sam[i] = pre(u_sam[i + 1]);
    end for;
    u_sam[nsamples] = u;
    y = sqrt(sum(u_sam[:] .^ 2)/nsamples);
  end when;

end RMS;
```

A.5 Modelica Code to Compute Frequency

```
model Freq "Frequency computation from zero crossings"

  extends Modelica.Blocks.Interfaces.DiscreteBlockIcon;
  parameter Real f_nom(unit="Hz") = 60 "Nominal frequency";

protected
  Real z_c_t(start=0,unit="s") "Time at zero crossing";
  Integer n(start=-1) "Counter";

equation

  ZeroCrossing.enable = true "Enable ZeroCrossing block";

  when ZeroCrossing.y == true then
    n = pre(n) + 1;
  end when;

  when mod(n, 2) == 0 then
    z_c_t = time;
    if z_c_t <= 0 then
      y = f_nom;
    else
      y = 1/(z_c_t - pre(z_c_t));
    end if;
  end when;

end Freq;
```

A.6 MATLAB Code to Perform FFT and Compute THD

```
% Script to check if current harmonics are within IEEE 1547 harmonic
% limits

% Trishan Esram
% 03/12/2009

clear all; close all; clc

% Load Dymola simulation output data file:
[filename,pathname]=uigetfile('*.mat');
data = dymload(filename);

time = dymget(data,'Time');     % time
i_out = dymget(data,'Grid.i');  % output current
```

```
% Indices:
t_final = max(time);                          % stop time of simulation
ind1 = find(time<(t_final-1/60),1,'last')+1; % index for one line cycle
ind2 = find(time<(t_final),1,'last')+1;      % ending index

% Harmonic array:
harmonic = (0:1:(ind2-ind1));                 % harmonic numbers

% Truncate data (to remove startup)
i_out_cut = i_out(ind1:ind2); clear i_out

% FFT of signals
i_out_fft = 2*fft(i_out_cut)/length(i_out_cut);
i_out_fft(1) = i_out_fft(1)/2;    % correction to dc component

% Normalized FFT (in percentage)
i_out_fft_norm = 100*i_out_fft./i_out_fft(2);

% IEEE 1547 limits (in percentage); indices are +1 because they cannot
% start with zero in MATLAB:
IEEE(1:2)=100;
IEEE(3:11)=4;
IEEE(12:17)=2;
IEEE(18:23)=1.5;
IEEE(24:35)=0.6;
IEEE(36:length(harmonic))=0.3;

% Plot waveform (1 cycle)
figure
plot(time(ind1:ind2),i_out_cut)
xlim([time(ind1) time(ind2)])
xlabel('Time (s)'); ylabel('Output Current (A)'); grid on

% Plot normalized FFTs (in percentage)
figure
bar(harmonic,abs(i_out_fft_norm),'k');
grid on; hold on
plot(harmonic,IEEE,'k--');
xlim([0 40])                              % display up to 40th harmonic
ylim([0 5])                               % display up to 5%
legend('i_o_u_t','IEEE limits',0)
xlabel('Harmonic Number'); ylabel('Percentage of fundamental');
title('Output Current Harmonics')

% Compute THD of output current using first 40 harmonics
i_THD_40 = sqrt(sum(abs(i_out_fft(3:40)).^2)/...
    abs(i_out_fft(2))^2)*100

% Compute THD of output current using all harmonics
i_THD_all = sqrt(sum(abs(i_out_fft(3: length(harmonic)/2)).^2)/...
    abs(i_out_fft(2))^2)*100
```

A.7 Modelica Code for AFD IDM Current Command Generation

```
model i_AFD "Current command generation for AFD IDM"

  extends Modelica.Blocks.Interfaces.DiscreteBlockIcon;
```

```
  parameter Modelica.SIunits.Time startTime=1/60 "Start time";

  parameter Real delta_f(unit="Hz") = 1.5 "Frequency difference";

protected
  parameter Real pi=Modelica.Constants.pi "pi";
  Real z_c_t(start=0,unit="s") "Time at zero-cross";
  Integer n(start=-1) "Counter";

equation

  ZeroCrossing.enable = true "Enable ZeroCrossing block";

  when ZeroCrossing.y == true then
    n = pre(n) + 1;
    z_c_t = time;
  end when;

  if time >= startTime and not not_EN then
    if mod(n, 2) > 0 then
      y = -max((P/V_rms)*sqrt(2)*sin(2*pi*(f + delta_f)*(time –
        z_c_t)),0);
    else
      y = max((P/V_rms)*sqrt(2)*sin(2*pi*(f + delta_f)*(time - z_c_t)),
        0);
    end if;
  else
    y = 0;
  end if;

end i_AFD;
```

A.8 Modelica Code for SMS IDM Current Command Generation

```
model i_SMS "Current command generation for SMS IDM"

  extends Modelica.Blocks.Interfaces.DiscreteBlockIcon;
  parameter Modelica.SIunits.Time startTime=1/60 "Start time";

  parameter Real theta_m(unit="deg") = 10 "Maximum phase shift";
  parameter Real f_m(unit="Hz") = 63 "Maximum phase shift frequency";
  parameter Real f_g(unit="Hz") = 60 "Nominal grid frequency";

protected
  parameter Real pi=Modelica.Constants.pi "pi";
  Real z_c_t(start=0,unit="s") "Time at zero-cross";
  Integer n(start=-1) "Counter";
  Real theta_sms(unit="rad") "SMS phase shift";

equation

  ZeroCrossing.enable = true "Enable ZeroCrossing block";

  when ZeroCrossing.y == true then
    n = pre(n) + 1;
  end when;
```

```
  when mod(n, 2) == 0 then
    z_c_t = time;
  end when;

  theta_sms = (theta_m*pi/180)*sin((pi/2)*((f - f_g)/(f_m - f_g)));

  if time >= startTime and not not_EN then
    y = (P/V_rms)*sqrt(2)*sin(2*pi*f*(time - z_c_t) + theta_sms);
  else
    y = 0;
  end if;

end i_SMS;
```

A.9 Modelica Code for SFS IDM Current Command Generation

```
model i_SFS "Current command generation for SFS IDM"

  extends Modelica.Blocks.Interfaces.DiscreteBlockIcon;
  parameter Modelica.SIunits.Time startTime=1/60 "Start time";

  parameter Real delta_f_0(unit="Hz") = 1.5
    "Initial frequency difference";
  parameter Real k=0 "Accelerating gain";
  parameter Real f_g(unit="Hz") = 60 "Nominal grid frequency";

protected
  parameter Real pi=Modelica.Constants.pi "pi";
  Real z_c_t(start=0,unit="s") "Time at zero-cross";
  Integer n(start=-1) "Counter";
  parameter Real cf_0=(1/f_g - 1/(f_g + delta_f_0))/(1/f_g)
    "Initial chopping factor";
  Real cf "Chopping factor";
  Real delta_f(unit="Hz",start=0) "Frequency difference";

equation

  ZeroCrossing.enable = true "Enable ZeroCrossing block";

  when ZeroCrossing.y == true then
    n = pre(n) + 1;
    z_c_t = time;
  end when;

  when mod(n, 2) == 0 then
    cf = cf_0 + k*(f - f_g);
  end when;

//compute delta_f from cf and use below for current command
//note that Dymola will solve for delta_f from the following equation:
  cf = (1/f - 1/(f + delta_f))/(1/f);

  if time >= startTime and not not_EN then
    if mod(n, 2) > 0 then
      y = -max((P/V_rms)*sqrt(2)*sin(2*pi*(f + delta_f)*(time –
        z_c_t)),0);
    else
```

```
      y = max((P/V_rms)*sqrt(2)*sin(2*pi*(f + delta_f)*(time - z_c_t)),
        0);
    end if;
  else
    y = 0;
  end if;

end i_SFS;
```

A.10 Modelica Code for Fault Detection

```
model Fault_Detector "Fault detector block"

  parameter Modelica.SIunits.Time t_start=1/60 "Start time";
  parameter Real f_up_limit(unit="Hz") = 60.5 "Upper frequency limit";
  parameter Real f_low_limit(unit="Hz") = 59.3 "Lower frequency limit";
  parameter Real grid_v_rms(unit="V") = 240 "Grid rms voltage";
  parameter Real rms_up_per(unit="%") = 110
    "Upper rms percentage limit";
  parameter Real rms_low_per(unit="%") = 88
    "Lower rms percentage limit";
  parameter Real f_nom(unit="Hz") = 60 "Nominal frequency";
  parameter Integer n_cycle=2
    "Number of line cycles to wait before shut-down";

protected
  Boolean f_flag "Flag when frequency is in abnormal range";
  Boolean rms_flag "Flag when rms is in abnormal range";
  Integer n_acc_f(start=-1) "Accumulator for frequency fault";
  Integer n_acc_rms(start=-1) "Accumulator for rms fault";
  Integer n(start=-1) "Zero-crossings counter";

algorithm
  when ZeroCrossing.y == true then
    n := pre(n) + 1;
  end when;

  when mod(n, 2) == 0 then
    if not f_flag then
      f_fault := false;
      n_acc_f := -1;
    else
      n_acc_f := pre(n_acc_f) + 1;
    end if;
    if not rms_flag then
      rms_fault := false;
      n_acc_rms := -1;
    else
      n_acc_rms := pre(n_acc_rms) + 1;
    end if;
    if n_acc_f >= n_cycle then
      f_fault := true;
    else
      f_fault := false;
    end if;
    if n_acc_rms >= n_cycle then
      rms_fault := true;
```

```
    else
      rms_fault := false;
    end if;
  end when;

equation
  ZeroCrossing.enable = true "Enable ZeroCrossing block";

  if (time > t_start and (f > f_up_limit or f < f_low_limit)) or pre(
      f_fault) then
    f_flag = true;
  else
    f_flag = false;
  end if;

  if (time > t_start and (rms > rms_up_per*grid_v_rms/100 or rms <
      rms_low_per*grid_v_rms/100)) or pre(rms_fault) then
    rms_flag = true;
  else
    rms_flag = false;
  end if;

end Fault_Detector;
```

APPENDIX B DERIVATIONS

B.1 Transfer Functions for Microinverter Input Stage

The state equations for the input-stage boost converter are

$$L\frac{di_L}{dt} = v - (1-q)v_{load} \text{ and} \tag{B.1}$$

$$C\frac{dv}{dt} = i - i_L . \tag{B.2}$$

Averaging on the order of a switching cycle, (B.1) and (B.2) can be rewritten as

$$L\frac{d\overline{i_L}}{dt} = \overline{v} - (1-d)\overline{v}_{load} = f\left(\overline{v}, d, \overline{v}_{load}\right) \text{ and} \tag{B.3}$$

$$C\frac{d\overline{v}}{dt} = \overline{i} - \overline{i_L} . \tag{B.4}$$

Let the equilibrium point *e* be

$$e = \left(V_0, D_0, V_{load\,0}\right). \tag{B.5}$$

Under small deviations around *e*, the nonlinear Equation (B.3) can be linearized as follows:

$$L\frac{d\tilde{i}_L}{dt} \approx f\big|_e + \left.\frac{\partial f}{\partial \overline{v}}\right|_e \tilde{v} + \left.\frac{\partial f}{\partial d}\right|_e \tilde{d} + \left.\frac{\partial f}{\partial \overline{v}_{load}}\right|_e \tilde{v}_{load} . \tag{B.6}$$

Since the first term on the left-hand side of (B.6) is zero, the linear small-signal model for the boost converter is

$$L\frac{d\tilde{i}_L}{dt} = \tilde{v} + V_{load\,0}\tilde{d} - \left(1 - D_0\right)\tilde{v}_{load} \text{ and} \tag{B.7}$$

$$C\frac{d\tilde{v}}{dt} = \tilde{i} - \tilde{i}_L . \tag{B.8}$$

Applying Laplace transform to (B.7) and (B.8) and dropping all the tildes,

$$sLi_L(s) = v(s) + V_{load\,0}d(s) + \left(D_0 - 1\right)v_{load}(s) \text{ and} \tag{B.9}$$

$$sCv(s) = i(s) - i_L(s). \tag{B.10}$$

Since it is desired to control the photovoltaic (PV) module current *i*, solving for the inductor *L* current i_L from (B.10) and substituting it into (B.9) results in

$$sLi(s) = (s^2LC + 1)v(s) + V_{load\,0}d(s) + \left(D_0 - 1\right)v_{load}(s). \tag{B.11}$$

Equation (B.11) can be rewritten as

$$i(s) = G_v(s)v(s) + G_d(s)d(s) + G_{vload}(s)v_{load}(s), \tag{B.12}$$

where

$$G_v(s) = \frac{s^2LC + 1}{sL}, \tag{B.13}$$

$$G_d(s) = \frac{V_{load0}}{sL}, \text{ and} \tag{B.14}$$

$$G_{vload}(s) = \frac{D_0 - 1}{sL}. \tag{B.15}$$

$G_v(s)$ represents the PV module voltage v to i transfer function, $G_d(s)$ the duty ratio d to i transfer function, and $G_{vload}(s)$ the load voltage v_{load} to i transfer function.

With the use of average current mode (ACM) control, which is essentially a proportional-integral (PI) control to drive the error between the current command i^* and i to zero, d is given as

$$d = k_{p_acm}\left(i^* - i\right) + k_{i_acm}\int\left(i^* - i\right)dt. \tag{B.16}$$

The Laplace transform of (B.16) is

$$d(s) = H_d(s)\left[i^*(s) - i(s)\right], \tag{B.17}$$

where

$$H_d(s) = \frac{k_{p_acm}s + k_{i_acm}}{s}. \tag{B.18}$$

Plugging (B.17) into (B.12),

$$i(s) = G_v(s)v(s) + G_d(s)H_d(s)\left[i^*(s) - i(s)\right] + G_{vload}(s)v_{load}(s). \tag{B.19}$$

If $v(s)$ and $v_{load}(s)$ in (B.19) are zero, the i^* to i transfer function is given as

$$\frac{i(s)}{i^*(s)} = \frac{G_d(s)H_d(s)}{1 + G_d(s)H_d(s)}. \tag{B.20}$$

Substituting (B.14) and (B.18) into (B.20) results in

$$\frac{i(s)}{i^*(s)} = \frac{V_{load0}k_{p_acm}s + V_{load0}k_{i_acm}}{Ls^2 + V_{load0}k_{p_acm}s + V_{load0}k_{i_acm}}. \tag{B.21}$$

Furthermore, the loop gain of (B.20) is given as

$$\ell_i(s) = G_d(s)H_d(s) = \frac{V_{load0}k_{p_acm}s + V_{load0}k_{i_acm}}{Ls^2}. \tag{B.22}$$

On the other hand, setting $v(s)$ and $i^*(s)$ in (B.19) to zero leads to the v_{load} to i transfer function

$$\frac{i(s)}{v_{load}(s)} = \frac{G_{vload}(s)}{1 + G_d(s)H_d(s)}, \tag{B.23}$$

which, with the use of (B.14), (B.15), and (B.18) can be written as

$$\frac{i(s)}{v_{load}(s)} = \frac{(D_0 - 1)s}{Ls^2 + V_{load0}k_{p_acm}s + V_{load0}k_{i_acm}}. \tag{B.24}$$

B.2 Transfer Functions for Microinverter with Passive Filter

For the microinverter with the passive filter, the state equation at the bus capacitor can be expressed as

$$C_{bus}\frac{dv_{bus}}{dt} = i_r - i_{of}. \tag{B.25}$$

Averaging over half the period of the utility grid voltage,

$$C_{bus}\frac{d\overline{v}_{bus}}{dt} = \overline{i}_r - \overline{i}_{of} = \overline{i}_r - V_{out0}\frac{\overline{i}_{out}}{\overline{v}_{bus}} = f\left(\overline{i}_r, \overline{i}_{out}, \overline{v}_{bus}\right), \tag{B.26}$$

where V_{out0} is the nominal root-mean-square (rms) of the output voltage v_{out} of the output stage of the microinverter.

Let the equilibrium point e be

$$e = \left(I_{r0}, I_{out0}, V_{bus0}\right). \tag{B.27}$$

Equation (B.26) can be linearized around e as follows:

$$C_{bus}\frac{d\tilde{v}_{bus}}{dt} \approx f\big|_e + \left.\frac{\partial f}{\partial \overline{i}_r}\right|_e \tilde{i}_r + \left.\frac{\partial f}{\partial \overline{i}_{out}}\right|_e \tilde{i}_{out} + \left.\frac{\partial f}{\partial \overline{v}_{bus}}\right|_e \tilde{v}_{bus}. \tag{B.28}$$

With the first term on the left-hand side of (B.28) being zero,

$$C_{bus}\frac{d\tilde{v}_{bus}}{dt} = \tilde{i}_r - \frac{V_{out0}}{V_{bus0}}\tilde{i}_{out} + \frac{V_{out0}I_{out0}}{V_{bus0}^2}\tilde{v}_{bus}. \tag{B.29}$$

Applying Laplace transform and dropping all the tildes,

$$sC_{bus}v_{bus}(s) = i_r(s) - \frac{V_{out0}}{V_{bus0}}i_{out}(s) + \frac{V_{out0}I_{out0}}{V_{bus0}^2}v_{bus}(s), \tag{B.30}$$

which can be rewritten as

$$v_{bus}(s) = G_{ir}(s) i_r(s) - G_{iout}(s) i_{out}(s), \tag{B.31}$$

where

$$G_{ir}(s) = \frac{V_{bus0}^2}{C_{bus} V_{bus0}^2 s - I_{out0} V_{out0}} \text{ and} \tag{B.32}$$

$$G_{iout}(s) = \frac{V_{bus0} V_{out0}}{C_{bus} V_{bus0}^2 s - I_{out0} V_{out0}}. \tag{B.33}$$

The transfer function $v_{bus}(s)/i_{out}(s)$ represents the bus capacitor impedance as seen by the microinverter output stage and is obtained from (B.31) if $i_r(s)$ is zero:

$$\frac{v_{bus}(s)}{i_{out}(s)} = -G_{iout}(s) = -\frac{V_{bus0} V_{out0}}{C_{bus} V_{bus0}^2 s - I_{out0} V_{out0}}. \tag{B.34}$$

In the microinverter topology with the passive filter, the average of v_{bus} is controlled by controlling i_{out} as follows:

$$\overline{i}_{out} = \frac{1}{V_{out0}} \left[k_{p_vbus} \left(\overline{v}_{bus} - \overline{v}_{bus}^* \right) + k_{i_vbus} \int \left(\overline{v}_{bus} - \overline{v}_{bus}^* \right) dt + p \right], \tag{B.35}$$

where p is the PV module power. In the frequency domain, (B.35) translates to

$$i_{out}(s) = H_{iout}(s) \left[v_{bus}(s) - v_{bus}^*(s) \right], \tag{B.36}$$

where

$$H_{iout}(s) = \frac{k_{p_vbus} s + k_{i_vbus}}{V_{out0} s}. \tag{B.37}$$

Plugging (B.36) into (B.31),

$$v_{bus}(s) = G_{ir}(s) i_r(s) - G_{iout}(s) H_{iout}(s) \left[v_{bus}(s) - v_{bus}^*(s) \right]. \tag{B.38}$$

Thus, when $i_r(s)$ is zero, the transfer function $v_{bus}(s)/v_{bus}^*(s)$ can be formulated as

$$\frac{v_{bus}(s)}{v_{bus}^*(s)} = \frac{G_{iout}(s) H_{iout}(s)}{1 + G_{iout}(s) H_{iout}(s)}, \tag{B.39}$$

which can be explicitly written as

$$\frac{v_{bus}(s)}{v_{bus}^*(s)} = \frac{V_{bus0} k_{p_vbus} s + V_{bus0} k_{i_vbus}}{C_{bus} V_{bus0}^2 s^2 + \left(k_{p_vbus} V_{bus0} - I_{out0} V_{out0} \right) s + V_{bus0} k_{i_vbus}}. \tag{B.40}$$

The loop gain of (B.39) is

$$\ell_{vbus}(s) = G_{iout}(s)H_{iout}(s) = \frac{V_{bus0}k_{p_vbus}s + V_{bus0}k_{i_vbus}}{C_{bus}V_{bus0}^2 s^2 - I_{out0}V_{out0}s}. \quad \text{(B.41)}$$

B.3 Transfer Functions for Microinverter with Active Filter

The state equation at the bus capacitor of the microinverter with active filter can be expressed as

$$C_{bus}\frac{dv_{bus}}{dt} = i_r - i_{of} - i_{afc}. \quad \text{(B.42)}$$

Averaging over half the period of the utility grid voltage,

$$C_{bus}\frac{d\overline{v}_{bus}}{dt} = \overline{i}_r - \overline{i}_{of} - \overline{i}_{afc} = \overline{i}_r - V_{out0}\frac{\overline{i}_{out}}{\overline{v}_{bus}} - \frac{\overline{v}_{af}\overline{i}_{af}}{\overline{v}_{bus}} = f\left(\overline{i}_r, \overline{i}_{out}, \overline{v}_{bus}, \overline{i}_{af}, \overline{v}_{af}\right). \quad \text{(B.43)}$$

Let the equilibrium point *e* be

$$e = \left(I_{r0}, I_{out0}, V_{bus0}, I_{af0}, V_{af0}\right). \quad \text{(B.44)}$$

Assuming small deviations around *e*, (B.43) can be linearized as

$$C_{bus}\frac{d\tilde{v}_{bus}}{dt} \approx f\big|_e + \left.\frac{\partial f}{\partial \overline{i}_r}\right|_e \tilde{i}_r + \left.\frac{\partial f}{\partial \overline{i}_{out}}\right|_e \tilde{i}_{out} + \left.\frac{\partial f}{\partial \overline{v}_{bus}}\right|_e \tilde{v}_{bus} + \left.\frac{\partial f}{\partial \overline{i}_{af}}\right|_e \tilde{i}_{af} + \left.\frac{\partial f}{\partial \overline{v}_{af}}\right|_e \tilde{v}_{af}. \quad \text{(B.45)}$$

The first term on the left-hand side of the above equation evaluates to zero and

$$C_{bus}\frac{d\tilde{v}_{bus}}{dt} = \tilde{i}_r - \frac{V_{out0}}{V_{bus0}}\tilde{i}_{out} + \frac{V_{out0}I_{out0}}{V_{bus0}^2}\tilde{v}_{bus} - \frac{V_{af0}}{V_{bus0}}\tilde{i}_{af} - \frac{I_{af0}}{V_{bus0}}\tilde{v}_{af}. \quad \text{(B.46)}$$

Since I_{af0} is generally zero,

$$C_{bus}\frac{d\tilde{v}_{bus}}{dt} = \tilde{i}_r - \frac{V_{out0}}{V_{bus0}}\tilde{i}_{out} + \frac{V_{out0}I_{out0}}{V_{bus0}^2}\tilde{v}_{bus} - \frac{V_{af0}}{V_{bus0}}\tilde{i}_{af}. \quad \text{(B.47)}$$

Applying Laplace transform and dropping all the tildes,

$$sC_{bus}v_{bus}(s) = i_r(s) - \frac{V_{out0}}{V_{bus0}}i_{out}(s) + \frac{V_{out0}I_{out0}}{V_{bus0}^2}v_{bus}(s) - \frac{V_{af0}}{V_{bus0}}i_{af}(s), \quad \text{(B.48)}$$

which can be simply expressed as

$$v_{bus}(s) = G_{ir}(s)i_r(s) - G_{iout}(s)i_{out}(s) - G_{iaf}(s)i_{af}(s), \quad \text{(B.49)}$$

where

$$G_{ir}(s) = \frac{V_{bus0}^2}{C_{bus}V_{bus0}^2 s - I_{out0}V_{out0}}, \quad \text{(B.50)}$$

$$G_{iout}(s) = \frac{V_{bus0}V_{out0}}{C_{bus}V_{bus0}^2 s - I_{out0}V_{out0}}, \text{ and} \tag{B.51}$$

$$G_{iaf}(s) = \frac{V_{af0}V_{bus0}}{C_{bus}V_{bus0}^2 s - I_{out0}V_{out0}}. \tag{B.52}$$

In the microinverter with active filter, controlling i_{out} controls the average of v_{af} as dictated by

$$\overline{i}_{out} = \frac{1}{V_{out0}}\left[k_{p_vaf}\left(\overline{v}_{af} - \overline{v}_{af}^*\right) + k_{i_vaf}\int\left(\overline{v}_{af} - \overline{v}_{af}^*\right)dt + p\right]. \tag{B.53}$$

The Laplace transform of (B.53) is

$$i_{out}(s) = H_{iout}(s)\left[v_{af}(s) - v_{af}^*(s)\right], \tag{B.54}$$

where

$$H_{iout}(s) = \frac{k_{p_vaf}s + k_{i_vaf}}{V_{out0}s}. \tag{B.55}$$

On the other hand, the average of v_{bus} is controlled by controlling i_{af} as follows:

$$\overline{i}_{af} = \frac{1}{\overline{v}_{af}}\left[k_{p_vbus}\left(\overline{v}_{bus} - \overline{v}_{bus}^*\right) + k_{i_vbus}\int\left(\overline{v}_{bus} - \overline{v}_{bus}^*\right)dt\right], \tag{B.56}$$

whose Laplace transform can be shown to be

$$i_{af}(s) = H_{iaf}(s)\left[v_{bus}(s) - v_{bus}^*(s)\right], \tag{B.57}$$

where

$$H_{iaf}(s) = \frac{k_{p_vbus}s + k_{i_vbus}}{V_{af0}s}. \tag{B.58}$$

Substituting (B.57) into (B.49) results in

$$v_{bus}(s) = G_{ir}(s)i_r(s) - G_{iout}(s)i_{out}(s) - G_{iaf}(s)H_{iaf}(s)\left[v_{bus}(s) - v_{bus}^*(s)\right]. \tag{B.59}$$

If $i_r(s)$ and $i_{out}(s)$ are zero,

$$\frac{v_{bus}(s)}{v_{bus}^*(s)} = \frac{G_{iaf}(s)H_{iaf}(s)}{1 + G_{iaf}(s)H_{iaf}(s)}, \tag{B.60}$$

which can be written as

$$\frac{v_{bus}(s)}{v_{bus}^*(s)} = \frac{V_{bus0}k_{p_vbus}s + V_{bus0}k_{i_vbus}}{C_{bus}V_{bus0}^2 s^2 + \left(k_{p_vbus}V_{bus0} - I_{out0}V_{out0}\right)s + V_{bus0}k_{i_vbus}}. \tag{B.61}$$

Moreover, the loop gain of (B.60) is given as

$$\ell_{vbus}(s) = G_{iaf}(s)H_{iaf}(s) = \frac{V_{bus0}k_{p_vbus}s + V_{bus0}k_{i_vbus}}{C_{bus}V_{bus0}^2 s^2 - I_{out0}V_{out0}s}. \quad \text{(B.62)}$$

From (B.59), if $i_r(s)$ and $v_{bus}^*(s)$ are zero, the bus capacitor impedance as seen by the output stage of the microinverter is given by

$$\frac{v_{bus}(s)}{i_{out}(s)} = \frac{-G_{iout}(s)}{1 + G_{iaf}(s)H_{iaf}(s)}, \quad \text{(B.63)}$$

which simplifies to

$$\frac{v_{bus}(s)}{i_{out}(s)} = \frac{V_{bus0}V_{out0}s}{C_{bus}V_{bus0}^2 s^2 + \left(k_{p_vbus}V_{bus0} - I_{out0}V_{out0}\right)s + V_{bus0}k_{i_vbus}}. \quad \text{(B.64)}$$

Substituting (B.54) into (B.49) leads to

$$v_{bus}(s) = G_{ir}(s)i_r(s) - G_{iout}(s)H_{iout}(s)\left[v_{af}(s) - v_{af}^*(s)\right] - G_{iaf}(s)i_{af}(s). \quad \text{(B.65)}$$

Furthermore, the relationship between v_{af} and i_{af} is given by

$$C_{af}\frac{dv_{af}}{dt} = i_{af}, \quad \text{(B.66)}$$

whose Laplace transform is

$$sC_{af}v_{af}(s) = i_{af}(s). \quad \text{(B.67)}$$

Therefore, combining (B.65) and (B.67),

$$v_{bus}(s) = G_{ir}(s)i_r(s) - G_{iout}(s)H_{iout}(s)\left[v_{af}(s) - v_{af}^*(s)\right] - sC_{af}G_{iaf}(s)v_{af}(s). \quad \text{(B.68)}$$

If $i_r(s)$ and $v_{bus}(s)$ are zero,

$$\frac{v_{af}(s)}{v_{af}^*(s)} = \frac{G_{iout}(s)H_{iout}(s)}{sC_{af}G_{iaf}(s) + G_{iout}(s)H_{iout}(s)}, \quad \text{(B.69)}$$

more explicitly written as

$$\frac{v_{af}(s)}{v_{af}^*(s)} = \frac{k_{p_vaf}s + k_{i_vaf}}{C_{af}V_{af0}s^2 + k_{p_vaf}s + k_{i_vaf}}. \quad \text{(B.70)}$$

The loop gain of (B.69) can be expressed as

$$\ell_{vaf}(s) = \frac{G_{iout}(s)H_{iout}(s)}{sC_{af}G_{iaf}(s)} = \frac{k_{p_vaf}s + k_{i_vaf}}{C_{af}V_{af0}s^2}. \quad \text{(B.71)}$$

APPENDIX C MULTIPLE-CARRIER PWM

The switching signals for a conventional inverter with a direct-current (dc) source or link—like those for the microinverter proposed in this dissertation—can be readily generated through conventional pulse-width modulation (PWM) by comparing a triangle or ramp carrier with a modulating function. This results in a PWM output waveform from which information about the modulating function can be recovered through filtering. Such an example can be found in Section 5.5.

For an inverter or a cycloconverter with a high-frequency (HF) source or link, like that analyzed in Section 1.4, the same waveforms as in conventional PWM inverters can be obtained by using multiple-carrier PWM [26]. Multiple-carrier PWM generally consists in generating multiple pulse sequences that, when unified, form a useful gate control sequence. Switching this gate control sequence against the HF source or link produces a PWM output waveform [26].

A general two-carrier PWM sequence generation process that can construct families of PWM sequences is analyzed in [26]. For every case presented therein, the resulting output PWM waveform depends on the gate control sequence. It will be shown below that it is possible to generate waveforms similar to those in [26] through simple equations. More importantly, it will be shown that the exact gate sequence can be easily generated by modulating the phase of a typical clock signal, without the need for multiple carrier signals and modulating functions.

Consider a carrier signal

$$tri(t) = \frac{1}{\pi}\cos^{-1}\left[\cos\left(\omega_{sw}t\right)\right], \text{ where} \tag{C.1}$$

$$\omega_{sw} = 2\pi f_{sw}. \tag{C.2}$$

In Equation (C.2), f_{sw} is the switching frequency. The function *tri* is zero at $t = 0$, one at $\omega_{sw}t = \pi$, and returns to zero at $\omega_{sw}t = 2\pi$. This function produces a triangle wave that varies between 0 and 1, at the switching frequency f_{sw}, as shown in Fig. C.1 (a), which also displays a clock signal *clk* defined as

$$clk(t) = \frac{1}{2}\left[1 + \text{sgn}\left(\sin\left(\omega_{sw}t\right)\right)\right]. \tag{C.3}$$

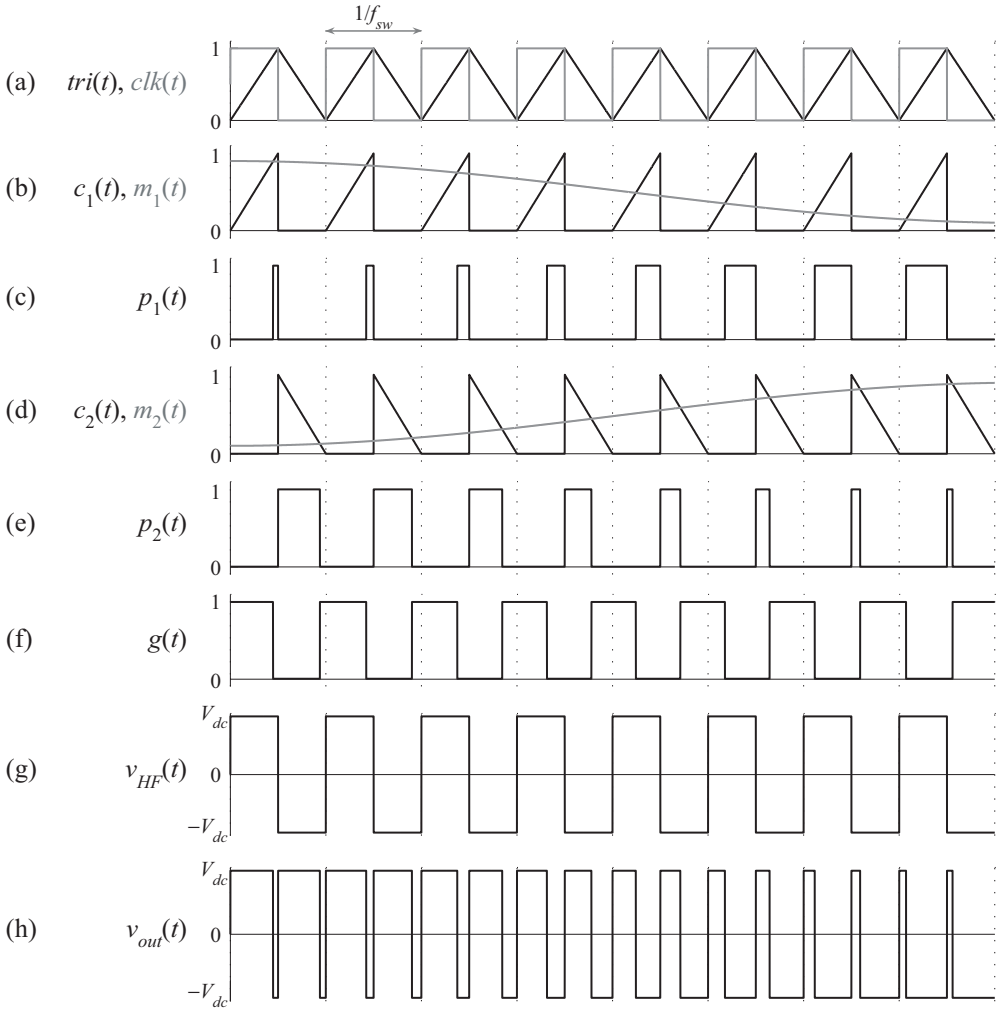


Fig. C.1 Example of multiple-carrier PWM generation

Two carrier signals, one corresponding to the rising slope of *tri* and the other to the falling slope, can be formulated as

$$c_1(t) = tri(t)clk(t), \text{ and} \tag{C.4}$$

$$c_2(t) = tri(t)\left[1 - clk(t)\right], \tag{C.5}$$

and illustrated in Fig. C.1 (b) and (d), respectively. Two modulating functions can be defined as

$$m_1(t) = \frac{1}{2}\left[1 + d_m \cos\left(\omega t\right)\right], \text{ and} \tag{C.6}$$

$$m_2(t) = \frac{1}{2}\left[1 - d_m \cos\left(\omega t\right)\right], \text{ where} \tag{C.7}$$

$$\omega = 2\pi f, \tag{C.8}$$

d_m is a constant, and f is the frequency. Comparing these modulating functions with the two carrier signals, as in Fig. C.1 (b) and (d), results in two pulse signals given by

$$p_1(t) = m_1(t) < c_1(t)\text{, and} \tag{C.9}$$

$$p_2(t) = m_2(t) < c_2(t), \tag{C.10}$$

shown in Fig. C.1 (c) and (e), respectively.

A gate control sequence can be formed by concatenating the pulse signals as

$$g(t) = 1 - \left[p_1(t) + p_2(t) \right] \tag{C.11}$$

and is shown in Fig. C.1 (f). While g displays a duty ratio of nearly 50%, it embeds the total PWM information. This can be extracted by switching g against a HF link voltage

$$v_{HF}(t) = V_{dc}\left[2clk(t) - 1 \right], \tag{C.12}$$

shown in Fig. C.1 (g), to form the PWM output voltage

$$v_{out}(t) = v_{HF}(t)\left[2g(t) - 1 \right], \tag{C.13}$$

shown in Fig. C.1 (h).

Interestingly, g can also be written as the phase modulation of clk as

$$g(t) = clk\left[t + \frac{1}{2f_{sw}}\left(\frac{1 - d_m \cos(\omega t)}{2} \right) \right] = clk\left[t + \frac{1}{2f_{sw}} m_2(t) \right]. \tag{C.14}$$

This matches exactly the signal formed by the multiple-carrier PWM approach, as shown in Fig. C.2. As can be noted in (C.14), the phase of clk is varied by one of the modulating functions. Although it is not shown how (C.14) was derived, it is conceptually much simpler to implement than generating carrier signals and comparing them with the modulating functions to produce the pulse signals. Further work is required to show the advantages of this phase modulating technique and its application to high-frequency link inverters.

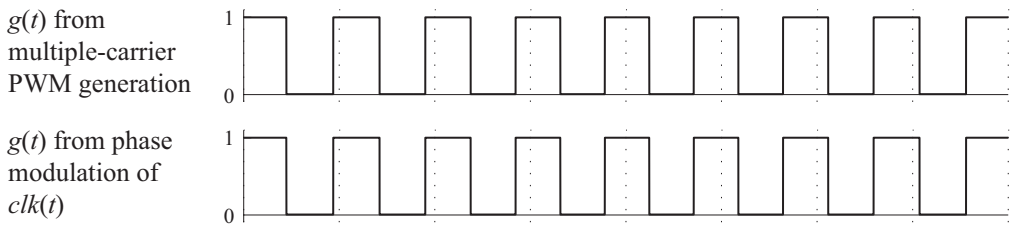


Fig. C.2 Two methods of generating the same gate control sequence

REFERENCES

[1] T. Esram, P. T. Krein, B. T. Kuhn, R. S. Balog, and P. L. Chapman, "Power electronics needs for achieving grid-parity solar energy costs," in *IEEE Energy 2030 Conference*, 2008, pp. 1–5.

[2] V. Gowrishankar, D. Hutton, C. Fluhrer, and N. Dasgupta, "Making photovoltaic power competitive with grid power," in *Conference Record of the 2006 IEEE 4th World Conference on Photovoltaic Energy Conversion*, 2006, pp. 2532–2535.

[3] Prometheus Institute and Solar Energy Industries Association, "US solar industry—Year in review 2007," 2008.

[4] U.S. Energy Information Administration. (Accessed March 2010). Electricity in the United States. [Online]. Available: http://tonto.eia.doe.gov/energyexplained/index.cfm?page=electricity_in_the_united_states

[5] Solarbuzz. (Accessed March 2010). Guideline electricity generation costs today. [Online]. Available: http://www.solarbuzz.com/statsCosts.htm

[6] National Oceanic & Atmospheric Administration. (Accessed March 2010). SURFRAD data display page. [Online]. Available: http://www.srrb.noaa.gov/surfrad/pick.html

[7] Ameren IP. (Accessed March 2010). Real time prices. [Online]. Available: https://www2.ameren.com/RetailEnergy/realtimeprices.aspx

[8] U.S. Energy Information Administration. (Accessed March 2010). 2007 state electricity profiles. [Online]. Available: http://www.eia.doe.gov/fuelelectric.html

[9] R. Wiser, G. Barbose, and C. Peterman, "Tracking the sun: The installed cost of photovoltaics in the U.S. from 1998–2007," Lawrence Berkeley National Laboratory, LBNL-1516E, Feb. 2009.

[10] U.S. Energy Information Administration. (Accessed March 2010). Factors affecting electricity prices. [Online]. Available: http://tonto.eia.doe.gov/energyexplained/index.cfm?page=electricity_factors_affecting_prices

[11] Solarbuzz. (Accessed March 2010). Solar module retail price environment. [Online]. Available: http://www.solarbuzz.com/Moduleprices.htm

[12] Solarbuzz. (Accessed March 2010). Inverter price environment. [Online]. Available: http://www.solarbuzz.com/Inverterprices.htm

[13] Y. Chernova, "Shedding light on solar," in *The Wall Street Journal*, 30 June 2008, pp. R6.

[14] R. Stevenson, “First Solar: Quest for the $1 watt,” in *IEEE Spectrum*, vol. 45, Aug. 2008, pp. 26–31.

[15] National Fire Protection Association, *National Electrical Code, International Electrical Code Series*, NFPA 70, 2008.

[16] J. Wiles, “Photovoltaic power systems and the 2005 National Electrical Code: Suggested practices,” Southwestern Technology Development Institute, SAND 2005-0342-N, March 2007.

[17] D. P. Hohm and M. E. Ropp, “Comparative study of maximum power point tracking algorithms using an experimental, programmable, maximum power point tracking test bed,” in *Conference Record of the Twenty-Eighth IEEE Photovoltaic Specialists Conference*, 2000, pp. 1699–1702.

[18] T. Esram and P. L. Chapman, “Comparison of photovoltaic array maximum power point tracking techniques,” *IEEE Transactions on Energy Conversion*, vol. 22, no. 2, pp. 439–449, June 2007.

[19] P. T. Krein and R. S. Balog, “Cost-effective hundred-year life for single-phase inverters and rectifiers in solar and LED lighting applications based on minimum capacitance requirements and a ripple power port,” in *Twenty-Fourth Annual IEEE Applied Power Electronics Conference and Exposition*, 2009, pp. 620–625.

[20] H. Oldenkamp, I. J. de Jong, C. W. A. Baltus, S. A. M. Verhoeven, and S. Elstgeest, “Reliability and accelerated life tests of the AC module mounted OKE4 inverter,” in *Conference Record of the Twenty Fifth IEEE Photovoltaic Specialists Conference*, 1996, pp. 1339–1342.

[21] G. Kern, “SunSine(TM) 300: Manufacture of an ac photovoltaic module,” Ascension Technology, Inc., NREL/SR-520-26085, March 1999.

[22] W. Bower, R. West, and A. Dickerson, “Innovative PV micro-inverter topology eliminates electrolytic capacitors for longer lifetime,” in *Conference Record of the 2006 IEEE 4th World Conference on Photovoltaic Energy Conversion*, 2006, pp. 2038–2041.

[23] AEE Solar. (Accessed March 2010). Micro-inverters and ac modules: The next generation solar energy solution or an idea from the past. [Online]. Available: http://av.conferencearchives.com/pdfs/091001/33.1308.pdf

[24] Q. Li and P. Wolfs, “A review of the single phase photovoltaic module integrated converter topologies with three different dc link configurations,” *IEEE Transactions on Power Electronics*, vol. 23, no. 3, pp. 1320–1333, May 2008.

[25] S. B. Kjaer, J. K. Pedersen, and F. Blaabjerg, "A review of single-phase grid-connected inverters for photovoltaic modules," *IEEE Transactions on Industry Applications*, vol. 41, no. 5, pp. 1292–1306, Sept. 2005.

[26] P. T. Krein, R. S. Balog, and X. Geng, "High-frequency link inverter for fuel cells based on multiple-carrier PWM," *IEEE Transactions on Power Electronics*, vol. 19, no. 5, pp. 1279–1288, Sept. 2004.

[27] R. S. Balog and P. T. Krein, "Commutation technique for high-frequency link cycloconverter based on state-machine control," *IEEE Power Electronics Letters*, vol. 3, no. 3, pp. 101–104, Sept. 2005.

[28] Dassault Systèmes. (Accessed March 2010). Dymola—Dynamic Modeling Laboratory. [Online]. Available: www.3ds.com/products/catia/portfolio/dymola

[29] British Petroleum. (Accessed March 2010). BP 7185 PV module datasheet. [Online]. Available: http://www.bp.com/liveassets/bp_internet/solar/bp_solar_uk/STAGING/local_assets/downloads_pdfs/b/BP7185_3022E-207_06.pdf

[30] T. Esram, "Maximum power point tracking of photovoltaic arrays using ripple correlation control," M.S. thesis, University of Illinois at Urbana-Champaign, Urbana, IL, United States of America, 2004.

[31] J. W. Bishop, "Computer simulation of the effects of electrical mismatches in photovoltaic cell interconnection circuits," *Solar Cells*, vol. 25, no. 1, pp. 73–89, Oct. 1988.

[32] J. A. Gow and C. D. Manning, "Development of a photovoltaic array model for use in power-electronics simulation studies," *IEE Proceedings on Electric Power Applications*, vol. 146, no. 2, pp. 193–200, 1999.

[33] H. Yamashita, K. Tamahashi, M. Michihira, A. Tsuyoshi, K. Amako, and M. Park, "A novel simulation technique of the PV generation system using real weather conditions," in *Proceedings of the Power Conversion Conference*, 2002, pp. 839–844.

[34] M. Park and I.-K. Yu, "A novel real-time simulation technique of photovoltaic generation systems using RTDS," *IEEE Transactions on Energy Conversion*, vol. 19, no. 1, pp. 164–169, 2004.

[35] F. Recart and A. Cuevas, "Application of junction capacitance measurements to the characterization of solar cells," *IEEE Transactions on Electron Devices*, vol. 53, no. 3, pp. 442–448, 2006.

[36] D. Sera, R. Teodorescu, and P. Rodriguez, "PV panel model based on datasheet values," in *IEEE International Symposium on Industrial Electronics*, 2007, pp. 2392–2396.

[37] A. S. Sedra and K. C. Smith, *Microelectronic Circuits*, 4 ed. New York: Oxford University Press, 1998.

[38] D. Sera, T. Kerekes, R. Teodorescu, and F. Blaabjerg, "Improved MPPT method for rapidly changing environmental conditions," in *2006 IEEE International Symposium on Industrial Electronics*, 2006, pp. 1420–1425.

[39] D. Sera, R. Teodorescu, J. Hantschel, and M. Knoll, "Optimized maximum power point tracker for fast-changing environmental conditions," *IEEE Transactions on Industrial Electronics*, vol. 55, no. 7, pp. 2629–2637, July 2008.

[40] L. Dixon, "Average current mode control of switching power supplies," Unitrode Application Note U-140, Texas Instruments, pp. 3-356–3-369, 1999.

[41] M. E. Ropp, M. Begovic, and A. Rohatgi, "Prevention of islanding in grid-connected photovoltaic systems," *Progress in Photovoltaics: Research and Applications*, vol. 7, no. 1, pp. 39–59, Feb. 1999.

[42] *IEEE Standard for Interconnecting Distributed Resources with Electric Power Systems*, IEEE Standard 1547, 2003.

[43] M. E. Ropp, M. Begovic, and A. Rohatgi, "Analysis and performance assessment of the active frequency drift method of islanding prevention," *IEEE Transactions on Energy Conversion*, vol. 14, no. 3, pp. 810–816, Sept. 1999.

[44] M. E. Ropp, M. Begovic, A. Rohatgi, G. A. Kern, R. H. Bonn, and S. Gonzalez, "Determining the relative effectiveness of islanding detection methods using phase criteria and nondetection zones," *IEEE Transactions on Energy Conversion*, vol. 15, no. 3, pp. 290–296, Sept. 2000.

[45] W. Bower and M. Ropp, "Evaluation of islanding detection methods for photovoltaic utility interactive power systems," International Energy Agency, IEA-PVPS T5-09:2002, March 2002.

[46] M. Xu, R. V. N. Melnik, and U. Borup, "Modeling anti-islanding protection devices for photovoltaic systems," *Renewable Energy*, vol. 29, no. 15, pp. 2195–2216, Dec. 2004.

[47] L. A. C. Lopes and H. Sun, "Performance assessment of active frequency drifting islanding detection methods," *IEEE Transactions on Energy Conversion*, vol. 21, no. 1, pp. 171–180, March 2006.

[48] V. V. Thong, J. Driesen, and R. Belmans, "Overview and comparisons of existing DG interconnection standards and technical guidelines," in *International Conference on Clean Electrical Power*, 2007, pp. 51–54.

[49] A. Woyte, R. Belmans, and J. Nijs, "Testing the islanding protection function of photovoltaic inverters," *IEEE Transactions on Energy Conversion*, vol. 18, no. 1, pp. 157–162, March 2003.

[50] *IEEE Standard Conformance Test Procedures for Equipment Interconnecting Distributed Resources with Electric Power Systems*, IEEE Standard 1547.1, 2005.

[51] P. T. Krein, *Elements of Power Electronics*. New York: Oxford University Press, Inc., 1998.

[52] S. B. Kjaer, J. K. Pedersen, and F. Blaabjerg, "Power inverter topologies for photovoltaic modules—a review," in *Conference Record of the Industry Applications Conference*, 2002, pp. 782–788.

[53] A. F. Dickerson and R. West, "Photovoltaic DC-to-AC power converter and control method," U.S. Patent 7521914, Apr. 21, 2009.

[54] M. Nikraz, H. Dehbonei, and C. V. N. Curtin, "Digital control of a voltage source inverter in photovoltaic applications," in *IEEE 35th Annual Power Electronics Specialists Conference*, 2004, pp. 3266–3271.

[55] P. T. Krein and R. S. Balog, "Methods for minimizing double-frequency ripple power in single-phase power conditioners," U.S. Patent Application Publication 2009/0097283, Apr. 16, 2009.

[56] P. L. Chapman, et al., "Apparatus and method for controlling DC-AC power conversion," U.S. Patent Application 12/563,495, Sep. 21, 2009.

[57] R. M. Hudson, T. Thorne, F. Mekanik, M. R. Behnke, S. Gonzalez, and J. Ginn, "Implementation and testing of anti-islanding algorithms for IEEE 929-2000 compliance of single phase photovoltaic inverters," in *Conference Record of the Twenty-Ninth IEEE Photovoltaic Specialists Conference*, 2002, pp. 1414–1419.

[58] L. Wang and T.-C. Lin, "Dynamic stability and transient responses of multiple grid-connected PV systems," in *IEEE/PES Transmission and Distribution Conference and Exposition*, 2008, pp. 1–6.

[59] E. J. Estebanez, V. M. Moreno, A. Pigazo, and M. Liserre, "An overview of anti-islanding detection algorithms in photovoltaic systems in case of multiple current-controlled inverters," in *35th Annual Conference of IEEE Industrial Electronics*, 2009, pp. 4555–4560.

[60] D. G. Infield, P. Onions, A. D. Simmons, and G. A. Smith, “Power quality from multiple grid-connected single-phase inverters,” *IEEE Transactions on Power Delivery*, vol. 19, no. 4, pp. 1983–1989, Oct. 2004.

[61] G. Chicco, J. Schlabbach, and F. Spertino, “Operation of multiple inverters in grid-connected large-size photovoltaic installations,” in *20th International Conference and Exhibition on Electricity Distribution*, 2009, pp. 1–4.

[62] T. Mizuno, Y. Noda, H. Koizumi, K. Nagasaka, K. Kurokawa, and H. Kobayashi, “The experimental results of an islanding detection method for Japanese AC modules,” in *Proceedings of 3rd World Conference on Photovoltaic Energy Conversion*, 2003, pp. 2058–2061.

[63] X. Zhou, X. Peng, and F. C. Lee, “A high power density, high efficiency and fast transient voltage regulator module with a novel current sensing and current sharing technique,” in *Fourteenth Annual IEEE Applied Power Electronics Conference and Exposition*, 1999, pp. 289–294.